Title

Integration of Physiologic MRI to Improve Antiangiogenic Treatment Management for Patients with Glioblastoma

Permalink

https://escholarship.org/uc/item/0933f04k

Author

Essock-Burns, Emma

Publication Date

2012

Peer reviewed|Thesis/dissertation

Integration of Physiologic MRI to Improve Antiangiogenic Treatment Management for
Patients with Glioblastoma

by

Emma Essock-Burns

DISSERTATION

Submitted in partial satisfaction of the requirements for the degree of

DOCTOR OF PHILOSOPHY

in

Bioengineering

in the

GRADUATE DIVISION

of the

UNIVERSITY OF CALIFORNIA, SAN FRANCISCO

Dedicated to my parents,

Ed Essock and Barbara Burns.

ACKNOWLEDGEMENTS:

_____

I would like to gratefully and sincerely thank my mentor, **Dr. Sarah Nelson**, for her continued support over the past five years. It is because of Sarah's outstanding mentorship, research guidance, and attack-big-problems mentality that I am able to put forth this body of work. Sarah is an incredible role model who has shown me what it means to be a true collaborator, a courageous thinker, and above all, an authentic leader. It has been an honor to be "one of Sarah's."

I have been fortunate to have many other supportive mentors during my time in the Bioengineering program. I'd like to thank my dissertation committee, **Dr. Susan Chang** and **Dr. Dan Vigneron** for guiding my research development and shaping my progress throughout graduate school. Susan has been an incredible mentor and inspiration to me. She is an incredibly fast thinker able to interpret new information and draw on a breadth of disciplines to comment on how it relates to clinical care. Susan has taught me to think of my research in terms of how it fits into clinical _decision-making_. She taught me to approach research problems by asking when a person arrives in clinic "what do I need to know" and then working backwards to the imaging. She knows where the field of neuro-oncology should head and helped me accomplish research that steps in that direction. I thank her immensely for her guiding light. Dan has been a friendly face and consistent ally through graduate school. As my academic advisor, Dan has seen my progress every step of the way. I have always felt he was actively listening to me and was

on my side. His advising left me calmer and more reassured of my direction and I am extremely grateful for that.

One of the best aspects of my training has been the breadth of cross-disciplinary mentorship I have received. I'd like to thank my GEMS project mentors, **Dr. Joanna Phillips** and **Dr. Annette Molinaro**. Joanna taught me what it really means to be cross-disciplinary. She taught me to think about histopathology scores not just as numbers, but as features. Annette taught me to think about data in terms of the strength of the numbers to identify where the statistical power lies. Together my GEMS mentors taught me how to "speak different languages" – something I am very grateful for.

I would also like to thank my qualifying exam committee: **Dr. Sharmila Majumdar**, **Dr. Soonmee Cha**, **Dr. Tracy McKnight**, and **Dr. Roland Henry**. I want to sincerely thank them for pushing me to expand my understanding of MRI. They recognized a potential for improvement in me and then provided me with the opportunity to grow. Sharmila showed me how to be me a bolder thinker. Tracy taught me to never treat any piece of my project as a "black box." Roland taught me to push my thinking to the extreme cases and always be ready to start deriving. Soonmee taught me to think in terms of the practical, clinical context. I have a deeper understanding of MRI, I am a clearer presenter, and I am a stronger person because of them.

Soonmee has been a driving force behind my graduate work. Soonmee is a renowned perfusion MRI researcher and radiologist, and gifted mentor to me. She took the time to teach me about clinically interpreting MRI exams and showed me how it really works in her reading room. Soonmee is the voice in my head when I make presentations, encouraging me to "speak to the clinician" and to make sure I'm clear on "what they will remember when they walk out of the room." Together, Soonmee and Susan kept me focused on the clinical impact of the work, something I am very grateful for.

Another strength of the JGGB Bioengineering program is that we also have access to mentors on the UCB side. I'd like to thank **Dr. Amy Herr** for her guidance in teaching through GSI-ing and guest lecturing in her undergraduate Biodesign course. Dr. Herr has continually supported my interest in biodesign and has been an inspiration to me as a woman-in-science able to merge both academia and industry. I'd also like to thank **Drew Isaacs** who led the Mayfield Fellows program and took time to mentor me on career choices. Drew showed me how to think about how biomedical research fits into an industry context. My exposure to Amy and Drew has been a large part of my inspiration to pursue Stanford's Biodesign Fellowship program.

I want to thank **Dr. Janine Lupo** for, quite literally, showing me how it's done. Simply put, Janine knows all. Getting to sit next to her and collaborate with her has greatly elevated my own work. She has been my example of how to write solid research,

how to present, and how to understand data. Janine is a talented and poised MR

researcher who I am proud to call my friend.

In addition to Janine, there were others that I saw as role models within the lab.
Dr. Kate Hammond-Rosenbluth, **Dr. Inas Khayal**, **Dr. Yan Li**, and **Dr. Ilwoo Park**
all completed the Bioengineering program ahead of me and demonstrated how to keep

balanced. Kate has been a very supportive friend to me throughout graduate school, Inas

first introduced me to managing clinical data, Yan has been a pleasure to sit next to

throughout graduate school, and Ilwoo continues to be my PowerPoint slide inspiration.

One of the best parts of graduate school has been the amazing group of people

I've been able to work with. I am always in awe of the amount of talent and enthusiasm

that permeates the Brain Group and Surbeck Labs. **Eugene Ozhinsky**, **Maryam Vareth**,
Qiuting Wen, **Wei Bian**, **Alex Constantin**, and **Trey Jalbert** are each amazing

bioengineering scholars that understand the value in collaboration. **Adam Elkhaled**,
Angela Jakary, **Andre Cote**, **Chris Williams**, and **Gabriela Bourne** have each been a

pleasure to work with, and without their resourcefulness in bridging the scanner to OR

this work would not have been possible. **Beck Olson** and **Jason Crane's** ingenuity in

building the software tools and imaging database are what enabled this work to happen. I

am so grateful for their patience and helpfulness in debugging software with me

throughout these projects. **Colleen Cloyd**, **Esin Ozturk**, **Julia Owen**, and **Ali Apple**
have been supportive and upbeat colleagues that have made conference going even more

enjoyable. I'd also like to thank **Gabby Joseph** for very kindly helping me through quals. I'd like to thank **Rupa Parvataneni** and **Mei-Yin Polley** for their statistical support of these projects.

My research has been greatly advanced by being able to work with many clinical collaborators at UCSF. I'd like to thank **Dr. Mekhail Anwar** for his work with the radiation-planning project and **Dr. Laleh Jalilian** for her work with diffusion and Avastin projects. Collaborating with Laleh has taught me a lot about the management of clinical data and combining results from different MRI techniques. I'd like to thank Laleh for being the lead author of the collaborative project presented in Chapter 6. I'd also like to thank **Dr. Ramon Barajas** for being the lead author of the large-scale collaborative project presented in Chapter 7. I'd like to also thank the neurosurgery and neuro-oncology team including **Dr. Nicholas Butowski**, **Dr. Mitch Berger**, **Dr. Manish Aghi**, and **Dr. Jennifer Clarke** who have made this work possible.

I'd like to thank my rotation-family: **Dr. Joe Osorio**, who got me setup in the lab and ceded to me the desk spot with view of the Bay that I've enjoyed the past five years; and **Christine Leon** and **Wenwen Jiang**, who taught me perhaps as much about managing projects as I taught them about MRI.

I want to thank **Mary McPolin** and **Niles Bruce** for all of their help with scanning. I'd like to send a special thanks to **Bert Jimenez** for being so accommodating

My family has been an incredible source of strength and support for me as I forged my way through graduate school. My parents, **Ed Essock** and **Barbara Burns**, have been my practice audience for all the shows, all the presentations, and all the papers I have done over my past 22 years of school (and there have been very, very many). They are shining examples of the spirit of academic pursuit meshed with the spirit of living fully. I also want to thank my sister, **Tara Essock-Burns**, for her encouragement of this pursuit. My parents have kept me buoyed, while my sister has kept me sane, and I am grateful for their support along this very long path.

I especially want to thank my boyfriend, **Michael Schump**, for being my partner on this journey. Mike has listened to me vent about, agonize over, rejoice in, and plan for all the projects in this dissertation (perhaps a little endlessly at times). He has kept me together after every bump along the course of graduate school and has celebrated with me after every victory. He's got my back and the world is a kinder place because of him.

Finally, thank you to the **Brain Group** for teaching me what it means to be a true collaborator and contributor. I will always be proud to have been part of this team.

The text of Chapter 5 is a reprint of the material as it appears in Neuro-Oncology:

Essock-Burns E, Lupo JM, Cha S, Polley MY, Butowski NA, Chang SM, Nelson SJ.
Neuro Oncol 2011;13(1):119-31.

The text of Chapter 7 is a reprint of the material as it appears in Neuro-Oncology with co-author permission:

Barajas RF, Phillips JJ, Parvataneni R, Molinaro A, Essock-Burns E, Bourne G, Parsa AT, Aghi MK, McDermott MW, Berger MS, Cha S, Chang SM, Nelson SJ. Neuro Oncol [accepted May, 2012]

Integration of Physiologic MRI to Improve Antiangiogenic Treatment Management for Patients with Glioblastoma

by

Emma Essock-Burns

ABSTRACT:

Advances in targeted therapies for patients with glioblastoma require simultaneous advances in noninvasive imaging in order to clinically manage these new treatments. Patients diagnosed with glioblastoma, a highly malignant form of brain cancer, have limited survival. Significant improvements in outcome for these patients will likely rest on both advances in targeted therapies and individualization of treatment regimens.

Standard clinical magnetic resonance imaging (MRI) provides insight into tissue structure and is used as a noninvasive surrogate marker of tumor presence. Physiologic MRI offers insight into tumor tissue physiology including surrogate markers of vascularization, cell density, and metabolic activity. The integration of physiologic imaging into the clinical exam has the opportunity to significantly improve decision making in the care of patients with brain cancer.

This dissertation project investigated dynamic susceptibility contrast (DSC) MRI and diffusion weighted (DWI) MRI as complementary methods for characterizing tumor burden prior to therapy and for assessing response during therapy. Specialized methods

for acquiring and post-processing DSC data were developed to be feasible in the clinical setting. Noninvasive surrogate markers of vascular morphology and histopathologic features were identified in de novo GBM. Initial vascularization and changes in permeability within the tumor measured with DSC MRI were found to relate to patient response to antiangiogenic therapy. DWI was used to detect treatment-specific changes in tumor burden in order to further develop biomarkers of response.

The results of this dissertation support integrating physiologic MRI into the clinical exam of patients with glioblastoma. DSC and DWI can provide valuable insight into tumor physiology, which will allow clinicians to better tailor treatments to individual patients and assess response to antiangiogenic therapy.

TABLE OF CONTENTS

LIST OF FIGURES:

LIST OF TABLES:

CHAPTER 1 : Introduction

_____

Patients diagnosed with glioblastoma multiforme (GBM), a highly malignant form of brain cancer, have an extremely poor prognosis. Without treatment, median overall survival of patients diagnosed with GBM is around 3 months. The development of the current standard-of-care treatment, surgical resection followed by combined radio- and chemotherapy, has led to significant improvements in survival. Despite these advances in care, median overall survival remains around 12 to 15 months. Further advances are likely to build upon tailoring specific therapies to patients by incorporating new prognostic markers and identifying early predictors of response.

In recent years, the development of new "antiangiogenic" therapies has generated excitement in the neuro-oncology field regarding the potential for using alterations in vasculature as a means to control tumor growth. Preliminary studies in patients with recurrent GBM reported a vast improvement in radiographic response and led to the accelerated approval of bevacizumab for this population. While a survival benefit has yet to be shown, these new therapies have greatly influenced the trajectory of neuro-oncology research. This has led to new challenges, such as the need for updated response assessment methods, as well as the opportunity to design individualized treatment plans based on tumor physiology. The lack of validated, predictive biomarkers to guide treatment is clearly a place where imaging is needed. As it provides a means for non-invasively assessing changes

in tumor vasculature, imaging is playing an important role in determining how to best utilize these new treatment options.

Magnetic resonance imaging (MRI) is a critical tool in the clinical management of patients with GBM, with anatomic images having been used to direct surgery and other focal therapy, as well as assess response to treatment. Advances in physiologic MRI, including perfusion-weighted imaging, diffusion-weighted imaging, and metabolic imaging, has lead to a number of different markers that may lend insight into tumor physiology. The integration of these physiologic markers into the management for patients with GBM, holds significant promise for improving clinical outcomes. In order for these markers to be translated to the clinic there are many technical and biological challenges that need to be addressed. The goal of this dissertation project was to develop and apply physiologic imaging techniques to guide the assessment of response to antiangiogenic therapy for patients with glioblastoma. This dissertation is organized into six major projects.

In **Chapter 2**, I review the clinical background of brain cancer, antiangiogenic therapy, and methods for evaluating response to therapy. The basic concepts of MRI are presented with a focus on the challenges of assessing response in the context of antiangiogenic therapy. Physiologic MRI is introduced with an emphasis on diffusion and perfusion imaging methods. The chapter concludes with a discussion of current research on perfusion and diffusion MRI in brain tumor management and the challenges that face clinical integration.

In **Chapter 3**, I describe a study in which we directly compared vascular parameters derived from dynamic susceptibility contrast (DSC) MRI to vascular histopathology found

in tissue samples from patients with GBM prior to treatment. This was a highly cross-disciplinary project supported by the Graduate Education in Medical Science (GEMS) program and co-advised by Dr. Joanna Phillips (Department of Pathology), Dr. Susan Chang (Neurological Surgery), and Dr. Sarah Nelson (Bioengineering and Therapeutic Sciences). The goal of this project was to determine which common post-processing methods best described underlying vasculature. Blood volume estimates calculated from nonlinear and non-parametric analyses were found to predict vascular morphology. These post-processing methods are then used in the subsequent chapters.

Building upon these pathology results, **Chapter 4** explores two acquisition methods to address a primary technical challenge that inhibits the clinical use of DSC-MRI: leakage contamination. One method that is gaining attention in the field is to apply a "preload" of gadolinium prior to DSC acquisition, but the trade-off is that it increases the cumulative gadolinium dose and associated risks to patients. While a preload has been shown to improve high flip angle DSC data, the goal of this project was to determine whether a preload was still needed for leakage correction when acquired with a low flip angle. Blood volume calculated from low flip angle DSC data was found to be highly repeatable with or without a preload. This results of this project support acquiring DSC-MRI with a low flip angle and without a preload as it yields physiologically relevant measures of blood volume (**Chapter 3**) without increased risk due to greater gadolinium exposure.

In **Chapter 5**, we apply the DSC-MRI analysis and acquisition methods developed in **Chapters 3** and **4** to identify biomarkers of response to antiangiogenic therapy. Serial changes in perfusion characteristics of the tumor are assessed in patients receiving standard chemo- and radiotherapy with adjuvant and concurrent enzastaurin, an antiangiogenic

therapy. The initial vascularization of the tumor and the vascular permeability after two months of therapy are found to be predictive of response. This work provides evidence for how DSC-MRI can augment standard anatomic MRI in order to improve antiangiogenic treatment management.

Chapter 6 describes a collaborative project that expands on the development of biomarkers by investigating treatment-specific changes in diffusion-weighted MRI. This project was led by Dr. Laleh Jalilian, currently a radiology resident at Stanford University. As the second author on this work, my contributions included data processing, analysis of results, and editorial review. The differences in the diffusion patterns among patients treated with radiotherapy in addition to standard temozolomide (TMZ) therapy, TMZ with enzastaurin, or TMZ with bevacizumab, provide context for future treatment-specific biomarker development.

Chapter 7 is a further collaborative project that was based on the work of a large cross-disciplinary team. The goal of this project was to relate physiologic MRI parameters to tumor histopathology in order to guide tissue sampling within the heterogeneous GBM lesion to improve diagnosis. The first author of this paper is Dr. Ramon Barajas, a radiology resident at UCSF. My contributions to this work included analyzing the perfusion data, making the figures, and assisting with editing for publication. The results of this project support the integration of physiologic imaging, including DSC and diffusion-weighted MRI, with anatomic MRI to better characterize both the contrast-enhancing and non-enhancing components of GBM at diagnosis.

Finally, **Chapter 8** discusses the main conclusions from this dissertation. This chapter emphasizes how the research presented advances the overarching goal of this body of work, the integration of physiologic MRI to improve the clinical management of patients with GBM.

CHAPTER 2 : Background

This chapter provides an overview of brain tumor disease and clinical management with antiangiogenic therapy. Magnetic resonance imaging (MRI) is introduced as the primary method for diagnosing brain cancer and for monitoring response to therapy. Physiologic MRI, including diffusion weighted imaging (DWI) and perfusion imaging, are introduced as complementary methods, while highlighting the current engineering challenges that hinder their use in the clinic. Finally, the potential for physiologic MRI to improve the clinical management of patients with brain tumors is discussed in the context of current clinical usage.

2.1 Brain Tumor Disease: Prevalence and Incidence

Recent studies project that for every 100,000 people in the United States, 209 are living with the diagnosis of a primary brain tumor [1]. The incidence rate of primary brain tumors increases with age and the median age of diagnosis for all brain tumors is 57 years old [2]. While primary brain tumors are much more common in adults than children, they are more likely to be malignant in children (65.2%) compared to adults (33.7%) [3]. Although brain cancer comprised only 1.44% of all primary malignant cancer diagnoses in the United States during 2010, it continues to have disproportionally high morbidity and mortality rates. In particular, brain tumors are the second leading cause of cancer-related deaths in children under 20 as well as in males ages 20-39 and the fifth leading cause of cancer-related deaths in females 20-39 [4].

Of the 22,500 malignant primary tumors of the brain and spinal cord that are diagnosed in the United States each year, it is estimated that seventy percent are gliomas, originating from glial cells [5]. Glial cells are one of the major cell populations in the brain and have four sub-types: astrocytes, oligodendrocytes, ependymal cells, and microglia. Astrocytes are the most abundant and have diverse functions, including providing structural support and neurotransmitter metabolism. Oligodendrocytes produce myelin, the conductive, fatty sheath surrounding the neuronal axons. Microglia digest cell debris, in a manner similar to macrophages. Ependymal cells line the ventricles and form blood- cerebral spinal fluid (CSF) border. Sub-types of glioma are named according to the cells from which they originate.

2.2 WHO Malignancy Grading

Gliomas are characterized using the World Health Organization (WHO) criteria on a four-tiered scale. Five histologic features form the basis for this definition: nuclear atypia, cellular density, mitotic activity, endothelial proliferation, and presence of necrosis [6]. Grade I gliomas are benign, slow-growing, and have the best prognosis. They include piliocytic astrocytomas, which most commonly occur in children. Although they are hypercellular, they do not include any of the five features of malignancy. Grade II gliomas are relatively slow growing, but can transform to a higher grade at the time of recurrence. The major sub-types are diffuse astrocytomas, oligodendrogliomas, and oligoastrocytomas. They have moderately increased cellular density and presence of nuclear atypia, but lack mitotic activity, necrosis, and endothelial proliferation. Grade III gliomas are considered "high-grade" and have increased mitotic features. Grade IV gliomas are the most malignant subtype and have high cellular density, marked nuclear atypia, elevated mitotic activity, presence of necrosis, and/or endothelial proliferation. The most common sub-type of grade IV glioma is glioblastoma (GBM). As this dissertation is focused primarily on using new physiologic MR-imaging techniques to aid in the diagnosis and treatment management of GBM, the next section focuses on the histopathologic features and characterization of these lesions.

2.3 Glioblastoma

GBM represent 53.7% of all primary gliomas in adults [7]. Their incidence is 1.6 times higher in males than in females and they typically occur between 65 and 84 years of age in the United States [7]. Despite advances in care, overall survival (OS) remains limited at approximately 15 months for patients with newly diagnosed GBM [8] and 30 weeks for

patients with recurrent GBM [9]. In addition to elevated mitotic activity, high cellular

density, and marked nuclear atypia, two hallmark features of GBM are the presence of

necrosis and/or microvascular proliferation.

A major issue in evaluating GBM is that they are extremely heterogeneous, both

within the tumor mass and in the presentation between patients. It is common for a large

portion of the central region to be necrotic, with a contrast-enhancing outer rim on T1-

weighted post-contrast MRI (see section 2.6). Central necrosis is an indication that the

actively proliferating tumor has outgrown its blood supply, causing the central tissue to

become hypoxic and ultimately necrotic. The presence of a hypoxic tumor microenvironment

triggers the expression of a variety of pro-angiogenic growth factors such as hypoxia

inducible factor (HIF)-1α. Accumulation of HIF-1α induces expression of the vascular

endothelial growth factor (VEGF), which represents a family of growth factors that act as

potent vasodilators and mediators of microvascular permeability. VEGFA is the most

common member of the VEGF family of proteins that is overexpressed in gliomas [10].

Extracellular binding of VEGFA triggers activation of the VEGF pathway leading to

increased vascular permeability, endothelial cell proliferation, and angiogenesis to sustain

tumor growth. The activation of angiogenesis is believed to be key in the transition from a

grade III lesion to a GBM [10].

2.4 Angiogenesis and Vascular Pathology of Glioblastoma

The driving process behind angiogenesis is often described as the "angiogenic switch"

[11] and can be visualized as a scale that balances pro- and antiangiogenic factors as shown

in **Figure 2.1**. Angiogenesis was previously thought to be primarily reliant on the growth of

new capillaries from existing vasculature but recent research has shown that there may be multiple, often simultaneous, mechanisms. In addition to classic "sprouting" angiogenesis, GBM may undergo neovascularization through "co-option" of pre-existing normal blood vessels and vasculogenesis, and de novo formation of new vasculature, through recruitment of bone-marrow derived endothelial precursor cells to the brain [12-13].

Figure 2.1: "Angiogenic Switch" Hypothesis
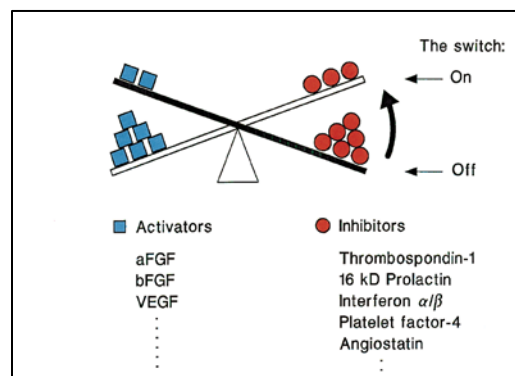
Figure 2.1: The misregulation of proangiogenic and antiangiogenic factors causes the scale to tip, activating the normally quiescent vasculature to undergo angiogenesis. (Figure reprinted from "Patterns and emerging mechanisms of the antiangiogenic switch during tumorigenesis," Hanahan et. al. Cell, 1996 [11], with permission from Elsevier.)

In normal brain, there are tight junctions between endothelial cells that create a selective "barrier" between brain tissue and blood vessels. This blood-brain barrier (BBB) comprises endothelial cells, pericytes, astrocytic perivascular feet projections, and a thick basement membrane. The intact BBB allows efficient delivery of blood and nutrients and serves to protect the brain parenchyma against infection. In the tumor environment, activation of the angiogenic switch leads to detachment of pericytes, degradation of the basement membrane, migration of endothelial cells into the perivascular space, and proliferation of endothelial cells to form lumen that ultimately fuse together into new vascular channels [10]. Unregulated tumor angiogenesis leads to overabundant, unstructured growth of microvasculature. The newly formed tumor vasculature is often hemorrhagic, dilated, and tortuous. Along a vessel there may be irregularly spaced sub-branches of microvasculature, often with dead ends. Complex glomeruloid microvasculature is a hallmark of GBM and is characterized by multiple lamina and breakdown of the blood brain barrier. The microvascular morphology can be identified using Factor VIII immunohistochemical staining of endothelial cells. **Figure 2.2** shows an example of complex glomeruloid microvasculature in a patient newly diagnosed with GBM. Note the proliferative endothelium and double lamina (arrows).

Figure 2.2: Factor VIII immunohistochemical staining of glomeruloid microvasculature in de novo GBM
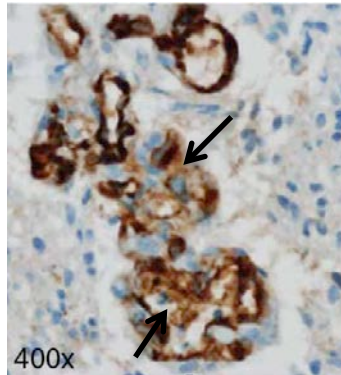
2.5 Antiangiogenic Therapy for Patients with GBM

The standard therapy for patients newly diagnosed with GBM comprises maximal safe surgical resection, followed by radiotherapy and chemotherapy. Radiotherapy is typically delivered in thirty fractions of 2Gy that are given for 5 days per week over a period of 6 weeks. In 2005, Stupp et al. reported a significant increase in progression-free survival (PFS) and overall survival of newly diagnosed GBM patients with the addition of concomitant and adjuvant temozolomide, which is an oral alkylating agent. Patients treated with temozolomide had a median overall survival of 14.6 months compared to 12.1 months with radiotherapy alone [14], which established it as the new standard of care for GBM.

The highly vascularized nature of GBM and the key role that angiogenesis plays in the growth and progression of gliomas, means that disruption of the angiogenic pathway is an attractive target for therapeutic development. A variety of intra- and extracellular strategies that can disrupt and impede tumor angiogenesis are under investigation [13, 15-17]. Strategies

Figure 2.3: VEGF pathway with antiangiogenic therapeutics and their targets
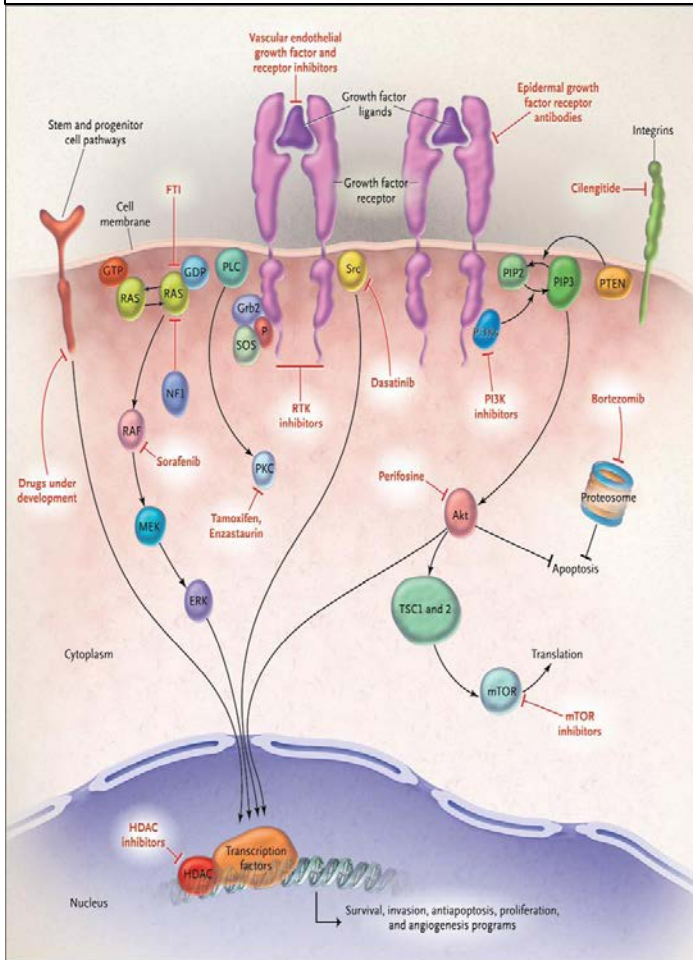
[Reproduced with permission from Malignant Gliomas in Adults. P. Wen and S. Kesari, New Eng J Med. 2008, July, Copyright Massachusetts Medical Society]

include sequestering circulating VEGF to reduce cell-surface VEGFR activation (bevacizumab, alfibercept), pan-VEGFR tyrosine kinase inhibitors (cediranib), broad-spectrum tyrosine kinase inhibitors (sorafenib, sunitnib, XL-184), intracellular protein kinase inhibitors (enzastaurin), and many others. **Figure 2.3** displays a variety of antiangiogenic therapeutics and their targets [18].

Enzastaurin disrupts the phosphorylation of the β-isoform of protein kinase-C (PKC), which lies on the VEGF signaling pathway, thereby inhibiting tumor angiogenesis (**Figure 2.3**) [19]. Preclinical data have supported the notion that enzastaurin induces apoptosis in addition to reducing angiogenesis [20]. A recent phase II trial showed enzastaurin was well tolerated in an upfront treatment setting for patients with GBM, and showed a moderate improvement in overall survival (OS) compared to historical controls (thalidomide with temozolomide and RT; cis-retinoic acid with temozolomide and RT; and erlotinib with temozolomide + RT), but the improvement may be attributable to improvement in care for GBM, rather than to the use of a novel agent [21].

13

A phase III trial in patients with recurrent GBM comparing enzastaurin to lomustine, which is an oral cytotoxic chemotherapeutic, showed that enzastaurin was well tolerated but did not provide a significant progression-free survival or overall survival advantage [22].

Bevacizumab (Avastin®, Genentech/Roche) is a humanized monoclonal antibody that binds with circulating, extracellular VEGFA, thus intercepting the activation of VEGFR and subsequent angiogenesis. Initial histopathological studies have shown evidence of reduced microvessel density and apparent vascular "normalization" following treatment with bevacizumab [23]. It has been shown to reduce the permeability of vasculature, thereby alleviating edema and reducing the required steroid dose for patients with recurrent GBM [24-25]. Improved function through antiangiogenic-induced vascular normalization has been hypothesized to improve the delivery of concomitant cytotoxic chemotherapeutic agents to the tumor [26].

In 2009, bevacizumab received accelerated approval from the U.S. Food and Drug Administration (FDA) for use as a single-agent in recurrent glioblastoma patients based on early evidence of radiographic response [27-28]. This was a key step in integrating antiangiogenic therapy strategies into the clinical care of patients with malignant glioma and raised important clinical questions about the evaluation of response (see Sec. 2.7). In order to address these critical questions, a more detailed understanding of the effects of angiogenesis on imaging appearance and the physics behind MR image contrast is needed.

2.6 MRI of Brain Tumors: Diagnosis, Therapy Selection, and Treatment Management

MRI is the preferred imaging modality for the diagnosis of brain tumor disease and for assessing response to therapy due to its high soft-tissue contrast. Contrast is based on the relative relaxation properties of hydrogen protons (spins) when placed in a uniform magnetic field. At rest, these spins are randomly aligned, but in the presence of an external magnetic field (B0) they align parallel or antiparallel to B_0. A slight excess of spins remain in the aligned, lower energy state resulting in a net magnetization vector, M_0. The distribution of spins in the higher (n-) and lower (n+) can be described as:

$$ {n^-}/{n^+} = \exp\left({-\gamma B_0}/{kT}\right), \qquad \text{(Eq. 3.1)} $$

where k = Boltzmann's constant (1.381×10^{-23} JK^{-1}), T = temperature in Kelvin (body ≈ 310 K), and γ = gyromagnetic ratio (42.58 MHz/T for H^1 proton.)

An excitation radiofrequency pulse (B_1) can be delivered to the system perpendicularly to B_0 at the frequency f=($\gamma/{2\pi}$)B_0 to flip the parallel spins into the antiparallel, elevated energy level state. The change in energy between these quantum states is defined by:

$$ \Delta E = {h\gamma}/{2\pi}, \qquad \text{(Eq. 2.2)} $$

where h = Planck's Constant (6.626×10^{-34} m^{2}kg/s).

Using a classical description, this pulse can also be visualized as tipping the magnetization vector into the transverse plane (**Figure 2.4**). The angle between the B_0 field and the magnetization vector M is called the flip angle and depends on the B1 field and time (τ) it is applied:

$$\alpha = \gamma B_1 \tau \qquad\qquad (\text{Eq. 2.3})$$

Figure 2.4: Diagram of M precession
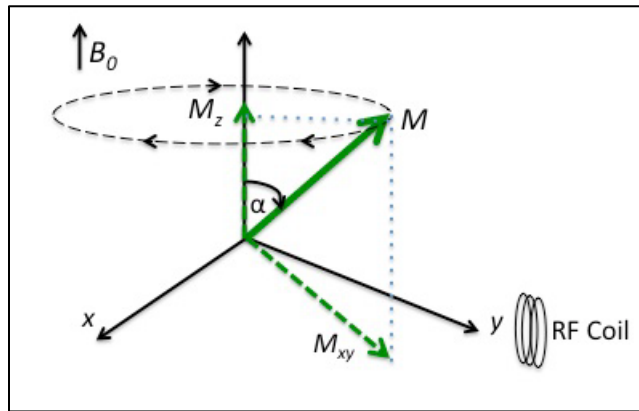
Figure 2.4: After excitation, M is tipped away from the B_0 axis through angle α and

precesses about B_0 with $M_{xy}(t)$ and $M_z(t)$.

After the B_1 pulse, the magnetization vector M precesses about the z-axis at the

Larmor frequency, $\frac{\lambda}{2\pi} B_0$. There are two methods by which M returns to its initial M_0 state,

which are described by two time constants: T_1 and T_2.

Longitudinal relaxation is the process by which spins release energy into the

surrounding lattice environment allowing the longitudinal magnetization (M_z) to recover to

equilibrium M_0. The growth of M_z is defined by equation 2.4 and illustrated in Fig. 2.5.a.

T1 is the rate constant that describes this process and is defined by the time it takes for Mz to recover to 63.2% of M0.

$$Mz(t) = M_0(1 - e^{\left(-\frac{t}{T_1}\right)})$$
(Eq. 2.4)

Transverse relaxation is the process by which spins lose their coherence through spin-spin interactions and the transverse magnetization (M_{xy}) recovers to zero. This is most frequently due to slowly fluctuating or static field variations within tissue, causing individual spins to experience a slightly different magnetic field. This causes the spins to resonate at slightly different frequencies resulting in a temporary gain or loss of phase with respect to the other spins. The resulting loss of coherence or "dephasing" reduces the net transverse magnetization, M_{xy}, and is governed by equation 2.5. T_2 is the rate constant that describes this process and is the time it takes for M_{xy} to decay to 36.8% of original M_{xy} component. **Figure 2.5.b** illustrates the rate at which M_{xy} dephases.

$$M_{xy}(t) = M_0 e^{\left(-\frac{t}{T_2}\right)}$$
(Eq. 2.5)

In practice, magnetic field inhomogeneity and susceptibility effects also cause spin dephasing thereby decreasing M_{xy} even faster. T_2^{*} is the time constant that describes the loss of coherence due to external field inhomogeneities (T_{2i}) as well as intrinsic, non-reversible T_2 dephasing. T_2^{*} is described by equation 2.6.

$$T_2^{*} = \frac{1}{T_2} + \frac{1}{T_{2i}}$$
(Eq. 2.6)

Figure 2.5: Plots of Mz and Mxy
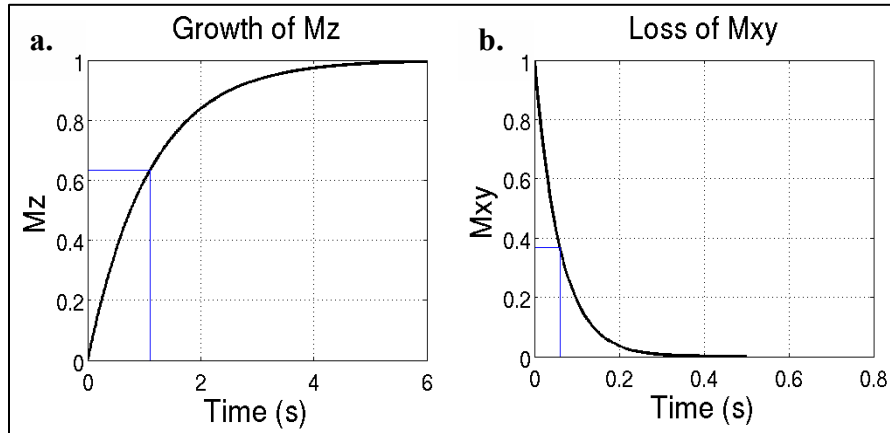
Figure 2.5. Plots showing M_z (a) and M_{xy} (b) over time. The blue line highlights T_1 (63.2% growth of Mz) and T_2 (decay to 36.8% of Mxy).

The T_1 and T_2 relaxation rates are key to generating contrast in MR images. They are strongly influenced by the water content of tissue. Table 2.1 describes the T_1 and T_2 for major regions of the brain. The presence of pathology also can greatly affect T_1 and T_2 rate constants, which is why MRI is such a useful tool for diagnosing disease. Contrast in MR images can be manipulated by altering acquisition parameters, such as repetition time (TR) between excitations and time to form an echo (TE), to highlight sensitivity to differences in relaxation rates.

Table 2.1: Examples of T_1 and T_2 at 1.5 Tesla (T) and 3.0 T in the human brain [29].

Brain Tissue	T1		T2	
	1.5 T	3.0 T	1.5 T	3.0 T
White Matter	884 ms	1100 ms	72 ms	60 ms
Gray Matter	1124 ms	1800 ms	95 ms	70 ms

T_1-weighting is controlled by TR, while T_2-weighting is controlled by TE. Sequences with short TR accentuate differences in the amount M_z has recovered, and produce images with brighter signal in region where T_1 is short. Sequences with long TE accentuate differences in the amount of M_{xy} dephasing, thus generating images with bright signal where there is long T_2. Table 2.2 demonstrates how altering TR and TE can change the T_1 and T_2 weighting of image contrast. Rapidly tumbling molecules in fluid-like suspension interact with many local inhomogeneities so the net effect on spin dephasing is lessened leading to longer T_2. This means that in T_2-weighted images, fluids such as CSF appear bright. Tissues with macromolecules that tumble near the Larmor frequency facilitate spin-lattice energy transfer, which leads to a shorter T_1. This means that tissues with high lipid concentration appear bright in T_1-weighted images. MR signal (S) is dependent on the TR, TE, T_1, T_2, and the spin population (ρ) as described in equation 2.7).

$$S = \rho(1 - e^{-\frac{TR}{T_1}})e^{-TE/T_2} \qquad \text{(Eq. 2.7)}$$

Table 2.2: Relationship of TE and TR to imaging weighting

Image-Weighting	TE	TR
T1-weighted	Short	Short
T2-weighted	Long	Long
Proton Density-weighted	Short	Long

Another way to generate contrast is to introduce an intravenous contrast agent that reduces T_1. This is possible using Gadolinium-based contrast agents, which carry unpaired electrons in their outer shell, and result in electron spin resonance. This increases the rate of transfer of energy to the lattice and shortens T_1 in nearby tissue. These agents do not pass through the BBB in normal tissue, but, in regions with compromised BBB, which is common in vasculature formed through uncontrolled angiogenesis, gadolinium can leak out of the intravascular space. This makes gadolinium contrast agents useful for identifying regions of BBB disruption and is the reason why contrast-enhancement has been historically used as a surrogate for tumor presence in GBM.

Patients who present with headaches or seizure are referred for an MRI exam of the brain. A standard exam of the brain includes T_1-weighted images, with and without contrast, and T_2-weighted images. Radiologists review the images to identify suspicious features such as presence of an enhancing mass, volume effect, and T_2 hyperintensity. **Figure 2.6** shows an example of a patient with de novo, treatment-naïve GBM which is depicted by a region of T2 hyperintensity on a fluid-attenuated inversion recovery (FLAIR) image (a) collapsing of the patient's right ventricle due to obvious mass effect (b), and a region of contrast-enhancement seen by T1-weighted post-contrast hyperintensity (c).

Figure 2.6: FLAIR and pre- and post-contrast T1-weighted MRI of patient with GBM
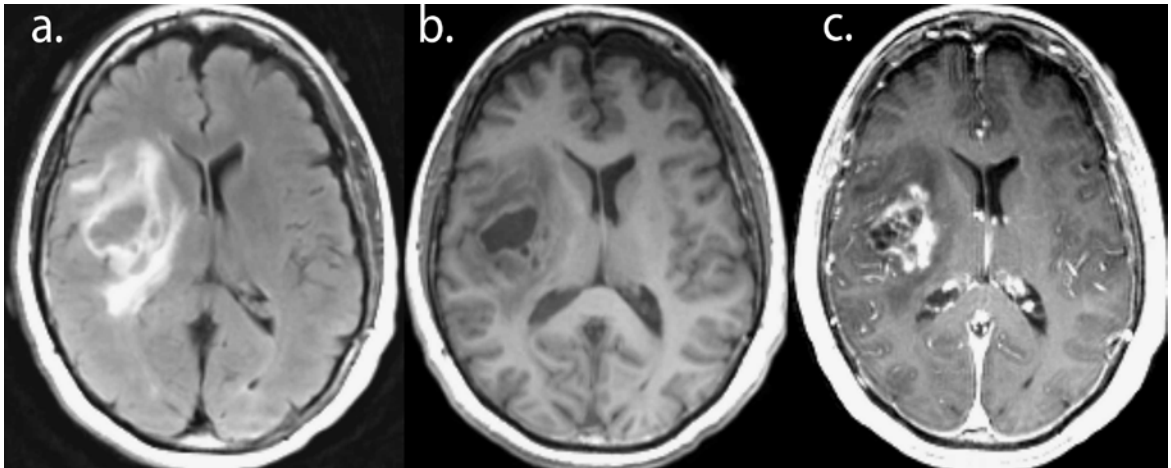
Figure 2.6: T2-weighted FLAIR (a), T1-weighted pre-contrast (b), and T1-weighted post-contrast (c) MR images at 3 Tesla of a patient newly diagnosed with GBM.

If the imaging exam shows evidence of such features, the patient will undergo biopsy and/or surgical debulking. Histologic analysis of the tissue samples acquired during these procedures are examined to identify the most malignant features and define the grade of the tumor. As discussed in section 2.5, standard therapy includes combined radiation therapy and temozolomide.

2.7 Methods for Evaluating Response to Therapy using MRI

Following initiation of treatment, patients with GBM continue to receive serial MRI exams, at approximately 2-month intervals. Decisions about further treatment are based upon changes in the anatomic lesion that are observed on T_1-weighted, pre- and post-contrast, and T_2-weighted MRI exams. Until recently, the evaluation of response to

treatment were based on the Macdonald criteria, which used changes in the area of contrast-enhancement on T_1-weighted post-contrast MRI combined with variations in steroid use and neurologic status **(Table 2.3)** [30].

Table 2.3: Summary of response assessment based on classic Macdonald criteria [28].

Macdonald Criteria Response Assessment				
	Complete Response (CR)	**Partial Response (PR)**	**Stable Disease**	**Progression**
MRI Evaluation: Area of T1-weighted contrast-enhancement (relative to baseline exam)	Disappearance for ≥ 4 weeks, No new lesions	Decrease of ≥ 50%, No new lesions	No CR, PR, nor progression	Increase of ≥ 25%, New Lesions
	AND	AND	AND	OR
Clinical Evaluation: Neurologic Status, Corticosteroid Use	Clinically stable or improved, No steroids	Clinically stable or improved, Reduced or Stable Steroid Use	Clinically stable	Clinical deterioration

2. 8 Clinical Challenges in Evaluating Response to Antiangiogenic Therapy

One of the central challenges in assessing response to antiangiogenic therapy is that the therapy itself can alter the presentation of contrast enhancement, making its use as a surrogate marker of response suspect. The anti-permeability effects of antiangiogenic agents restore the BBB, which reduces the amount of contrast enhancement observed on T1-weighted post-contrast MRI. This is problematic for radiologists as patients may present with a large decrease in contrast enhancement as in **Figure 2.7**, which may or may not be indicative of a reduction in tumor cells.

Figure 2.7: Challenge of assessing response to antiangiogenic therapy with metrics based on T1-w contrast-enhancement
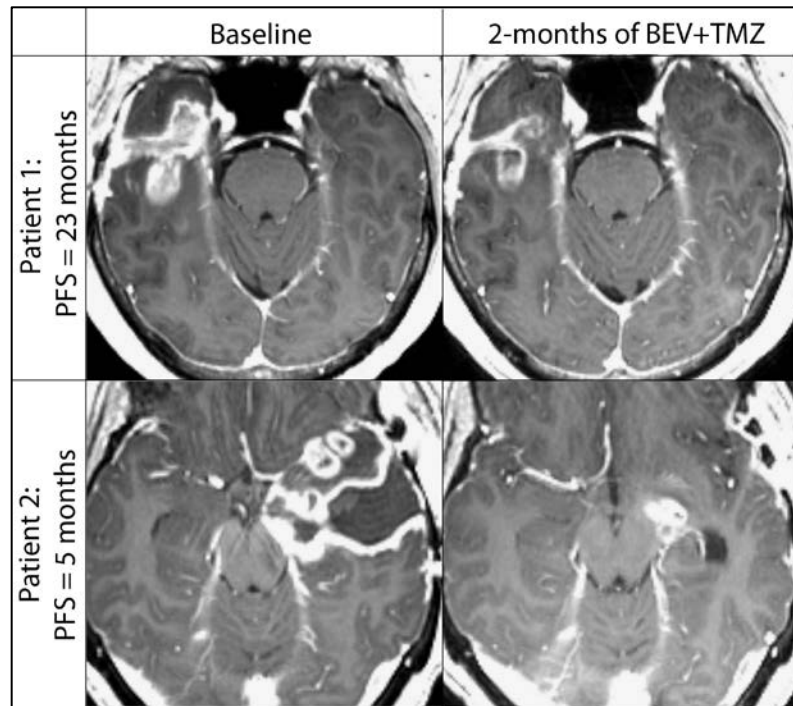
Figure 2.7 T1-weighted post-contrast MRI of two patients newly diagnosed with GBM at baseline (left) and after 2 months of combined radio- chemotherapy including bevacizumab (BEV) and standard temozolomide (TMZ). Both Patient 1 (top) and Patient 2 (bottom) demonstrate a large decrease in contrast-enhancement after 2 months of therapy. Patient 1 had a prolonged progression-free survival (PFS) of 23 months, but despite this early reduction in contrast-enhancement, Patient 2 progressed after only 5 months.

The need for updated methods for evaluating response to antiangiogenic therapy was highlighted by the accelerated approval of bevacizumab (see sec 2.5 for drug description). Two prospective phase II studies (AVF3708g, NCI 06-C-0064E) showed adjuvant bevacizumab in the recurrent setting greatly improved radiographic response (overall response

rates of 28.2% [27] and 35% [28]) compared to historical controls (less than 10% [31]). For both studies, radiographic response was defined based on standard contrast-enhancement based methods adjusted for steroid use. The limited overall survival rates of patients with recurrent GBM, few available therapeutic options, and significant improvement in radiographic response, were important factors in the FDA's decision to advance this drug into the clinic. Clinical trials are currently underway in both the upfront and recurrent setting [32-35]. Questions about quality of life following prolonged bevacizumab exposure also remain [36-39]. If the ongoing trials are unsuccessful, the FDA will revoke the drug approval, as they did in 2011 for the accelerated approval of bevacizumab for patients with breast cancer. This highlights the importance of understanding the physiology behind surrogate markers in the context of antiangiogenic therapy.

In 2010, the Response Assessment in Neuro-Oncology (RANO) working group published updated criteria to address some of the limitations of conventional assessment methods [40]. The main update was to include changes in the non-enhancing component of the tumor, as depicted by hyperintensity on T2-weighted or FLAIR MRI, in the assessment of response. The RANO group also proposed that patients who progress within 12 weeks of the completion of radiotherapy should only be included in trials for patients with recurrent disease if the progression was outside the high-dose radiation region or with histologic confirmation in order to better distinguish between pseudo-progression and progression. RANO also clarified that patients without measurable disease (less than 1 cc of residual tumor, for example, following a gross-total resection) could at best have stable disease. Table 2.4 summarizes the updated RANO criteria. The potential for using physiologic imaging to aid in response assessment was recognized but it was felt that the current

understanding of these markers was not sufficient for inclusion into clinical standards at that time.

Table 2.4: Summary of response assessment based on 2010 RANO criteria [40].

2010 Updated RANO Criteria Response Assessment				
	Complete Response (CR)	**Partial Response (PR)**	**Stable Disease**	**Progression**
MRI Evaluation: Area of T1-weighted contrast-enhancement (relative to baseline exam)	Disappearance for ≥ 4 weeks, No new lesions	Decrease of ≥ 50%, No new lesions	No CR, PR, nor progression	Increase of ≥ 25%, New lesions
	AND	AND	AND	OR
MRI Evaluation: Area of T2/FLAIR non-enhancing lesion (relative to baseline exam)	Stable or improved	Stable or improved	Stable	Significant increase (with stable or increased steroids)
	AND	AND	AND	OR
Clinical Evaluation: Neurologic Status, Corticosteroid Use	Clinically stable or improved, No steroids	Clinically stable or improved, Reduced or equivalent steroid use as baseline	Clinically stable, Reduced or equivalent steroid use as baseline	Clinical deterioration

The accelerated approval of bevacizumab and the recommendations of the RANO working group serve to highlight critical questions regarding the interpretation of MRI data in the context of antiangiogenic therapy. The identification of alternative, reliable biomarkers of response and the development of noninvasive methods for characterizing microvasculature are critical for moving forward. This dissertation focuses on improving the management of patients with glioblastoma through the development and application of physiologic MRI techniques to the assessment of antiangiogenic therapy.

2.9 Physiologic MR-Imaging

Advanced imaging methods that can be used to monitor physiologic and metabolic changes in the brain will be especially useful in diagnosing the highly heterogeneous GBM disease and assessing response to antiangiogenic therapy. Recent studies have investigated the use of such methods for aiding in the diagnosis of disease, individualizing targeted therapies for patients, and predicting progressive disease. Options considered include diffusion-weighted imaging (DWI), perfusion imaging, and MR metabolic imaging. The focus of this dissertation is perfusion and diffusion imaging. The use of metabolic imaging is outside of the scope of this dissertation project and has been reviewed elsewhere [41-43]. Perfusion and diffusion imaging are currently being acquired as part of standard serial imaging for brain tumor patients, but how to apply these techniques and translate the findings into clinical practice needs further research.

DWI applies multiple gradients in different directions to measure the amount of water diffusion that occurs within the tissue of interest. Quantitative parameters that are estimated from such data are the apparent diffusion coefficient (ADC), which is reflective of tissue cellularity, and fractional anisotropy (FA), which measures the disruption of tissue architecture. DWI is of interest for clinical applications in GBM because it may guide selection of tissue samples to the most cellular regions and provide better characterization of the T2 lesion (T2L), which can contain a mixture of infiltrative tumor and regions of edema. For patients with GBM, the median ADC in the T2L is around 1.5 times and in the contrast

enhancing lesion is around 1.4 times greater than in NAWM [44]. Lower ADC values indicate restricted diffusion, which has been interpreted as corresponding to higher tumor cellularity. Higher ADC values reflect increased movement of water molecules, which has been interpreted as edema, necrosis and/or gliosis with elevated tissue disruption. Advantages of DWI are that it can be used to estimate quantitative measures of tissue properties, necessitates no additional gadolinium, and is relatively straightforward to add to a clinical exam. One of the challenges in using DWI is in knowing how to correctly interpret increases in ADC following radiotherapy and adjuvant antiangiogenic therapy, which can result in a reduction in tumor cellularity and an increase in treatment-induced gliosis, necrosis, and edema.

Common methods for analyzing serial changes in DWI include histogram analysis and the use of functional diffusion maps (fDM). The latter quantifies early (1-4 week) voxel-by-voxel change in ADC within the same patient [45-46]. More recently, the rate of change that is observed in the T2 lesion with fDM has been shown to predict OS in a population of patients with recurrent GBM who were treated with antiangiogenic therapy [47]. Since DWI parameters reflect changes to the composite tissue architecture, which can be altered from multiple treatment-related processes, one of the major challenges to transitioning them into the clinic is in understanding therapy-specific changes. **Chapter 6** characterizes differences in the early pattern of ADC changes between conventional and antiangiogenic therapies in the newly diagnosed setting in order to describe the context for future biomarker development.

2.10 Perfusion Imaging: DCE

Another physiological MR-imaging technique is perfusion MRI. This has been used to assess vascular function by tracking the relaxation effects of injected gadolinium as it circulates through the brain. Rather than highlighting regions where gadolinium contrast has previously leaked out of the vasculature through the disrupted BBB, perfusion MRI highlights the time-course of changes in image contrast due to alterations in relaxation times. These dynamic data can be used to describe functional characteristics of the underlying vasculature, which provide unique insights into response to antiangiogenic therapy. There are two primary types of perfusion imaging that use contrast agents: dynamic contrast-enhanced imaging (DCE) and dynamic susceptibility imaging (DSC).

DCE-MRI is commonly used to generate a robust estimate of permeability and utilizes images that are acquired with T_1-weighting. It tracks the magnitude of signal enhancement resulting from the gadolinium that leaks from the intravascular to the extravascular-extracellular space (EECS). Three main models (Tofts, Larsson, and Brix) have been proposed for analyzing DCE data. They are based on modeling the pharmacokinetics of tracer concentration between these compartments, which are determined by three physiologic factors: capillary surface area and permeability to gadolinium, volume of the extracellular leakage space, and tissue perfusion. Assumptions in these models include a well-mixed tracer concentration within each compartment, slow clearance of the contrast between the plasma and kidneys, and sufficient flow as to not reduce the plasma concentration through leakage. **Figure 2.8** describes the classic Tofts and Kermode compartmental model.

Figure 2.8: Tofts and Kermode Compartmental Model
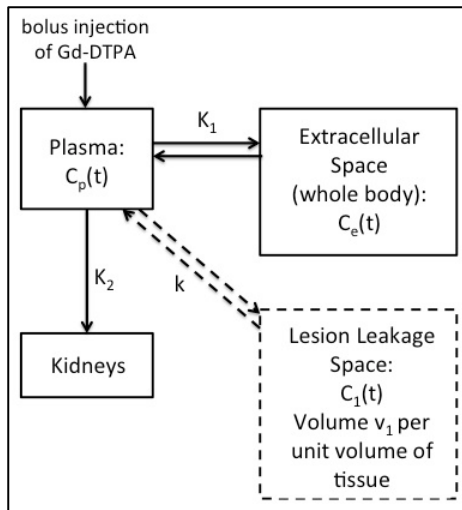
Figure 2.8: Tofts and Kermode original compartmental model of gadolinium contrast distribution [48]. A bolus of contrast is injected to the plasma compartment. The solid line compartments represent clearance of gadolinium to the kidneys and extracellular space throughout the body (but not the brain due to BBB). Tofts and Kermode added the dotted line compartment to represent the lesion leakage space compartment connected by a permeable membrane.

The concentration of gadolinium in a unit of tissue is defined as the sum of both the concentration in the plasma compartment (C_p) and the concentration in the EECS compartment (C_e) weighted by the volume fraction of available space accessible to the tracer of plasma (v_p) or EECS (v_e) (equation 2.8).

$$C(t) = v_p C_p + v_e C_e \qquad\qquad (Eq.\ 2.8)$$

Based on pharmacokinetic theory (Fick's Law), the rate of change of the concentration of a tracer in EECS compartment (or mass of the tracer per v_e) is equal to the difference in the concentrations of the two compartments weighted by the transfer coefficient (K_{trans}) of the membrane separating them (equation 2.9).

$$\frac{dC_e(t)}{dt} = \frac{K_{trans}(C_p - C_e)}{v_e} \qquad \text{(Eq. 2.9)}$$

Thus, concentration of Gadolinium in the EECS can be expressed as:

$$C_e(t) = \frac{K_{trans}}{v_e} \int_0^t (C_p - C_e) \qquad \text{(Eq. 2.10)}$$

The concentration of the Gadolinium in the EECS can be substituted back into equation 2.8 to express its concentration in the tissue as the sum of the plasma component, or first pass of the contrast agent, and the leakage component.

$$C_e(t) = v_p C_p(t) + K_{trans} \int_0^\tau C_p(\tau) e^{((t-\tau)/v_e)} d\tau \qquad \text{(Eq. 2.11)}$$

A dynamic MRI sequence can be designed to be sensitive to either component. T1-weighted DCE-MRI is commonly acquired with a 3D fast spoiled gradient recalled (SPGR) with short TR and TE, allowing relatively good image resolution, but low temporal resolution (on the order of several seconds). For DCE-MRI the first pass of the agent is generally ignored and the focus is on the calculation of quantitative parameter estimates of Ktrans or permeability-surface area product (Kps).

Figure 2.9: DCE and DSC dynamic data from patient with GBM
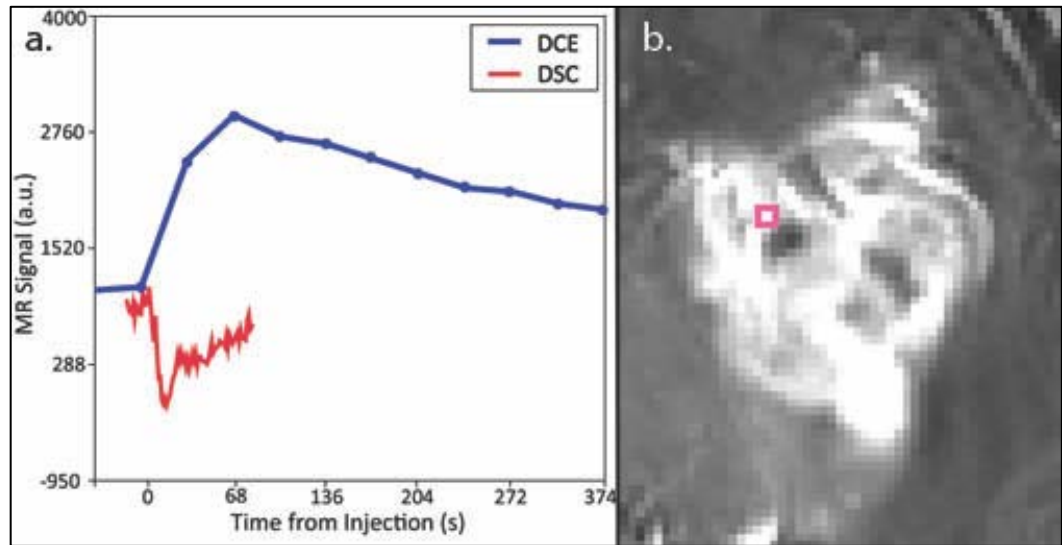
Figure 2.9: (a) Plot of DCE (blue) and DSC (red) dynamic data from a patient with GBM acquired sequentially within the same exam. (b) The pink square shows the region of interest corresponding to the location of the dynamic data overlaid on T1-weighted post-contrast MRI. Time = 0 represents the time of the gadolinium contrast injection (bolus for DSC and infusion for DCE acquisition). Note the greater time resolution of DSC and the longer acquisition time of DCE.

Figure 2.9.a (blue) shows the T1-weighted kinetic enhancement curve following an injection of gadolinium contrast in a patient with GBM. The DCE dynamic data can be separated into three phases: the upslope (**Figure 2.9.a**: time = 0 to 68s), the maximum enhancement (**Figure 2.9.a:** time = 68s), and the washout phase (**Figure 2.9.a:** time = 102 to 374s). The upslope phase reflects overall perfusion to the tissue, so highly vascularized tissue will have a faster upslope. The maximum enhancement phase is reflective of maximum uptake of contrast to the interstitial space. The washout phase is reflective of the leakage of contrast agent dominated by K_{trans}.

31

2.11 Perfusion Imaging: DSC:

DSC-MRI is a dynamic imaging technique that is aimed at capturing the first-pass of the contrast bolus. It utilizes the decrease and subsequent recovery in signal observed on T_2 or T_2^* weighted images as the agent passes through the vasculature. The reduction in signal is due to spin-spin dephasing due to the susceptibility gradient, which is induced by the intravascular compartmentalized gadolinium [49]. The signal intensity over time curve can be converted to a change in T_2^* relaxivity (ΔR_2^*) curve which has a nearly linear relationship with contrast agent concentration [50], thus providing information about the hemodynamics of the tissue. The change in relaxivity is described as:

$$\Delta R_2^*(t) = -\frac{\ln\left(\frac{S(t)}{S_0}\right)}{TE} \qquad \text{(Eq. 2.12)}$$

where $S(t) = T_2$ or T_2^*-weighted signal at time t; S_0 = baseline signal excluding the first few data points (typically 5 points) in order to allow the MR signal to reach steady state; and TE = echo time.

In **Figure 2.9.a**, comparison of the T_2^* MR signal (red) used in DSC and the T_1-weighted MR signal trace (blue) used in DCE, highlights many distinguishing acquisition features. First, the acquisition time is much shorter in DSC (~2 minutes) than DCE (~6-10 minutes), since DSC is aimed at describing the plasma component to calculate a sensitive estimate of blood volume rather than permeability from the leakage component.

32

Second, the time resolution is shorter for DSC (~1.5 s) than for DCE (~7s for bolus injection, ~34s for infusion). This is needed to acquire enough samples to fully describe the hemodynamic curve during the first pass of the bolus and is commonly achieved by using single-shot echo-planar imaging, with the penalty that it results in lower spatial resolution. The critical feature of the echo-planar imaging sequence is that its time resolution can be greatly improved by traversing the entire k-space in one TR, The main disadvantage of using EPI is that there is more time to accumulate phase errors due to susceptibility effects, which can lead to geometric distortion. This warping can be addressed by applying a non-rigid affine transform that uses mutual information in order to register the image to the corresponding anatomic images and hence correct for the distortion [51]. DSC can also be tailored to alter the relative sensitivity of the hemodynamic curve to small microvasculature (using T_2 signal with a spin-echo sequence) or a mixture of small capillaries and large vessels (using T_2^* signal with a gradient-echo sequence) [50, 52-53].

There are multiple methods for deriving functional vascular parameters from the DSC hemodynamic curve. Quantitative approaches are based on identifying an arterial input function (AIF) and deconvolving this with the observed ΔR_2^* to calculate a tissue response function [54-56]. The advantage of these methods are that they yield quantitative estimates of cerebral blood flow (CBF) and cerebral blood volume (CBV), but they are computationally intensive and prone to noise propagation. This limits their clinical utility. Semi-quantitative approaches developed by Weisskoff et al. [57] are built on the assumption that the tissue response function is similar between patients and hence avoids identification of the AIF and deconvolution. Although these methods yield relative

rather than absolute parameter estimates, they are more practical in the clinical setting and have been shown to be useful physiologic markers for predicting tumor grade and response to therapy (see Sec. 2.11).

Regional cerebral blood volume (rCBV) is the most reliable and most common semi-quantitative hemodynamic parameter derived from DSC imaging and is traditionally calculated by integrating the ΔR_2^* curve during the first pass of the contrast agent. However, this model assumes that the gadolinium is confined to the intravascular compartment, which may not be the case in GBM tumors that exhibit breakdown of the BBB.

2.12 Engineering Challenges of using DSC: Extravasation and Developing Methods

For regions where there is breakdown of the BBB, the extravasation of the gadolinium contrast agent causes a change in the T_1 relaxation time which modifies the observed signal intensity and makes the estimation of vascular parameters more complex [58]. This is problematic as extravasation of contrast decreases the susceptibility gradient between the intra- and extravascular components and cause T1-shortening, which results in signal increase and challenges the assumption of there being a linear relationship between the observed ΔR_2^* and concentration of contrast agent (C_{Gd}).

$$\Delta R_2^* \equiv \frac{1}{T_2^*} - \frac{1}{T_{2,baseline}^*} = R_2^* C_{Gd} \text{ and } \Delta R_1 \equiv \frac{1}{T_1} - \frac{1}{T_{1,baseline}} = R_1 C_{Gd} \quad \text{(Eq. 2.13)}$$

Multiple strategies, including both post-processing strategies and tailored acquisition methods, have been proposed to address this situation [59-62]. The method of Weisskoff et al [57] was further elaborated by Donahue et al [63] and has been widely used in the research setting. It is based on modeling the observed ΔR_2^* curve as the sum of the true R_2^* resulting from the bolus and an additional T_1 component caused by leakage:

$$\Delta R_{2,observed}^*(t) = \Delta R_2^*(t) - \frac{TRexp(-TR/T1)}{TE(1-\exp(-TR/T1))} R_1 C_{tissue}(t) \quad \text{(Eq. 2.14)}$$

Back diffusion from the tissue into the plasma is ignored. The time rate of change of C_{tissue} is equal to the average concentration in the vascular component ($\overline{C_{vasc}}(t)$) weighted by a permeability surface constant (PS) between the intra and extravascular space.

$$\frac{dC_{tissue}(t)}{dt} = PS \cdot \overline{C_{vasc}} \quad \text{(Eq. 2.15)}$$

Using a conversion factor (k) between permeability and relaxivity and recalling equation 2.13, this can be expressed as:

$$\frac{dC_{tissue}(t)}{dt} = k \cdot \Delta R_2^* \quad \text{(Eq. 2.16)}$$

C_{tissue} can then be expressed as the average of all the non-contrast enhancing voxels (zero permeability) weighted by a permeability constant (K_2).

$$C_{tissue} = K_2 \int_0^t \overline{\Delta R_2^*(\tau)} \, d\tau \quad \text{(Eq. 2.17)}$$

Substituting equation 2.17 back into equation 2.14, the observed ΔR_2^* can be expressed as a combination of the bolus and leakage components:

$$\Delta R_{2,observed}^*(t) = K_1 \overline{\Delta R_2^*(t)} - K_2 \int_0^t \overline{\Delta R_2^*(\tau)} \, d\tau \quad \text{(Eq. 2.18)}$$

Nonlinear least-squares fitting can then be applied to calculate the constants K1 and

K2[64-65]. The hemodynamic curve can now be expressed as a combination of a gamma-

variate function, corrected for leakage by subtracting the cumulative integral of T1-

dominated component (**Figure 2.10**). The fitted model can be used to calculate the

leakage factor (RF) and leakage-corrected estimates of rCBV.

Figure 2.10: Nonlinear Fit with Leakage-Correction
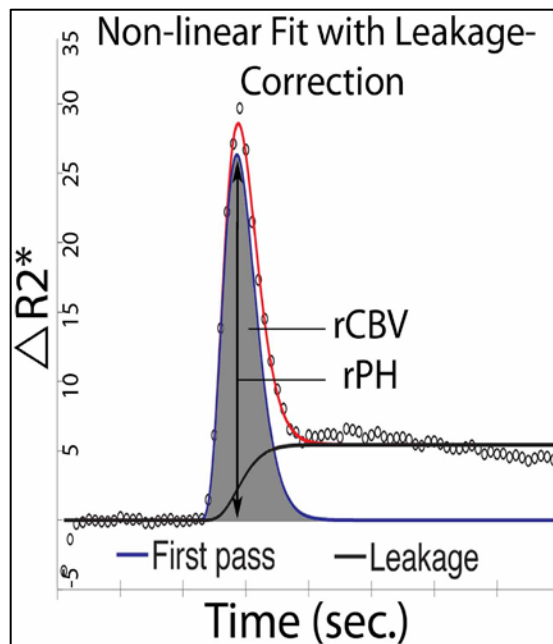
Figure 2.10. ΔR_2^* data from a patient with de novo GBM (circles). Using the two
compartment nonlinear model, the estimated leakage component (black line) is subtracted
from the raw data and a gamma-variate model is fit to the leakage-corrected data (blue).
rCBV is calculated by integrating the leakage-corrected model (shaded area). Peak height
(rPH) is defined as the peak of the first pass model and percent recovery is calculated by
dividing the distance recovered (rPH – steady-state of the leakage component) by the
rPH.

The disadvantage of this post-processing strategy is that it requires complex nonlinear fitting procedure, which is not always practical in the clinic. Many other post-processing methods are also being used in research and clinical settings to estimate perfusion parameters. One simple, non-parametric approach is to calculate parameters such as peak height and percent signal recovery directly from the $\Delta R^*_{2,observed}(t)$ curve without model-fitting [60]. Chapter 3 is aimed at identifying which common post-processing method most accurately reflects the vascular histopathology for de novo GBM when applied to single gradient-echo DSC data acquired with a low-flip angle.

The effects of extravasation can also be modulated through changes in data acquisition parameters that reduce the impact of T1 contamination in the signal obtained. These include the use of a low flip angle gradient echo sequence [65-66], the implementation of a dual-echo sequence [67-69] and the application of an additional, pre-load injection of gadolinium [59, 70-71]. In the majority of the studies described in this dissertation, DSC data were obtained with a 30° - 35° flip angle and a short TE (54 – 56 ms) are able to minimize sensitivity to T1 and maximize the susceptibility change during the first-pass of the contrast agent. Dynamic dual-echo perfusion imaging corrects for the T1 signal contamination by utilizing the ratio of signal intensity acquired from the two echoes at each time point after a single injection. The clinical validation of the resulting perfusion estimates is ongoing [72]. A further acquisition strategy is to apply a small, pre-dose of gadolinium contrast several minutes prior to acquiring the DSC data. This pre-dose reduces the initial T1 of the tissue so that the subsequent changes in signal due to extravasation of contrast agent are reduced. This strategy is relatively straightforward to add to a clinical MRI exam, but requires additional exposure to gadolinium and may provide an increase in risk to the patient of nephrogenic systemic fibrosis (NSF).

Chapter 4 is aimed at identifying the acquisition paradigm that combines flip angle and presence of pre-load injection to yield the most repeatable data in order to ensure a robust estimate of vascular parameters for serial comparisons.

2.13 Clinical Utility of Integrating Physiologic Imaging with Standard MRI for Patients with Brain Tumors

While there are engineering challenges that remain to be addressed in the quantification of physiologic estimates from perfusion and diffusion imaging, these techniques remain promising for improving clinical care. When a patient presents with a suspected brain tumor, one of the first challenges faced by clinicians is how to most accurately diagnosis the disease in order to ensure the patient is placed upon the optimal treatment path. Physiologic MRI may provide complementary information that is useful in differentiating between glioma subtypes. DSC and DWI have been shown to distinguish between low-grade gliomas [73-74], and between metastases and GBM [75-76] better than standard anatomic MRI. Increased rCBV relative to normal appearing white matter (NAWM) in treatment naïve patients has been associated with greater malignancy [77-79]. The addition of DWI and DSC to standard anatomical MRI may therefore also help to guide tissue sample selection to the most malignant regions of the tumor and allow for more accurate diagnosis of disease.

With emerging evidence of bevacizumab resistance and increased invasiveness that have been reported following treatment failure in some patients [80], there is growing interest in prescribing antiangiogenic therapies strategically in the upfront setting to those that patients that will respond best, rather than unilaterally to all patients. Prognostic markers, such as age

and Karrnofsky performance score (KPS), are favorable markers of prolonged survival in patients with GBM, but treatment-specific predictive markers are needed in order to tailor therapies to individual patients. MGMT-promoter methylation status has been found to be a predicative marker of prolonged survival in GBM patients treated with temozolomide and radiotherapy [81], but currently there are no clinically accepted predictive markers for specific antiangiogenic therapies. DSC and DWI may provide useful insights into the tumor physiology that could help tailor subsequent treatment planning. Patients newly diagnosed with GBM with large regions of restricted ADC, abnormal perfusion, and elevated metabolic indices preoperatively [82] and prior to radio- and chemotherapy [83] were found to have worse overall survival. In the upfront antiangiogenic setting, histogram analysis of ADC within the enhancing lesion has shown that lesions with lower ADC, perhaps counterintuitively, respond better to bevacizumab and have prolonged survival compared to patients with high ADC lesions [84]. The authors note that a greater number of patients with low ADC lesions were also MGMT–methylated, which may be related to the survival advantage, or that bevacizumab may be more effective in preventing angiogenesis in tumors with less active VEGF proliferation, presumably the low-ADC lesions. Clearly there is a strong potential for using physiologic imaging parameters to augment treatment stratification.

Physiologic imaging may also aid in providing a biomarker of response once a patient is receiving adjuvant therapy. A recent study reported that patients with recurrent GBM who demonstrated elevated perfusion after adjuvant cediranib treatment had increased overall survival [85]. Multiple studies have shown DWI to provide biomarkers of progression free survival by applying fDM [47, 86] or histogram analysis to the non-enhancing lesion [87-88]. DWI has been reported to be useful in evaluating pseudoprogression when new regions of

contrast enhancement appear immediately post-operatively by differentiating between glyolitic cavity and tumor recurrence [89]. Prolonged and reversible vascular normalization has been observed on DCE and DSC perfusion imaging following antiangiogenic therapy [90], suggesting there may be an optimum treatment-window for antiangiogenic therapies. Expanding upon this work, others have proposed a "vascular normalization index" that combines relative changes in permeability and blood volume from DSC imaging as an early biomarker of response to cerdanib in recurrent GBM patients [91]. With the advent of the RANO recommendations and the growing acknowledgment in the neuro-oncology field that the conventional response criteria have limited effectiveness in the antiangiogenic therapy setting, the use of physiologic imaging to develop alternative biomarkers is becoming even more critical.

Finally, one of the most important challenges facing neuro-oncologists today is the difficulty in differentiating between tumor recurrence and treatment-related tissue changes, such as radiation-induced necrosis, which can both lead to BBB disruption. Physiologic imaging may be particularly useful in better characterizing the large areas of contrast-enhancement often observed at GBM recurrence, which can contain a combination of viable tumor and/or treatment-related injury. DSC data that are co-registered to image-guided tissue sample locations from GBM patients obtained at the time of suspected recurrence have shown elevated rCBV in regions of tumor compared to regions with post-treatment radiation effect [70, 92]. Mixed results have been reported with ADC, which has shown regions of tumor recurrence to have both lower [93] and higher [94] ADC values than regions corresponding to radiation effect. Incorporating physiologic imaging as a complementary noninvasive method

to better distinguish regions of BBB disruption that may or may not contain viable tumor, will

improve clinicians ability to make treatment-altering decisions.

Figure 2.11: Examples of integrating physiologic and anatomic MRI to aid in treatment management of GBM
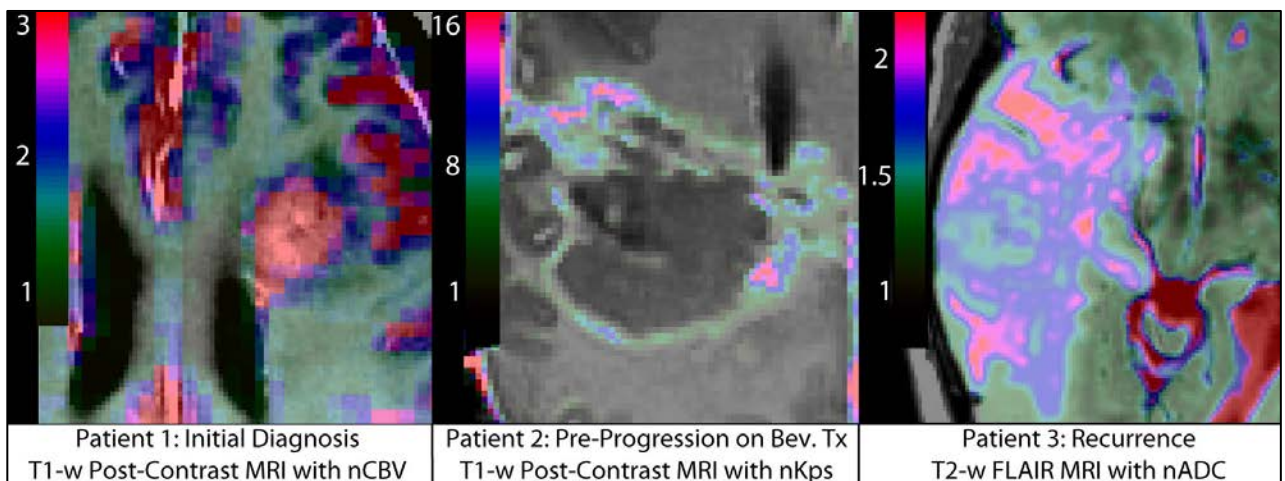
Figure 2.11: Physiologic MRI data overlaid on anatomical MRI of three patients with GBM at different stages of treatment. Patient 1 (left) shows a highly vascularized region throughout the contrast-enhancement at diagnosis prior to beginning treatment. Patient 2 (middle) shows sub-regions of the contrast-enhancing lesion with highly elevated Kps immediately prior to progression on adjuvant bevacizumab treatment. Patient 3 (right) shows a mix of ADC values likely corresponding to components of edema and infiltrative tumor throughout the T2-lesion at recurrence. Determining how to best integrate physiologic MRI data to guide treatment strategy, provide biomarkers of response, and characterize recurrence remain open research questions.

The integration of physiologic imaging methods to the clinical MRI exam for patients with GBM has the potential to improve the diagnosis of disease, tailor adjuvant treatment strategies to an individual patient, provide an alternative early biomarker of response, and better distinguish recurrence from the effect of treatment. **Figure 2.11** illustrates three patient examples showing how physiologic data can be incorporated with standard anatomical MRI. The potential benefit of these complementary imaging parameters rests on developing reliable methods and analysis metrics that can be translated to the clinical environment. The research presented in this dissertation was aimed at addressing the engineering challenges and clinical translation of incorporating physiologic perfusion and diffusion MR-imaging to the treatment management of patients with GBM.

2.14 References:

1. Porter, K.R., et al., *Prevalence estimates for primary brain tumors in the United States by age, gender, behavior, and histology.* Neuro Oncol, 2010. **12**(6): p. 520-7.
2. CBTRUS, *2009-2010 CBTRUS Statistical Report: Primary Brain and Central Nervous System Tumors Diagnosed in Eighteen States in 2002-2006*, 2009, Published by the Central Brain Tumor Registry of the United States, Hinsdale, IL. 60521.
3. Kohler, B.A., et al., *Annual report to the nation on the status of cancer, 1975-2007, featuring tumors of the brain and other nervous system.* J Natl Cancer Inst, 2011. **103**(9): p. 714-36.
4. Jemal, A., et al., *Cancer statistics, 2010.* CA Cancer J Clin, 2010. **60**(5): p. 277-300.
5. Society, A.C., *Detailed Guide: Brain / CNS Tumors in Adults*, 2009.
6. Louis, D.N., et al., *The 2007 WHO classification of tumours of the central nervous system.* Acta Neuropathol, 2007. **114**(2): p. 97-109.
7. CBTRUS, *Central Brain Tumor Registry of the United States analysis of the NPCR and SEER data, 2004 - 2007.* 2011.
8. Stupp, R., et al., *Effects of radiotherapy with concomitant and adjuvant temozolomide versus radiotherapy alone on survival in glioblastoma in a randomised phase III study: 5-year analysis of the EORTC-NCIC trial.* Lancet Oncol, 2009. **10**(5): p. 459-66.
9. Friedman, H.S., et al., *Irinotecan therapy in adults with recurrent or progressive malignant glioma.* J Clin Oncol, 1999. **17**(5): p. 1516-25.
10. Bergers, G. and L.E. Benjamin, *Tumorigenesis and the angiogenic switch.* Nat Rev Cancer, 2003. **3**(6): p. 401-10.
11. Hanahan, D. and J. Folkman, *Patterns and emerging mechanisms of the angiogenic switch during tumorigenesis.* Cell, 1996. **86**(3): p. 353-64.
12. Kerbel, R.S., *Tumor angiogenesis.* N Engl J Med, 2008. **358**(19): p. 2039-49.
13. Chi, A.S., et al., *Angiogenesis as a therapeutic target in malignant gliomas.* Oncologist, 2009. **14**(6): p. 621-36.
14. Stupp, R., et al., *Radiotherapy plus concomitant and adjuvant temozolomide for glioblastoma.* N Engl J Med, 2005. **352**(10): p. 987-96.
15. Chi, A.S., A.D. Norden, and P.Y. Wen, *Antiangiogenic strategies for treatment of malignant gliomas.* Neurotherapeutics, 2009. **6**(3): p. 513-26.
16. Kerbel, R. and J. Folkman, *Clinical translation of angiogenesis inhibitors.* Nat Rev Cancer, 2002. **2**(10): p. 727-39.
17. Quick, A., et al., *Current therapeutic paradigms in glioblastoma.* Rev Recent Clin Trials, 2010. **5**(1): p. 14-27.
18. Wen, P.Y. and S. Kesari, *Malignant gliomas in adults.* N Engl J Med, 2008. **359**(5): p. 492-507.
19. Teicher, B.A., et al., *Enzymatic rationale and preclinical support for a potent protein kinase C beta inhibitor in cancer therapy.* Adv Enzyme Regul, 1999. **39**: p. 313-27.

20. Graff, J.R., et al., *The protein kinase Cbeta-selective inhibitor, Enzastaurin (LY317615.HCl), suppresses signaling through the AKT pathway, induces apoptosis, and suppresses growth of human colon cancer and glioblastoma xenografts.* Cancer Res, 2005. **65**(16): p. 7462-9.

21. Butowski, N., et al., *Phase II and pharmacogenomics study of enzastaurin plus temozolomide during and following radiation therapy in patients with newly diagnosed glioblastoma multiforme and gliosarcoma.* Neuro Oncol, 2011. **13**(12): p. 1331-8.

22. Wick, W., et al., *Phase III study of enzastaurin compared with lomustine in the treatment of recurrent intracranial glioblastoma.* J Clin Oncol, 2010. **28**(7): p. 1168-74.

23. Fischer, I., et al., *High-grade glioma before and after treatment with radiation and Avastin: initial observations.* Neuro Oncol, 2008. **10**(5): p. 700-8.

24. Iwamoto, F.M., et al., *Patterns of relapse and prognosis after bevacizumab failure in recurrent glioblastoma.* Neurology, 2009. **73**(15): p. 1200-6.

25. Norden, A.D., et al., *Bevacizumab for recurrent malignant gliomas: efficacy, toxicity, and patterns of recurrence.* Neurology, 2008. **70**(10): p. 779-87.

26. Jain, R.K., *Normalization of tumor vasculature: an emerging concept in antiangiogenic therapy.* Science, 2005. **307**(5706): p. 58-62.

27. Friedman, H.S., et al., *Bevacizumab alone and in combination with irinotecan in recurrent glioblastoma.* J Clin Oncol, 2009. **27**(28): p. 4733-40.

28. Kreisl, T.N., et al., *Phase II trial of single-agent bevacizumab followed by bevacizumab plus irinotecan at tumor progression in recurrent glioblastoma.* J Clin Oncol, 2009. **27**(5): p. 740-5.

29. Stanisz, G.J., et al., *T1, T2 relaxation and magnetization transfer in tissue at 3T.* Magn Reson Med, 2005. **54**(3): p. 507-12.

30. Macdonald, D.R., et al., *Response criteria for phase II studies of supratentorial malignant glioma.* J Clin Oncol, 1990. **8**(7): p. 1277-80.

31. Wong, E.T., et al., *Outcomes and prognostic factors in recurrent glioma patients enrolled onto phase II clinical trials.* J Clin Oncol, 1999. **17**(8): p. 2572-8.

32. Desjardins, A., et al., *Bevacizumab and daily temozolomide for recurrent glioblastoma.* Cancer, 2012. **118**(5): p. 1302-12.

33. Vredenburgh, J.J., et al., *Addition of bevacizumab to standard radiation therapy and daily temozolomide is associated with minimal toxicity in newly diagnosed glioblastoma multiforme.* Int J Radiat Oncol Biol Phys, 2012. **82**(1): p. 58-66.

34. Narayana, A., et al., *A clinical trial of bevacizumab, temozolomide, and radiation for newly diagnosed glioblastoma.* J Neurosurg, 2012. **116**(2): p. 341-5.

35. Reardon, D.A., et al., *Phase II study of carboplatin, irinotecan, and bevacizumab for bevacizumab naive, recurrent glioblastoma.* J Neurooncol, 2012. **107**(1): p. 155-64.

36. Henriksson, R., T. Asklund, and H.S. Poulsen, *Impact of therapy on quality of life, neurocognitive function and their correlates in glioblastoma multiforme: a review.* J Neurooncol, 2011. **104**(3): p. 639-46.

37. Ellingson, B.M., et al., *Quantification of edema reduction using differential quantitative T2 (DQT2) relaxometry mapping in recurrent glioblastoma treated with bevacizumab.* J Neurooncol, 2012. **106**(1): p. 111-9.

38.   Verhoeff, J.J., et al., *Concerns about anti-angiogenic treatment in patients with glioblastoma multiforme.* BMC Cancer, 2009. **9**: p. 444.

39.   Vredenburgh, J.J., et al., *Corticosteroid use in patients with glioblastoma at first or second relapse treated with bevacizumab in the BRAIN study.* Oncologist, 2010. **15**(12): p. 1329-34.

40.   Wen, P.Y., et al., *Updated response assessment criteria for high-grade gliomas: response assessment in neuro-oncology working group.* J Clin Oncol, 2010. **28**(11): p. 1963-72.

41.   Nelson, S.J., *Multivoxel magnetic resonance spectroscopy of brain tumors.* Mol Cancer Ther, 2003. **2**(5): p. 497-507.

42.   Nelson, S.J., et al., *In vivo molecular imaging for planning radiation therapy of gliomas: an application of 1H MRSI.* J Magn Reson Imaging, 2002. **16**(4): p. 464-76.

43.   Cha, S., *Neuroimaging in neuro-oncology.* Neurotherapeutics, 2009. **6**(3): p. 465-77.

44.   Chang, S.M., et al., *Integration of preoperative anatomic and metabolic physiologic imaging of newly diagnosed glioma.* J Neurooncol, 2009. **92**(3): p. 401-15.

45.   Moffat, B.A., et al., *The functional diffusion map: an imaging biomarker for the early prediction of cancer treatment outcome.* Neoplasia, 2006. **8**(4): p. 259-67.

46.   Hamstra, D.A., et al., *Evaluation of the functional diffusion map as an early biomarker of time-to-progression and overall survival in high-grade glioma.* Proc Natl Acad Sci U S A, 2005. **102**(46): p. 16759-64.

47.   Ellingson, B.M., et al., *Volumetric analysis of functional diffusion maps is a predictive imaging biomarker for cytotoxic and anti-angiogenic treatments in malignant gliomas.* J Neurooncol, 2011. **102**(1): p. 95-103.

48.   Tofts, P.S. and A.G. Kermode, *Measurement of the blood-brain barrier permeability and leakage space using dynamic MR imaging. 1. Fundamental concepts.* Magn Reson Med, 1991. **17**(2): p. 357-67.

49.   Rosen, B.R., et al., *Perfusion imaging with NMR contrast agents.* Magn Reson Med, 1990. **14**(2): p. 249-65.

50.   Weisskoff, R.M., et al., *Microscopic susceptibility variation and transverse relaxation: theory and experiment.* Magn Reson Med, 1994. **31**(6): p. 601-10.

51.   Rueckert, D., et al., *Nonrigid registration using free-form deformations: application to breast MR images.* IEEE Trans Med Imaging, 1999. **18**(8): p. 712-21.

52.   Fisel, C.R., et al., *MR contrast due to microscopically heterogeneous magnetic susceptibility: numerical simulations and applications to cerebral physiology.* Magn Reson Med, 1991. **17**(2): p. 336-47.

53.   Schmainda, K.M., et al., *Characterization of a first-pass gradient-echo spin-echo method to predict brain tumor grade and angiogenesis.* AJNR Am J Neuroradiol, 2004. **25**(9): p. 1524-32.

54.   Calamante, F., *Perfusion MRI using dynamic-susceptibility contrast MRI: quantification issues in patient studies.* Top Magn Reson Imaging, 2010. **21**(2): p. 75-85.

55. Calamante, F., et al., *Measuring cerebral blood flow using magnetic resonance imaging techniques.* J Cereb Blood Flow Metab, 1999. **19**(7): p. 701-35.

56. Ostergaard, L., et al., *High resolution measurement of cerebral blood flow using intravascular tracer bolus passages. Part I: Mathematical approach and statistical analysis.* Magn Reson Med, 1996. **36**(5): p. 715-25.

57. Weisskoff, R.M., Boxerman J. L., Sorensen A. G., Kulke S. M., Campbell T. A., Rosen B. R., *Simultaneous blood volume and permeability mapping using a single Gd-based contrast injection.* In: Proceedings of the Second Meeting of the Society of Magnetic Resonance., 1994. **Berkeley, CA**(279).

58. Weisskoff, R.M., *Simultaneous blood volume and permeability mapping using a single GD-based contrast injection.* In: Proceedings of the 2nd Annual Meeting of ISMRM, 1994. **San Francisco**: p. 279.

59. Paulson, E.S. and K.M. Schmainda, *Comparison of dynamic susceptibility-weighted contrast-enhanced MR methods: recommendations for measuring relative cerebral blood volume in brain tumors.* Radiology, 2008. **249**(2): p. 601-13.

60. Lupo, J.M., et al., *Dynamic susceptibility-weighted perfusion imaging of high-grade gliomas: characterization of spatial heterogeneity.* AJNR Am J Neuroradiol, 2005. **26**(6): p. 1446-54.

61. Cha, S., et al., *Dynamic susceptibility contrast MR imaging: correlation of signal intensity changes with cerebral blood volume measurements.* J Magn Reson Imaging, 2000. **11**(2): p. 114-9.

62. Barajas, R.F., Jr., et al., *Glioblastoma multiforme regional genetic and cellular expression patterns: influence on anatomic and physiologic MR imaging.* Radiology, 2010. **254**(2): p. 564-76.

63. Donahue, K.M., et al., *Utility of simultaneously acquired gradient-echo and spin-echo cerebral blood volume and morphology maps in brain tumor patients.* Magn Reson Med, 2000. **43**(6): p. 845-53.

64. Henry, R.G., et al., *Comparison of relative cerebral blood volume and proton spectroscopy in patients with treated gliomas.* AJNR Am J Neuroradiol, 2000. **21**(2): p. 357-66.

65. Lee, M.C., et al., *Dynamic susceptibility contrast perfusion imaging of radiation effects in normal-appearing brain tissue: changes in the first-pass and recirculation phases.* J Magn Reson Imaging, 2005. **21**(6): p. 683-93.

66. Law, M., et al., *Conventional MR imaging with simultaneous measurements of cerebral blood volume and vascular permeability in ganglioglioma.* Magn Reson Imaging, 2004. **22**(5): p. 599-606.

67. Heiland, S., et al., *Simultaneous assessment of cerebral hemodynamics and contrast agent uptake in lesions with disrupted blood-brain-barrier.* Magn Reson Imaging, 1999. **17**(1): p. 21-7.

68. Vonken, E.P., et al., *Simultaneous quantitative cerebral perfusion and Gd-DTPA extravasation measurement with dual-echo dynamic susceptibility contrast MRI.* Magn Reson Med, 2000. **43**(6): p. 820-7.

69. Uematsu, H., et al., *Blood volume of gliomas determined by double-echo dynamic perfusion-weighted MR imaging: a preliminary study.* AJNR Am J Neuroradiol, 2001. **22**(10): p. 1915-9.

70. Hu, L.S., et al., *Relative cerebral blood volume values to differentiate high-grade glioma recurrence from posttreatment radiation effect: direct correlation between image-guided tissue histopathology and localized dynamic susceptibility-weighted contrast-enhanced perfusion MR imaging measurements.* AJNR Am J Neuroradiol, 2009. **30**(3): p. 552-8.

71. Hu, L.S., et al., *Optimized preload leakage-correction methods to improve the diagnostic accuracy of dynamic susceptibility-weighted contrast-enhanced perfusion MR imaging in posttreatment gliomas.* AJNR Am J Neuroradiol, 2010. **31**(1): p. 40-8.

72. Uematsu, H. and M. Maeda, *Double-echo perfusion-weighted MR imaging: basic concepts and application in brain tumors for the assessment of tumor blood volume and vascular permeability.* Eur Radiol, 2006. **16**(1): p. 180-6.

73. Cha, S., et al., *Differentiation of low-grade oligodendrogliomas from low-grade astrocytomas by using quantitative blood-volume measurements derived from dynamic susceptibility contrast-enhanced MR imaging.* AJNR Am J Neuroradiol, 2005. **26**(2): p. 266-73.

74. Khayal, I.S. and S.J. Nelson, *Characterization of low-grade gliomas using RGB color maps derived from ADC histograms.* J Magn Reson Imaging, 2009. **30**(1): p. 209-13.

75. Cha, S., et al., *Differentiation of glioblastoma multiforme and single brain metastasis by peak height and percentage of signal intensity recovery derived from dynamic susceptibility-weighted contrast-enhanced perfusion MR imaging.* AJNR Am J Neuroradiol, 2007. **28**(6): p. 1078-84.

76. Server, A., et al., *Diagnostic examination performance by using microvascular leakage, cerebral blood volume, and blood flow derived from 3-T dynamic susceptibility-weighted contrast-enhanced perfusion MR imaging in the differentiation of glioblastoma multiforme and brain metastasis.* Neuroradiology, 2011. **53**(5): p. 319-30.

77. Law, M., et al., *Comparison of cerebral blood volume and vascular permeability from dynamic susceptibility contrast-enhanced perfusion MR imaging with glioma grade.* AJNR Am J Neuroradiol, 2004. **25**(5): p. 746-55.

78. Law, M., et al., *Glioma grading: sensitivity, specificity, and predictive values of perfusion MR imaging and proton MR spectroscopic imaging compared with conventional MR imaging.* AJNR Am J Neuroradiol, 2003. **24**(10): p. 1989-98.

79. Knopp, E.A., et al., *Glial neoplasms: dynamic contrast-enhanced T2*-weighted MR imaging.* Radiology, 1999. **211**(3): p. 791-8.

80. Quant, E.C., et al., *Role of a second chemotherapy in recurrent malignant glioma patients who progress on bevacizumab.* Neuro Oncol, 2009. **11**(5): p. 550-5.

81. Hegi, M.E., et al., *MGMT gene silencing and benefit from temozolomide in glioblastoma.* N Engl J Med, 2005. **352**(10): p. 997-1003.

82. Crawford, F.W., et al., *Relationship of pre-surgery metabolic and physiological MR imaging parameters to survival for patients with untreated GBM.* J Neurooncol, 2009. **91**(3): p. 337-51.

83. Saraswathy, S., et al., *Evaluation of MR markers that predict survival in patients with newly diagnosed GBM prior to adjuvant therapy.* J Neurooncol, 2009. **91**(1): p. 69-81.

84.   Pope, W.B., et al., *Apparent diffusion coefficient histogram analysis stratifies progression-free survival in newly diagnosed bevacizumab-treated glioblastoma.* AJNR Am J Neuroradiol, 2011. **32**(5): p. 882-9.

85.   Sorensen, A.G., et al., *Increased Survival of Glioblastoma Patients Who Respond to Antiangiogenic Therapy with Elevated Blood Perfusion.* Cancer Res, 2012. **72**(2): p. 402-407.

86.   Ellingson, B.M., et al., *Functional diffusion maps (fDMs) evaluated before and after radiochemotherapy predict progression-free and overall survival in newly diagnosed glioblastoma.* Neuro Oncol, 2012. **14**(3): p. 333-43.

87.   Pope, W.B., et al., *Recurrent glioblastoma multiforme: ADC histogram analysis predicts response to bevacizumab treatment.* Radiology, 2009. **252**(1): p. 182-9.

88.   Nowosielski, M., et al., *ADC histograms predict response to anti-angiogenic therapy in patients with recurrent high-grade glioma.* Neuroradiology, 2011. **53**(4): p. 291-302.

89.   Smith, J.S., et al., *Serial diffusion-weighted magnetic resonance imaging in cases of glioma: distinguishing tumor recurrence from postresection injury.* J Neurosurg, 2005. **103**(3): p. 428-38.

90.   Batchelor, T.T., et al., *AZD2171, a pan-VEGF receptor tyrosine kinase inhibitor, normalizes tumor vasculature and alleviates edema in glioblastoma patients.* Cancer Cell, 2007. **11**(1): p. 83-95.

91.   Emblem, K.E., et al., *T(1)- and T(2)(*)-dominant extravasation correction in DSC-MRI: part II-predicting patient outcome after a single dose of cediranib in recurrent glioblastoma patients.* J Cereb Blood Flow Metab, 2011. **31**(10): p. 2054-64.

92.   Barajas, R.F., Jr., et al., *Differentiation of recurrent glioblastoma multiforme from radiation necrosis after external beam radiation therapy with dynamic susceptibility-weighted contrast-enhanced perfusion MR imaging.* Radiology, 2009. **253**(2): p. 486-96.

93.   Hein, P.A., et al., *Diffusion-weighted imaging in the follow-up of treated high-grade gliomas: tumor recurrence versus radiation injury.* AJNR Am J Neuroradiol, 2004. **25**(2): p. 201-9.

94.   Sundgren, P.C., et al., *Differentiation of recurrent brain tumor versus radiation injury using diffusion tensor imaging in patients with new contrast-enhancing lesions.* Magn Reson Imaging, 2006. **24**(9): p. 1131-42.

CHAPTER 3 : Comparison of DSC-MRI Post-Processing Techniques in Predicting Microvascular Histopathology in Patients Newly Diagnosed with GBM

In this project, non-invasive DSC imaging data were directly compared to Factor VIII immunohistochemical staining analysis of microvasculature in tissue samples from patients with treatment-naïve GBM. We calculated DSC perfusion parameters using each of the most common post-processing methods and determined which method best reflects underlying vascular histopathology.

Authors:

Essock-Burns E, Phillips JJ, Molinaro AM, Lupo JM, Cha S, Chang S, Nelson SJ.

3.1 Abstract:

Purpose: To evaluate which common post-processing method applied to gradient-echo DSC-MRI data, acquired with a single gadolinium injection and low flip-angle, most accurately reflects microvascular histopathology for patients with de novo, treatment-naive GBM.

Materials and Methods: 72 tissue samples were collected from 35 patients with treatment-naïve GBM. Sample locations were co-registered to preoperative gradient-echo DSC-MRI acquired with 35° flip-angle and 0.1mmol/kg gadolinium. Estimates of blood volume and leakiness at each sample location were calculated using four common post-processing methods (leakage-corrected nonlinear gamma-variate, non-parametric, scaled MR-signal, and unscaled MR-signal). Tissue sample microvascular morphology was characterized using Factor VIII immunohistochemical analysis. A random-effects regression model, adjusted for repeated measures and contrast-enhancement, identified whether MR parameter estimates significantly predicted IHC findings.

Results: Elevated blood volume estimates from nonlinear and non-parametric methods significantly predicted increased microvascular hyperplasia. Abnormal microvasculature existed beyond the CE-lesion and was significantly reflected by increased blood volume from nonlinear, non-parametric, and scaled MR-signal analysis.

Conclusion: This study provides histopathological support for both non-parametric and nonlinear post-processing of low flip-angle DSC-MRI for characterizing microvascular hyperplasia within GBM. Non-parametric analysis with a single gadolinium injection

may be a particularly useful strategy clinically, as it requires less computational expense and limits gadolinium exposure.

3.2 Introduction:

Dynamic susceptibility-weighted contrast-enhanced (DSC) MR imaging is used for patients with brain tumors to noninvasively assess the tumor angiogenesis and underlying microvascular environment in the lesion and surrounding tissue. DSC MR imaging has become increasingly important in the management of patients with glioma as the therapy paradigm shifts to incorporate anti-angiogenic therapy. One of the challenges of assessing response in this context is that anti-angiogenic agents directly remove what has been considered the primary surrogate outcome measure for assessing treatment response, namely the presence of a contrast-enhancing lesion after the injection of a gadolinium based MR contrast agent (1,2). It is for this reason that DSC imaging has received increasing attention as a more quantitative method for evaluating microvascular changes associated with the tumor (3-5).

Gliomas are the most common malignant primary brain tumor in adults and are highly infiltrative in nature. Accurate diagnosis and definition of tumor grade is based upon histopathologic evaluation of tissue samples obtained by stereotactic biopsy or surgical resection using WHO criteria (6) . Glioblastoma multiforme (GBM) is the most malignant and the highest grade glioma (Grade IV) and is characterized by increased cellular proliferation, nuclear atypia, necrosis, and microvascular proliferation. Microvascular hallmarks of GBM include the presence of complex microvascular

hyperplasia, epitomized by "glomeruloid" bodies, tortuous lamina, and breakdown of the blood brain barrier (BBB) (7). Histopathologic and immunohistochemical (IHC) analysis of the biopsy sample can be used to highlight the microvasculature and is the gold-standard for determining malignancy.

Noninvasive DSC imaging assesses vascular function by tracking the relaxation effects of injected gadolinium-based MR contrast agent as it circulates through the brain. Following the injection of a bolus of gadolinium, the observed T2 or T2*-weighted signal decreases and then recovers as the agent recirculates. The reduction in signal is due to spin-spin dephasing caused by the susceptibility gradient induced by the intravascular compartmentalized gadolinium (8). The changes in signal intensity can be modeled as a change in T2* relaxivity (ΔR_2^*), which has a nearly linear relationship with contrast agent concentration and provides information about the hemodynamics of the tissue. A number of different parameters are computed from the concentration-time curve to create various parametric maps that reflect different characteristics of the underlying microvasculature in the tumor region. The most common parameter used to describe the changes in signal intensity is the relative cerebral blood volume (rCBV), which represents bulk vessel density often expressed as a ratio value to contralateral normal appearing white matter.

For regions where there is breakdown of the BBB, the extravasation of the contrast agent causes a change in the T1 relaxation time which modifies the observed signal intensity and makes the estimation of vascular parameters more complex (9). Multiple strategies have been proposed to address this situation (10-13). Acquisition methods to reduce the impact of the T1 effect include the use of a low flip angle (35°) gradient echo sequence (14,15), the implementation of a dual-echo sequence (16-18) and

the application of an additional, pre-load injection of gadolinium (10,19,20). A post-processing strategy that has been widely used in a research setting, is to model the ΔR_2^* curve as the sum of a gamma-variate function that results from the bolus and an additional component caused by leakage. This requires a more complex nonlinear fitting procedure to estimate model parameters such as rCBV and leakage factor (RF), but the resulting values been shown to correlate well with glioma grade (21).

In cases where a low flip angle is used for data acquisition, a simpler, non-parametric approach to characterizing the ΔR_2^* curve is the determination of the relative peak height (rPH) and percent signal recovery to baseline (PSR). Differences in rPH were shown to differentiate GBM from brain metastasis and the magnitude of PSR early in therapy was shown to be associated with progression-free survival (22,23). In a clinical setting, estimates of rCBV have also been calculated directly from the MR signal trace, either scaled to initial baseline levels (13) or unscaled raw MR data (12). These parameters require minimal computational time for post-processing the data, which makes them a common choice for use in the clinic, but there is limited evidence to support their relationship to physiologic variables (12).

The goal of this study was to apply the most common post-processing methods to DSC imaging data that were acquired with a single dose of gadolinium and a low flip angle using gradient-echo sequence in order to determine which method most accurately reflects the underlying vascular pathology for patients with de novo, treatment-naive GBM. This was achieved by acquiring DSC data from patients prior to surgical resection and making a direct comparison between MR parameter estimates from the locations

where image guided tissue samples were obtained and the results from subsequent histopathological analysis of individual specimens.

3.2 Materials and Methods:

Patient Population:

Thirty-five patients with de novo (primary), treatment-naïve, pathologically confirmed GBM were included in this HIPPA compliant, imaging study. All patients received MRI exams, including anatomic and physiologic imaging, prior to undergoing tumor resection. Preoperative MR data were used to guide the site of tissue sample towards regions with elevated nCBV, low apparent diffusion coefficient (ADC), or high Choline-to-NAA index. Image-guided tissue samples were collected from these tumor locations and the MR imaging coordinates of the sample location were recorded using Brainlab software (Vector Vision Navigation System, Medtronic, Stealth Station). Once removed, the 5mm-diameter spherical samples (approximately 50 mg) were divided into two sections; half was snap-frozen and stored for ex vivo analysis(24) and half was fixed in 10% buffered formalin for histologic and immunohistologic evaluation. The tissue specimen handling methods have been described elsewhere (13, Chapter 7).

MRI Protocol:

MR imaging exams were performed on a 3T GE scanner and included both anatomic and physiologic imaging. In selected cases lactate edited ^{1}H MRSI data were also collected using methods described previously (25,26) and used as an adjunct to the other measurements to select regions of putative tumor for targeting tissue collection. The standard anatomic imaging protocol included axial T2 weighted FLAIR sequence (TE=

120 ms, TR = 10,000 ms, TI = 2200 ms, slice thickness = 3mm, slice gap = 0 mm, matrix

= 192x256, FOV = 24x24 cm) and pre- and post-contrast axial T1-weighted 3D IRSPGR

(TE=2.5 ms, TR = 8.9 ms, TI = 400 ms, slice thickness = 1.5mm, matrix = 256x256,

FOV = 24x24 cm^2 with SENSE R=2). The standard physiologic imaging included

diffusion-weighted imaging (DWI) and DSC perfusion imaging. DWI was acquired with

a 2D spin-echo, echo-planar sequence (TE = 99 ms, TR = 10,000 ms, slice thickness =

3mm, matrix = 256x256, FOV = 24x24 cm^2, 6 gradient directions, b=0 and 1000 s/mm^2).

Gradient-echo, echo-planar DSC imaging was acquired before, during, and following an

injection of 0.1 mmol/kg gadolinium contrast agent (TE = 54 – 56 ms, TR = 1250 – 1500

ms, flip angle = 35°, slice thickness = 3-4 mm, matrix = 128 x 128, FOV = 24 x 24 cm^2)

at 3 ml/s. Fifteen seconds of dynamic imaging was acquired prior to the contrast agent

injection. The first five data points acquired were excluded and the following 10 data

points were used to get an estimate of baseline. Total DSC imaging time was 100 – 120

seconds. A flip-angle of 35º was chosen for all DSC acquisitions in this study in order to

minimize T1 sensitivity during the first-pass of the contrast agent. A TE of 54-56 ms was

selected to maximize the susceptibility change during the first-pass of contrast agent.

These parameters have consistently achieved maximum contrast between normal

appearing white matter and tumor during the recirculation phase of contrast at our

institution.

DSC Image-Processing:
        The DSC data were non-rigidly aligned to the pre-contrast, T1-weighted images

using B-spline warping by maximization of normalized mutual information in order to

minimize distortion from the echo-planar imaging (27,28). A 5-mm diameter spherical

region of interest (ROI) was placed at the corresponding surgical coordinates of the

image-guided target location on the co-registered MRI images (BrainLab, VectorVision Navigation System; Medtronic, Stealth Station). The region of normal-appearing white matter (NAWM) was defined semi-automatically on the pre-contrast T1-weighted image (26). These ROI's were then re-sampled to the native resolution of the DSC data set and overlaid on the DSC data at the original resolution. Average hemodynamic curves were calculated within each specimen region and NAWM using each of the 4 post-processing methods selected for comparison in this study. Any voxel with a signal peak of less than 4 times the baseline noise level was excluded to insure that necrosis voxels would not be included in the representative biopsy average curve. The four post-processing methods included: i) Nonlinear Fit Model of concentration-time curve (nl), (ii) Non-parametric concentration-time curve analysis (np), (iii) Scaled MR signal-time curve analysis (sc), and (iv) Unscaled MR signal-time curve analysis (unsc). Strategies (i) and (ii) are both commonly accepted in the research community (8,9,21,29), while strategies (iii) and (iv) are often used in the clinical setting (12,13). **Table 3.1** describes the hemodynamic curve data, model, and derived parameters for each of these four methods and **Figure 3.1** illustrates examples of the derived perfusion parameters.

Table 3.1: Four post-processing methods and derived perfusion parameters

		Post-Processing Methods & Derived Perfusion Parameters			
		Nonlinear	Non-parametric	Scaled MR signal	UnScaled MR signal
Step 1. Manipulation of the hemodynamic data		$\Delta R2^*$-time curve (Eq. 1)		MR signal-time curve	
Step 2. Calculation of derived perfusion parameters	**Blood Volume Measures**	nCBV, nPH	nPH	nCBV, nMSD	nCBV, nMSD
	Leakiness Measures	PSR	PSR	PSR	PSR

These post-processing methods are described in two steps: (1) manipulation of the hemodynamic data curve and (2) calculation of derived parameters.

<u>Step 1.</u> Manipulation of the Hemodynamic Data Curve:

Average DSC data were either (A) converted to change in relaxivity (ΔR_2^*) representative of the concentration-time curve using Equation 1 or (B) left as MR signal-time curve.

$$\Delta R_2^* = -\frac{\ln(S_1(t) - S_0)}{TE} \quad \text{(Equation 1)}$$

<u>Step 2.</u> Calculation of Derived Perfusion Parameters:

Perfusion parameters that were derived included estimates of blood volume (rCBV, peak height (PH), negative enhancement integral (NEI), or maximum signal drop (MSD)) and estimates of vessel leakiness (percent signal recovery (PSR)) depending on the post-processing method. The average hemodynamic curve from within NAWM was used as a normalization reference to compute relative blood volume measures (nCBV, nPH, nNEI, nMSD, **Figure 3.1**).

A. ΔR_2^* Signal

    (i)   *Nonlinear Fit Model (nl):* The concentration-time curve was fit with a nonlinear gamma-variate model with leakage correction (9). nCBV(nl), nPH(nl), and PSR(nl) were calculated from the model of the first pass (**Figure 3.1.i: Nonlinear Fit Model**).

(ii) *Non-parametric Analysis (np):* The concentration-time curve was used to directly calculate nPH(np) and PSR(np), without fitting a parametric model (**Figure 3.1.ii: Non-Parametric**).

B. MR Signal

(iii) *Scaled MR Signal Analysis (sc)*: The T_2^* MR signal intensity-time curve was scaled to baseline MR signal intensity (mean of the 5th through 10th time-points) and baseline was shifted to 1000 MR arbitrary units. nMSD(sc), nNEI(sc), and PSR(sc) were calculated from this scaled MR signal-time curve (**Figure 3.1.iii: Scaled MR Signal**)

(iv) *Unscaled MR Signal Analysis (unsc):* The raw T_2^* MR signal intensity-time curve was used to directly calculate nMSD(unsc), nNEI(unsc), and PSR(unsc) (**Figure 3.1.iv: Unscaled MR Signal**)

Figure 3.1: The four post-processing methods applied to hemodynamic curve from a single CE-tissue sample with complex vasculature
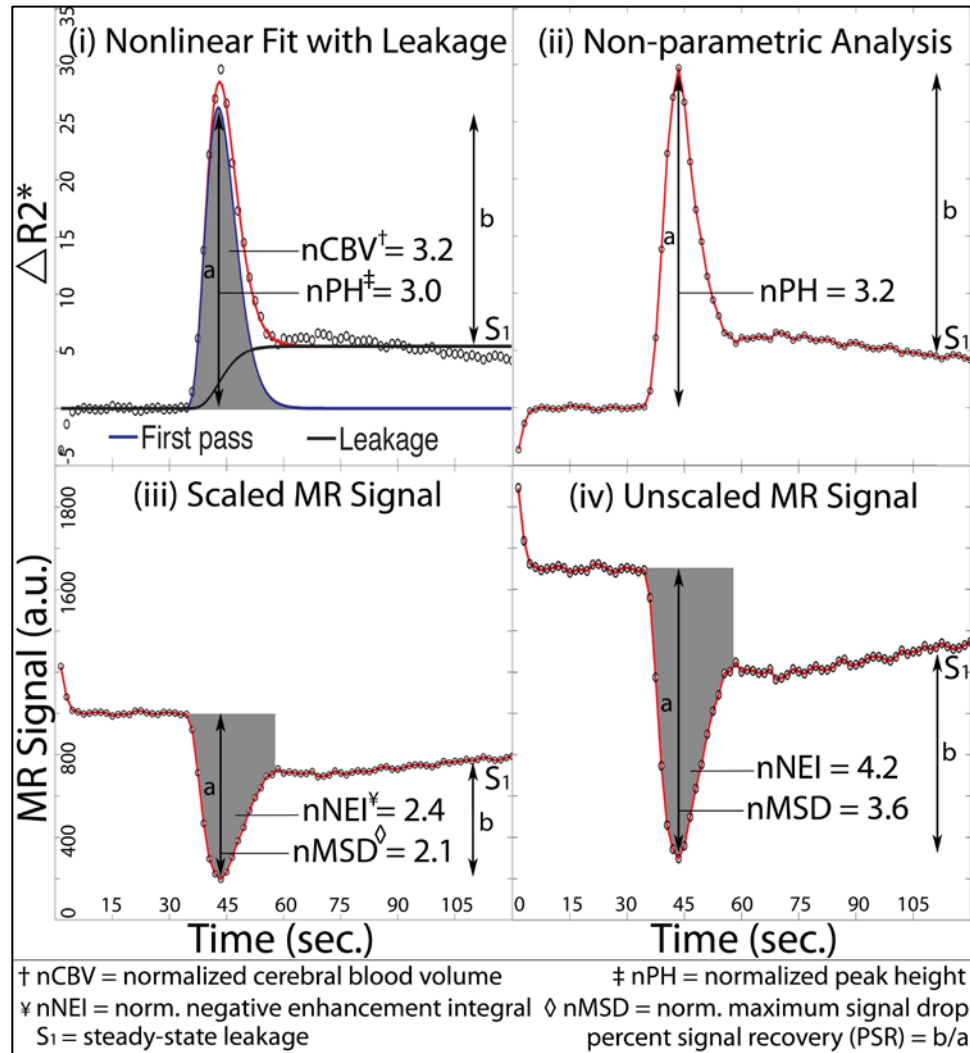
Figure 3.1 illustrates the hemodynamic curve from a single CE-biopsy with complex vasculature calculated using each of the four post-processing methods. The first 5 data points were excluded from parameter calculation to allow for steady-state relaxation to be reached. All blood volume estimates were normalized to the respective blood volume estimate from the NAWM hemodynamic curve to generate relative measures (nCBV, nPH, nNEI, nMSD, as marked in figure).

(i)   **Nonlinear gamma-variate fit with leakage correction** (black curve) is used to calculate the leakage-corrected first-pass (blue curve) from the average ΔR_2^* data (black circles) within the biopsy region. Peak height (PH) = peak of the first pass, cerebral blood volume (CBV) = integral of the first pass and S1 = steady-state height of the leakage component. Percent signal recovery (PSR) = b / a, where b = (PH − S1) and a = PH.

(ii)   **Non-parametric analysis** is used to calculate the hemodynamic curve (red) directly from the average ΔR_2^* data (black circles) in the biopsy region. PH = maximum of the average hemodynamic curve and S1 = average of the last 15 time points acquired. PSR = b / a, where b = PH − S1 and a = PH.

(iii)   **Scaled MR signal analysis** is used to scale the T2* signal intensity to the original baseline level and shift to 1000 MR au. Negative enhancement integral (NEI) is calculated using trapezoidal integration of signal-time curve from initial drop of signal to 3/2*full-width half-max of the first pass, maximum signal drop (MSD) = absolute value of the difference between the minimum of signal-time curve and the baseline average of 5th through 15th time-points, S1 = average of the last 15 time-points. PSR = b / a, where b = absolute value of the difference between the minimum of the signal-time curve and S1 and a = MSD.

(iv)   **Unscaled MR signal analysis** is used to directly calculate perfusion parameters from the raw MR signal-time curve. NEI = trapezoidal integration of signal-time curve from initial signal drop to 3/2 * full-width half-max of the first pass, MSD = absolute value of the difference between the minimum of signal-time curve and the baseline average of 5th through 15th time-point and S1 = average of the last 15 time-points. PSR = b / a, where b = absolute value of the difference between the minimum of the signal-time curve and S1 and a = MSD.

Factor VIII Immunohistochemical Microvascular Staining:

Immunohistochemistry for Factor VIII, rabbit polyclonal antibody (Dako) at 1.2 µg/ml for 20 min at 37°C, was analyzed blinded to the MRI findings by an experienced neuropathologist (J.P.). On the basis of Factor VIII immunostaining, the microvascular morphology was graded as delicate (resembling normal cerebral vessels), simple microvascular hyperplasia (circumferential single cell hyperplasia with definitive lumen), or complex microvascular hyperplasia (circumferential multi-layered and glomeruloid-type vessels). Two features were scored from the factor VIII IHC results, (1) relative contribution of each vascular morphology and (2) overall vascular morphology score. The relative contribution of each vascular morphology to total vascularity within the sample was qualitatively measured on a four-tiered ordinal scale (0, no contribution; 1, minimal; 2, prevalent; 3, predominant) at a magnification of 200x. The overall microvascular morphology score assigned to each tissue sample corresponded to the most abnormal, morphologic-type of vasculature present in the sample as follows: 0, delicate only; 1, simple microvascular hyperplasia; and 2, complex microvascular hyperplasia. For example, samples that contained any contribution of complex hyperplasia were scored as "complex." Whereas, samples that contained a mix of delicate and simple, but no complex vasculature, were scored as "simple." Digital images were captured using a microscope (Olympus, Model BX41TF) and digital camera (Olympus, Model DP70).

Contrast-Enhancing vs. Non-enhancing Classification of Specimens:

Each tissue specimen ROI, in the native DSC resolution, was also overlaid on the T1-weighted post-contrast image in order to determine if the sample originated from a lesion location with contrast-enhancement (CE) or no contrast-enhancement (NE). A

board-certified radiologist (S.C.) evaluated all CE and NE classifications blinded to the DSC findings.

Statistical Analysis:

A random-effects regression model, adjusted for CE categorization at the specimen location and repeated specimen samples per patient, was used to determine if the perfusion parameters from each post-processing method significantly predicted IHC findings. The two types of factor VIII IHC findings, vascular morphology (delicate, simple, complex) and relative contribution of each vascular morphology (0-none to 3-large) were treated as ordinal outcomes on a 3-tiered and 4-tiered scale, respectively. Outcome levels were also grouped to assess whether DSC findings were predictive of complex vasculature (delicate or simple vs. complex) or abnormal vasculature (delicate vs. simple or complex). Binary CE categorization was included as a covariate in each model to adjust for CE at the specimen site, which is known to be associated with increased microvascular density and abnormal perfusion (30).

To assess the association of the perfusion parameters and the ordinal histopathology variables we employed a proportional odds logistic regression model with repeated measures to model the probability of observing a lower vs. a higher response. This model is written as:

$$\log it[P(Y_{ijk} \leq \kappa | X_i, Z_i)] = a_\kappa + x'_{ij}\beta + z'_{ij}b_i; i = 1,...,35; \kappa = 1,...,c-1 \text{ (Equation 2)}$$

where c is the total number of levels of the ordinal variable, X_i is the design matrix for the fixed effects and Z_i for the random effects; x_{ij} and z_{ij} are rows corresponding to the jth biopsy specimen (ranges from 1 to 4); and β & b_i are the vectors of fixed and random

parameters. The intercepts are fixed and category dependent. The odds ratio and p-value for each variable is reported. The ordinal-valued outcome mixed effect models were analyzed with PROC GENMOD in SAS v.9.2.

Significance was assessed at p<.05 for all models. Due to the exploratory nature of the study, no adjustment for type I error was included. Any perfusion parameter that was predictive of IHC results at p<.05, adjusted for CE and repeated sampling, was deemed to be a significant predictor and is presented in the results. The method(s) with the greatest number of significant predictors was determined to be the post-processing method that most reflected underlying vascular histopathology.

3.3 Results:

Tissue Specimen IHC Results:
Table 3.2 summarizes the distribution of vascular morphology observed in the 72 samples obtained from the thirty-five patients with de-novo GBM. The number of samples acquired per patient ranged from 1 to 4 with an average of 2 samples per patient. Patient age ranged from 33 to 85 years old (median = 66) and 25 patients were male and 10 patients were female. 52 (72.2%) of the samples were from CE regions and 20 (27.8%) samples were from NE regions. The highest degree of microvascular hyperplasia within each sample was used to determine the overall microvascular morphology. Among the 72 samples, 16 contained at most delicate microvasculature (delicate), 27 contained at most simple microvascular hyperplasia (simple), and 29 contained complex microvascular hyperplasia (complex). As expected, the majority of complex hyperplasia

was found in the CE specimens (89.6% of specimens with complex were CE), however

approximately half of the CE specimens sampled did not contain complex microvascular

hyperplasia.

Table 3.2: Distribution of biopsy specimens, vascular morphology, and CE/NE classification.

	Delicate:	Simple	Complex	Total:
CE:	9	17	26	52 (72.2%)
NE:	7	10	3	20 (27.8%)
Total:	16 (22.2%)	27 (37.5%)	29 (40.3%)	72 Specimens

Predicting Vascular Morphology using DSC data:

Identification of Microvascular Morphology (delicate, simple, or complex):

The ability of each post-processing method to predict the microvascular

morphology of a tissue was further assessed using the proportional odds logistic

regression statistical analysis. Odds ratios (OR) and significance of each regression

model are reported in **Table 3.3**. Statistical results reflect each parameter adjusted for the

other covariate in the model. For example, in the first model of nonlinear post-processing

in **Table 3.3** (shaded), the top row reports nCBV(nl) adjusted for presence of CE and the

bottom row reports presence of CE adjusted for nCBV(nl) in predicting underlying

vascular morphology.

The nCBV(nl), nPH(nl), and nPH(np) parameters significantly predicted the

underlying vascular morphology ($p < 0.05$, $p = 0.02$, $p = 0.02$, respectively). The

presence of CE, adjusted for blood volume, in each of these models was also a significant

predictor of increasingly abnormal vascular morphology. This is expected since more

samples with hyperplasia (simple or complex) were found in CE specimens than NE

specimens (44 of 52 CE samples compared to 13 of 20 NE samples, **Table 3.2**).

Perfusion parameters from scaled MR signal analysis and unscaled MR signal analysis

were not predictive of vascular morphology.

Table 3.3: Mixed Effects Model Results - DSC perfusion parameters in predicting microvascular morphology by post-processing method

Statistical Results: Predicting Microvascular Morphology (Delicate vs Simple vs Complex)				
Post-Processing Method	Parameter	Odds Ratio	95% Confidence Interval	p-value
Nonlinear	nCBV(nl)	1.578	[1.010, 2.466]	0.045*
	CE Presence	3.490	[1.253, 9.716]	0.016*
	nPH(nl)	1.757	[1.084, 2.848]	0.022*
	CE Presence	3.934	[1.407, 11.000]	0.009*
	PSR(nl)	1.004	[0.978, 1.030]	0.790
	CE Presence	3.928	[1.333, 11.574]	0.013*
Non-Parametric	nPH(np)	1.717	[1.0751, 2.743]	0.024*
	CE Presence	3.702	[1.314, 10.428]	0.013*
	PSR(np)	1.004	[0.966, 1.043]	0.843
	CE Presence	3.871	[1.324, 11.318]	0.013*
Scaled MR Signal	nNEI(sc)	1.675	[0.914, 3.070]	0.095
	CE Presence	3.196	[1.114, 9.171]	0.031*
	nMSD(sc)	1.910	[0.728, 5.015]	0.189
	CE Presence	3.505	[1.223, 10.044]	0.020*
	PSR(sc)	0.991	[0.957, 1.027]	0.627
	CE Presence	3.152	[1.098, 9.054]	0.033*
Unscaled MR Signal	nNEI(unsc)	0.996	[0.719, 1.382]	0.983
	CE Presence	3.658	[1.199, 11.167]	0.023*
	nMSD(unsc)	0.907	[0.614, 1.338]	0.621
	CE Presence	3.652	[1.195, 11.165]	0.023*
	PSR(unsc)	0.992	[0.959, 1.025]	0.621
	CE Presence	3.162	[1.096, 9.124]	0.033*

Table 3.3 displays the mixed effects regression model results of predicting microvascular

morphology based on MRI data. Results are grouped by DSC post-processing method

(left column) and the alternating shading delineates the individual multi-variate models.

Statistical models include two covariates: the DSC-derived perfusion parameter (top row)

and the binary presence of contrast-enhancement (CE, bottom row). Statistical results reflect each parameter adjusted for the other covariate in the model. Note blood volume measures from nonlinear analysis and non-parametric analysis significantly predict vascular morphology, while the other post-processing methods do not.

Figure 3.2 further illustrate the differences among post-processing methods in distinguishing between samples of different vascular morphologies. In **Figure 3.2**, histograms of a blood volume estimate from each of the four post-processing methods (a.-d.) are plotted grouped by the Factor VIII vascular morphology of the tissue samples. Samples with delicate microvasculature are shown in green, simple microvasculature are shown in blue, and samples with complex microvasculature are shown in red.

Note that for nonlinear and non-parametric analyses (**Figure 3.2.a-b**) samples with delicate microvasculature generally cluster at low blood volume (median nCBV(nl) = 1.79 , median nPH(np) = 1.73), simple hyperplasia cluster in mid-range (median nCBV(nl) = 2.15, median nPH(np) = 1.98), and complex hyperplasia cluster in mid-to-high range (median nCBV(nl) = 2.55, median nPH(np) = 2.30). For scaled MR signal (**Figure 3.2.c**) the blood volume estimates of delicate microvasculature cluster in the low range (median nNEI(sc) = 1.78), but simple and complex show high overlap (median nNEI(sc) = 2.00 (simple) , 2.07 (complex)). For unscaled MR signal (**Figure 3.2.d**), the blood volume estimates of samples with delicate, simple, and complex hyperplasia all show high overlap (median nNEI(unsc) = 2.72 (delicate) , 3.04 (simple) , 3.10 (complex)).

Figure 3.2: Blood volume estimate and microvascular hyperplasia of tissue samples by post-processing method.
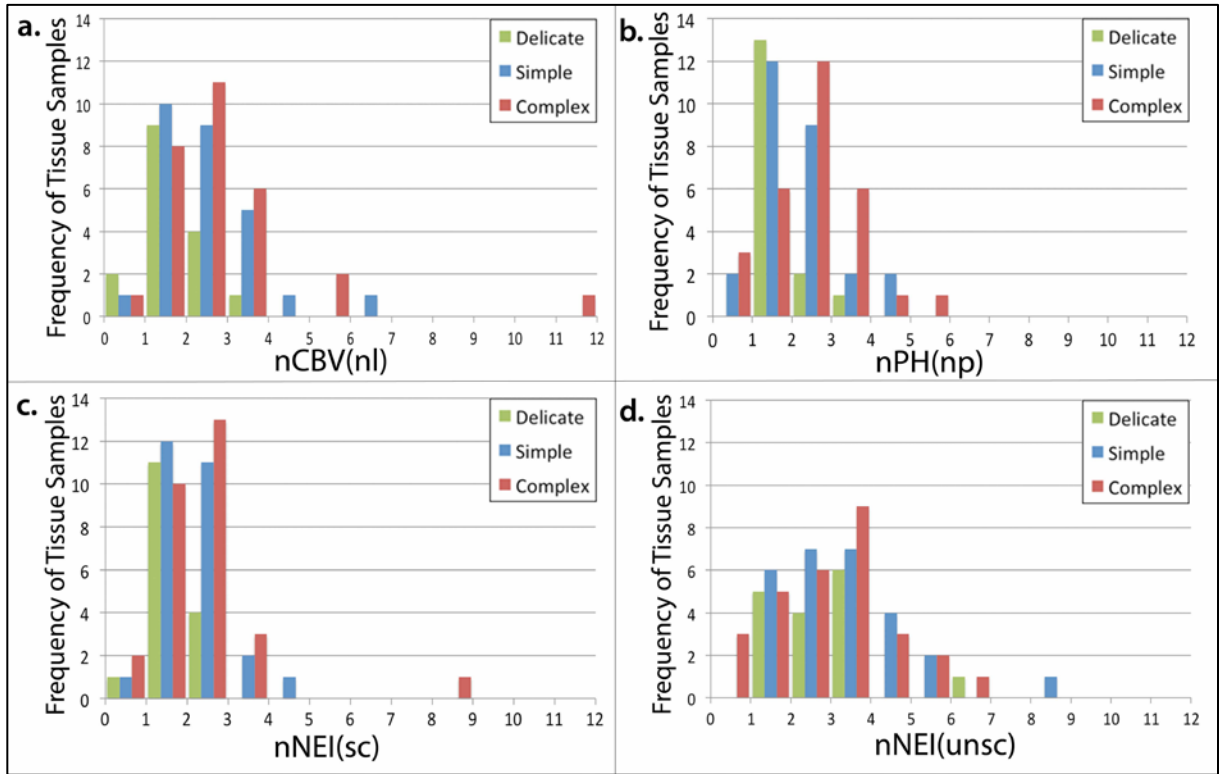
Figure 3.2: Histograms illustrating the distribution of a blood volume estimate calculated from each of the four post-processing strategies within tissue samples of different vascular morphologies. DSC estimates of blood volume include: (a) nCBV(nl), (b) nPH(np), (c) nNEI(sc), and (d) nNEI(unsc). Samples with microvasculature classified as delicate are green, simple are blue, and complex are red. nCBV(nl) (a) and nPH(np) (b) show a more separable pattern between delicate (low-range), simple (mid-range) and complex (mid-to-high range) blood volume. nCBV(nl) (a), nPH(np) (b), and nNEI(sc) (c) show a separable pattern between delicate microvasculature samples (green) and abnormal microvasculature (simple-blue or complex-red) samples, whereas nNEI(unsc) shows high overlap among all vascular morphologies (d).

In general, a one-unit increase in the nonlinear and non-parametric blood volume measures corresponded to approximately 1.7 times increased likelihood of the sample containing microvasculature with a greater degree of hyperplasia (delicate, simple, complex; ORs in **Table 3.3**). **Figure 3.3** illustrates how greater nCBV(nl), nPH(nl), and nPH(np) are predictive of increased microvascular hyperplasia present in the tissue sample.

Figure 3.3: Increasing blood volume measures from nonlinear and non-parametric analyses predict increasingly abnormal microvascular morphology.
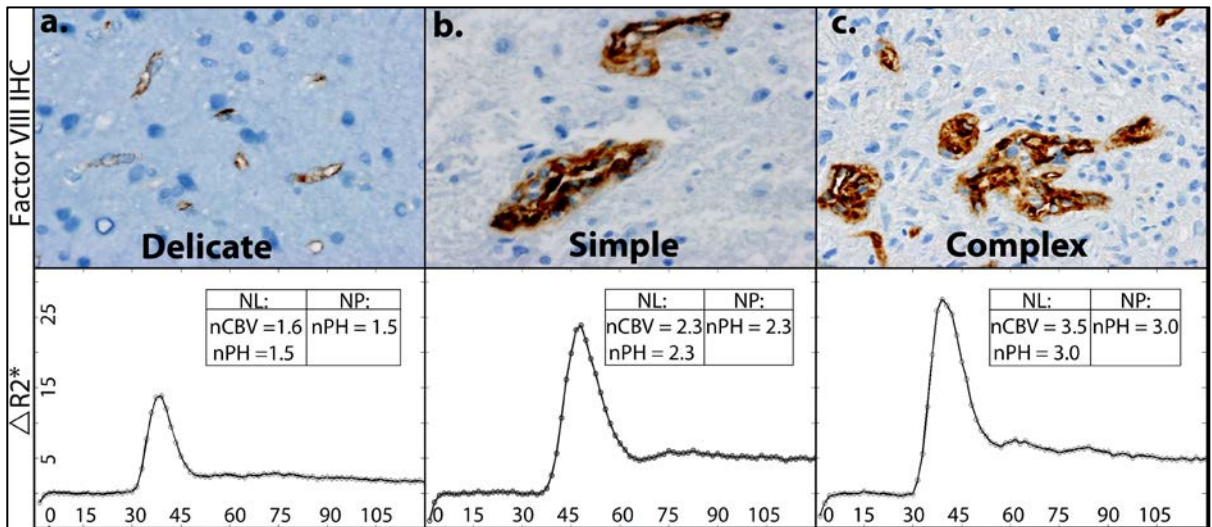
Figure 3.3 depicts IHC staining (top) and corresponding ΔR_2^* curve (bottom) of 3 specimens with delicate, simple, and complex microvascular hyperplasia (a-c). Increased nCBV(nl), nPH(nl), and nPH(np) are significant risk factors for increased microvascular hyperplasia.

Identification of Complex Microvasculature:

The presence of CE was a highly significant covariate in the model predictor of complex hyperplasia in the tissue sample (CE presence covariate: $p<.05$ for each model, **Table 3.4**). Contrast enhancing biopsies were much more likely to contain complex microvascular hyperplasia (see high ORs in Table 3.4), as expected given greater contrast extravasation among markedly abnormal microvasculature. Even when adjusted for the presence of CE categorization, the nCBV(nl), nPH(nl), and nPH(np) were marginally significant risk factors for complex hyperplasia ($p=.09$, $p<.07$, $p<.08$ respectively, **Table 3.4**). Again, perfusion parameters derived from scaled MR signal analysis and unscaled MR signal analysis were not predictive of complex hyperplasia and neither were the PSR measures from any of the four post-processing methods (**Table 3.4**).

Table 3.4: Mixed Effects Model Results - DSC perfusion parameters in predicting complex microvasculature by post-processing method.

Statistical Results: Predicting Complex Microvasculature				
Post-Processing Method	Parameter	Odds Ratio	95% Confidence Interval	p-value
Nonlinear	nCBV(nl)	1.515	[0.933, 2.458]	0.093
	CE Presence	5.583	[1.567, 19.89]	0.008*
	nPH(nl)	1.651	[0.967, 2.820]	0.066
	CE Presence	6.236	[1.739, 22.361]	0.005*
	PSR(nl)	1.002	[0.977, 1.028]	0.872
	CE Presence	5.924	[1.461, 24.023]	0.013*
Non-Parametric	nPH(np)	1.607	[0.946, 2.731]	0.079
	CE Presence	5.891	[1.620, 21.413]	0.007*
	PSR(np)	1.002	[0.966, 1.039]	0.910
	CE Presence	5.857	1.446, 23.717]	0.013*
Scaled MR Signal	nNEI(sc)	1.564	[0.814, 3.006]	0.179
	CE Presence	5.062	[1.350, 18.980]	0.016*
	nMSD(sc)	1.658	[0.568, 4.842]	0.355
	CE Presence	5.438	[1.442, 20.506]	0.012*
	PSR(sc)	0.993	[0.960, 1.027]	0.681
	CE Presence	4.973	[1.167, 21.194]	0.030*
Unscaled MR Signal	nNEI(unsc)	0.926	[0.636, 1.348]	0.688
	CE Presence	5.779	[1.415, 23.608]	0.015*
	nMSD(unsc)	0.809	[0.513, 1.276]	0.362
	CE Presence	5.703	[1.418, 22.931]	0.014*
	PSR(unsc)	0.994	[0.962, 1.027]	0.717
	CE Presence	5.060	[1.199, 21.351]	0.027*

Table 3.4 displays the mixed effects regression model results of predicting complex microvasculature in the tissue sample based on MRI data. Results are grouped by DSC post-processing method (left column) and the alternating shading delineates the individual multi-variate models. Statistical models include two covariates: the DSC-derived perfusion parameter (top row) and the binary presence of contrast-enhancement (CE, bottom row Statistical results reflect each parameter adjusted for the other covariate in the model. Presence of CE is a strong predictor of complex vasculature, as expected given greater extravasation near markedly abnormal vessels with complex hyperplasia, with an odds ratio of approximately 6 across the analysis methods. Interestingly, even adjusted for presence of CE, nCBV(nl), nPH(nl) and nPH(np) are marginally significant predictors of complex hyperplasia.

Identification of Abnormal Microvasculature (Simple or Complex):

The blood volume measures calculated from the nonlinear, non-parametric, and scaled MR signal methods each were significant predictors of the presence of abnormal microvasculature (simple or complex), while the presence of CE categorization was not (nCBV(nl): p=.03, nPH(nl): p<.03; nPH(np): p<.02; nNEI(sc): p<.03, nMSD(sc): p<.05; CE presence in each model: p≥.15). Unscaled MR signal analysis was not predictive of abnormal vasculature and neither were the PSR measures from any of the post-processing methods. 13 of the 20 NE specimens contained abnormal vasculature (simple = 10, complex = 3, **Table 3.2**). **Table 3.5** describes the ORs and significance of each model in predicting abnormal microvasculature. Note that in Figure 3.2, this pattern of elevated blood volume in abnormal microvasculature (blue-simple and red-complex) compared to delicate microvasculature (green) is more evident in panels a – c (nonlinear, non-parametric, and scaled MR signal analysis), than in panel d (unscaled MR signal analysis).

In general, a 1-unit increase in the nonlinear, non-parametric, and scaled MR signal blood volume measures was associated with approximately a 2.3-fold greater likelihood of presence of abnormal microvasculature (ORs in **Table 3.5**). **Figure 3.4** illustrates an example of a patient with abnormal microvasculature (simple or complex hyperplasia) in both the CE and NE tissue, which is reflected by elevated blood volume estimates from the nonlinear, non-parametric, and scaled MR signal analysis methods.

Table 3.5: Mixed Effects Model Results: DSC perfusion parameters in predicting abnormal microvasculature (simple or complex) by post-processing method.

Statistical Results: Predicting Abnormal Microvasculature (Simple or Complex)				
Post-Processing Method	Parameter	Odds Ratio	95% Confidence Interval	p-value
Nonlinear	nCBV(nl)	1.993	[1.054, 3.766]	0.034*
	CE Presence	2.369	[0.611, 9.183]	0.212
	nPH(nl)	2.200	[1.096, 4.416]	0.027*
	CE Presence	2.720	[0.693, 10.670]	0.151
	PSR(nl)	1.009	[0.981, 1.037]	0.540
	CE Presence	3.127	[0.769, 12.710]	0.111
Non-Parametric	nPH(np)	2.232	[1.182, 4.214]	0.013*
	CE Presence	2.495	[0.644, 9.658]	0.186
	PSR(np)	1.012	[0.969, 1.057]	0.597
	CE Presence	3.124	[0.770, 12.673]	0.111
Scaled MR Signal	nNEI(sc)	2.282	[1.100, 4.733]	0.027*
	CE Presence	2.145	[0.553, 8.316]	0.270
	nMSD(sc)	2.942	[1.041, 8.313]	0.042*
	CE Presence	2.462	[0.623, 9.723]	0.199
	PSR(sc)	0.995	[0.955, 1.035]	0.791
	CE Presence	2.331	[0.657, 8.271]	0.190
Unscaled MR Signal	nNEI(unsc)	1.122	[0.765, 1.647]	0.556
	CE Presence	2.526	[0.620, 10.283]	0.196
	nMSD(unsc)	1.074	[0.670, 1.720]	0.768
	CE Presence	2.581	[0.625, 10.663]	0.190
	PSR(unsc)	0.993	[0.957, 1.031]	0.719
	CE Presence	2.268	[0.636, 8.091]	0.207

Table 3.5 displays the mixed effects regression model results of predicting abnormal microvasculature (simple or complex) in the tissue sample based on MRI data. Results are grouped by DSC post-processing method (left column) and the alternating shading delineates the individual multi-variate models. Statistical models include two covariates: the DSC-derived perfusion parameter (top row) and the binary presence of contrast-enhancement (CE, bottom row). Statistical results reflect each parameter adjusted for the other covariate in the model. Blood volume measures derived from nonlinear analysis, non-parametric analysis, and scaled MR signal analysis each significantly predict abnormal vasculature, while presence of CE does not.

Figure 3.4: Abnormal microvasculature detected by blood volume measures from nonlinear and non-parametric analysis, but not CE categorization.
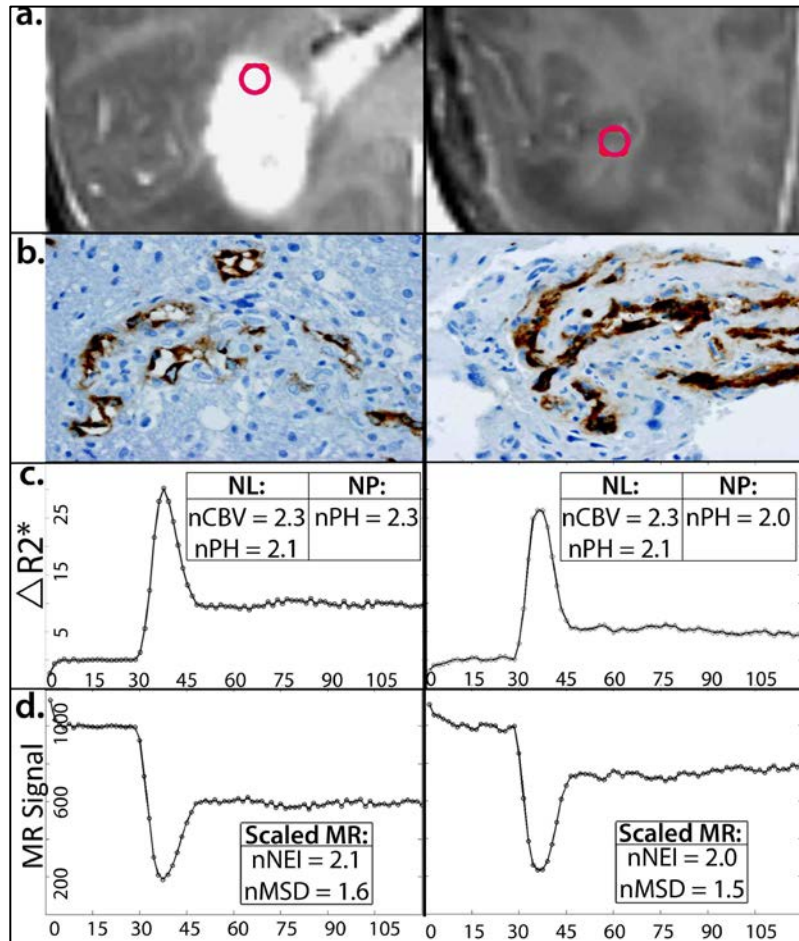
Figure 3.4: T1-weighted, post-contrast MRI of a patient with two tissue samples (a), one in the CE lesion (left) and one in the NE lesion (right). Factor VIII IHC staining demonstrates abnormal microvasculature (simple or complex hyperplasia) in both samples (b), which is reflected by elevated nCBV(nl), nPH (nl), and nPH(np) (c) as well as elevated nNEI(sc) and nMSD(sc) (d). Elevated blood volume estimates from nonlinear, non-parametric, and scaled MR signal post-processing methods detect abnormal hyperplasia within and beyond the CE-lesion.

Predicting Relative Contribution of Microvascular Morphology using DSC data:

Based on immunostaining for Factor VIII the relative contribution of each microvascular pattern to the overall microvasculature, was similarly evaluated to determine if any of the DSC parameters were significant predictors. Adjusted for CE, nPH(nl) and nPH(np) were marginally significant predictors of a predominance of simple hyperplasia in the specimen (nPH(nl): OR = 1.42, p=.06; nPH(np): OR = 1.4, p=.06). In these models, presence of CE was a significant predictor of increased relative contribution of simple hyperplasia, with CE specimens more likely to contain a greater predominance of simple hyperplasia (p=.02, p=.03 respectively). Contrastingly, greater nPH(nl) and nPH(np) were not predictive of the predominance of complex hyperplasia. The scaled MR signal analysis and unscaled MR signal analysis did not yield perfusion parameters predictive of the relative contribution of any of the three vascular morphologies.

3.4 Discussion:

In this retrospective study, tissue samples were collected from patients with treatment-naïve GBM who had received a pre-operative MR imaging examination that included the acquisition of DSC data with a 35° flip angle and single-dose of gadolinium. Four common post-processing methods were applied to the DSC data and evaluated in order to determine whether any of the estimated perfusion parameters could non-invasively predict the underlying tissue microvasculature. It was found that blood volume measures from both the nonlinear and non-parametric analysis of the concentration time

curve significantly predicted the underlying vascular morphology as defined by Factor VIII IHC analysis. Higher values of the nCBV and nPH obtained using the nonlinear fitting method and higher values of the non-parametric estimate of nPH were predictive of a greater degree of hyperplasia, both within the CE and the NE portion of the lesion.

Complex vasculature is a hallmark of GBM and more often present in specimens from the CE lesion. This is in agreement with previous research (13,30). However, not all CE-specimens contained complex vasculature, implying that the tissue within this region has heterogeneous vascular morphology. The nonlinear and non-parametric DSC parameters may therefore assist in guiding sampling toward complex vasculature where it is present. There were only four patients who had a sample with complex vasculature that was represented as having lower blood volume than a sample with simple or delicate vasculature. In re-examining these cases, all four samples were removed from the central core of the CE-lesion or the internal edge of a contrast-enhancing rim around a necrotic core. Partial voluming of low signal from necrosis may have reduced the average hemodynamic curve from these ROIs. This suggests that care must be exercised in interpreting estimates of blood volume from regions that are close to necrosis.

Interestingly, while complex microvasculature was found preferentially in the CE lesion, simple microvasculature was found in specimens from the both the NE and CE lesion. Previous studies have shown abnormal, simple microvasculature to be associated with increased endothelial cellularity and luminal patency (31,32). In a complementary study investigating physiologic MRI correlates of histopathologic features within GBM, which included the patient cohort presented here, tissue samples with simple microvasculature were found to be associated with elevated cellularity, proliferation, and

75

tumor score (manuscript accepted). The availability of a non-invasive method for identifying regions with abnormal microvascular hyperplasia that includes simple and complex morphologies is therefore key to characterizing vascular tumor burden, which often extends outside the CE lesion. Blood volume measures derived from the nonlinear, non-parametric, and scaled MR signal analyses were all able to identify abnormal vasculature, while the CE categorization did not. This suggests that CE alone is not sufficient in visualizing regions with abnormal microvasculature and that these DSC-derived blood volume measurements can identify abnormal microvascular morphology both within and beyond the CE lesion (example in **Figure 3.4).**

DSC perfusion parameters were more reflective of overall morphologic-type of microvasculature in the tissue sample than relative contribution of each vascular morphology within the sample. Both the nonlinear and non-parametric estimates of nPH were marginally predictive of the relative contribution of simple vasculature, while not predictive of the relative contribution of complex vasculature. This could be a limitation of the study since the relative contribution was a more qualitative parameter assessed from the IHC staining than the more general vascular morphology presence parameter. However, this could also reflect the nonlinearity of increasing relative contribution of complex vasculature and blood volume. Specimens with a high degree of complex, glomeruloid vasculature with partially thrombosed or minimally patent vessels may result in slower arrival of gadolinium or greater contrast agent extravasation, which may lead to reduced blood volume measures. Generally, these results support that the MR estimates of blood volume are more predictive of the dominant morphologic-type of

microvasculature present in the sample location, rather than relative contribution of each specific vascular morphology.

The blood volume measurements calculated in this study were more predictive of vascular morphology rather than quantitative assessment of endothelial leakiness. Elevated blood volume may be more characteristic of specific abnormal vascular morphology, while leakiness measures, like PSR, may be more reflective of a combination of vascular type and amount of extravasation within the tissue microenvironment. Blood volume measures from non-parametric and nonlinear analysis were consistently reflective of underlying vasculature; observed through predicting morphology, identifying abnormal vasculature, and highlighting complex vasculature within the CE lesion. Scaled MR signal analysis was only found to be predictive of identifying abnormal vasculature, while the unscaled MR signal analysis was not found to be predictive of any of the IHC results.

Contrast-agent extravasation near areas of compromised BBB leads to competing signal enhancement, which is a known challenge that plagues interpretation of DSC perfusion parameters (9,10,21). Multiple acquisition strategies and post-processing methods exist for addressing this limitation and have been shown to greatly influence the resultant estimates of CBV (10). The acquisition strategy chosen for this study was a 35º flip angle to limit T1-sensitivity, a TE of 54-56 ms to maximize susceptibility contrast, and a single-dose of gadolinium to limit gadolinium exposure for patients. Of the 4 most common post-processing techniques compared, nonlinear and non-parametric analysis were consistently predictive of vascular morphology. Nonlinear gamma-variate fit with leakage correction, while a common method for addressing this extravasation limitation

in the research setting, necessitates curve-fitting, which limits its use in the clinical practice. Non-parametric analysis, which was equally representative of histopathology, is less computationally expensive and may be a better alternative for CBV estimation in the clinical setting. Both the scaled and unscaled MR signal analysis, which are often used in the clinical setting due to their direct ease of use, were not found to be predictive of vascular morphology. This highlights the need for an alternative post-processing method for DSC data that is histopathologically validated and easy-to-use in clinical practice. An open-source, freely available software package with non-parametric DSC post-processing analysis is currently being developed (33,34) such that these non-invasive blood volume measures can be used more reliably in clinical practice.

In conclusion, this study provides histopathological support for using both non-parametric and nonlinear post-processing techniques in conjunction with low flip angle DSC imaging data as noninvasive methods for characterizing microvascular hyperplasia within GBM. The non-parametric analysis method and acquisition strategy that requires a single injection of a standard dose of gadolinium may be particularly useful in the clinic, as it requires less computational expense and limits the potential side effects associated with gadolinium. The findings from this study also suggest that blood volume measurements derived in the manner described may assist in both guiding sites of tissue sampling to regions with vascular features characteristic of GBM and in identifying and monitoring patients with highly vascular GBM who may benefit from targeted antiangiogenic therapy.

3.5 References:

1. Chang SM, Lamborn KR, Kuhn JG, et al. Neurooncology clinical trial design for targeted therapies: lessons learned from the North American Brain Tumor Consortium. Neuro Oncol 2008;10(4):631-642.
2. Wen PY, Macdonald DR, Reardon DA, et al. Updated response assessment criteria for high-grade gliomas: response assessment in neuro-oncology working group. J Clin Oncol 2010;28(11):1963-1972.
3. Cha S, Tihan T, Crawford F, et al. Differentiation of low-grade oligodendrogliomas from low-grade astrocytomas by using quantitative blood-volume measurements derived from dynamic susceptibility contrast-enhanced MR imaging. AJNR Am J Neuroradiol 2005;26(2):266-273.
4. Saito T, Yamasaki F, Kajiwara Y, et al. Role of perfusion-weighted imaging at 3T in the histopathological differentiation between astrocytic and oligodendroglial tumors. [published online ahead of print May 2, 2011]. Eur J Radiol. PMID: 21543173 [PubMed - as suplied by publisher].
5. Nelson SJ. Assessment of therapeutic response and treatment planning for brain tumors using metabolic and physiological MRI. NMR Biomed 2011;24(6):734-749.
6. Fuller GN, Scheithauer BW. The 2007 Revised World Health Organization (WHO) Classification of Tumours of the Central Nervous System: newly codified entities. Brain Pathol 2007;17(3):304-307.
7. Rojiani AM, Dorovini-Zis K. Glomeruloid vascular structures in glioblastoma multiforme: an immunohistochemical and ultrastructural study. J Neurosurg 1996;85(6):1078-1084.
8. Rosen BR, Belliveau JW, Vevea JM, Brady TJ. Perfusion imaging with NMR contrast agents. Magn Reson Med 1990;14(2):249-265.
9. Weisskoff RM. Simultaneous blood volume and permeability mapping using a single GD-based contrast injection. In: Proceedings of the 2nd Annual Meeting of ISMRM 1994;San Francisco:279.
10. Paulson ES, Schmainda KM. Comparison of dynamic susceptibility-weighted contrast-enhanced MR methods: recommendations for measuring relative cerebral blood volume in brain tumors. Radiology 2008;249(2):601-613.
11. Lupo JM, Cha S, Chang SM, Nelson SJ. Dynamic susceptibility-weighted perfusion imaging of high-grade gliomas: characterization of spatial heterogeneity. AJNR Am J Neuroradiol 2005;26(6):1446-1454.
12. Cha S, Lu S, Johnson G, Knopp EA. Dynamic susceptibility contrast MR imaging: correlation of signal intensity changes with cerebral blood volume measurements. J Magn Reson Imaging 2000;11(2):114-119.
13. Barajas RF, Jr., Hodgson JG, Chang JS, et al. Glioblastoma multiforme regional genetic and cellular expression patterns: influence on anatomic and physiologic MR imaging. Radiology 2010;254(2):564-576.
14. Law M, Meltzer DE, Wetzel SG, et al. Conventional MR imaging with simultaneous measurements of cerebral blood volume and vascular permeability in ganglioglioma. Magn Reson Imaging 2004;22(5):599-606.

15. Lee MC, Cha S, Chang SM, Nelson SJ. Dynamic susceptibility contrast perfusion imaging of radiation effects in normal-appearing brain tissue: changes in the first-pass and recirculation phases. J Magn Reson Imaging 2005;21(6):683-693.

16. Heiland S, Benner T, Debus J, Rempp K, Reith W, Sartor K. Simultaneous assessment of cerebral hemodynamics and contrast agent uptake in lesions with disrupted blood-brain-barrier. Magn Reson Imaging 1999;17(1):21-27.

17. Vonken EP, van Osch MJ, Bakker CJ, Viergever MA. Simultaneous quantitative cerebral perfusion and Gd-DTPA extravasation measurement with dual-echo dynamic susceptibility contrast MRI. Magn Reson Med 2000;43(6):820-827.

18. Uematsu H, Maeda M, Sadato N, et al. Blood volume of gliomas determined by double-echo dynamic perfusion-weighted MR imaging: a preliminary study. AJNR Am J Neuroradiol 2001;22(10):1915-1919.

19. Hu LS, Baxter LC, Smith KA, et al. Relative cerebral blood volume values to differentiate high-grade glioma recurrence from posttreatment radiation effect: direct correlation between image-guided tissue histopathology and localized dynamic susceptibility-weighted contrast-enhanced perfusion MR imaging measurements. AJNR Am J Neuroradiol 2009;30(3):552-558.

20. Hu LS, Baxter LC, Pinnaduwage DS, et al. Optimized preload leakage-correction methods to improve the diagnostic accuracy of dynamic susceptibility-weighted contrast-enhanced perfusion MR imaging in posttreatment gliomas. AJNR Am J Neuroradiol 2010;31(1):40-48.

21. Boxerman JL, Schmainda KM, Weisskoff RM. Relative cerebral blood volume maps corrected for contrast agent extravasation significantly correlate with glioma tumor grade, whereas uncorrected maps do not. AJNR Am J Neuroradiol 2006;27(4):859-867.

22. Cha S, Lupo JM, Chen MH, et al. Differentiation of glioblastoma multiforme and single brain metastasis by peak height and percentage of signal intensity recovery derived from dynamic susceptibility-weighted contrast-enhanced perfusion MR imaging. AJNR Am J Neuroradiol 2007;28(6):1078-1084.

23. Essock-Burns E, Lupo JM, Cha S, et al. Assessment of perfusion MRI-derived parameters in evaluating and predicting response to antiangiogenic therapy in patients with newly diagnosed glioblastoma. Neuro Oncol 2011;13(1):119-131.

24. Elkhaled A JL, Phillips JJ, et al. Magnetic resonance of 2-hydroxyglutarate in IDH1-mutated low-grade gliomas. Sci Transl Med 2012;4(116ra5).

25. Crawford FW, Khayal IS, McGue C, et al. Relationship of pre-surgery metabolic and physiological MR imaging parameters to survival for patients with untreated GBM. J Neurooncol 2009;91(3):337-351.

26. Saraswathy S, Crawford FW, Lamborn KR, et al. Evaluation of MR markers that predict survival in patients with newly diagnosed GBM prior to adjuvant therapy. J Neurooncol 2009;91(1):69-81.

27. Studholme C HD, Hawkes D. An overlap invariant entropy measure of 3D medical image alignment. . Pattern Recognition 1999;3:16.

28. Rueckert D, Sonoda LI, Hayes C, Hill DL, Leach MO, Hawkes DJ. Nonrigid registration using free-form deformations: application to breast MR images. IEEE Trans Med Imaging 1999;18(8):712-721.

29. Lupo JM, Cha S, Chang SM, Nelson SJ. Analysis of metabolic indices in regions of abnormal perfusion in patients with high-grade glioma. AJNR Am J Neuroradiol 2007;28(8):1455-1461.

30. Jain R, Narang J, Gutierrez J, et al. Correlation of immunohistologic and perfusion vascular parameters with MR contrast enhancement using image-guided biopsy specimens in gliomas. Acad Radiol 2011;18(8):955-962.

31. Miyagami M, Katayama Y. Angiogenesis of glioma: evaluation of ultrastructural characteristics of microvessels and tubular bodies (Weibel-Palade) in endothelial cells and immunohistochemical findings with VEGF and p53 protein. Med Mol Morphol 2005;38(1):36-42.

32. Izycka-Swieszewska E. [Immunomorphological analysis of the vascular stroma in glioblastoma]. Neurol Neurochir Pol 2003;37(1):59-71.

33. Crane JC OM, Essock-Burns E, Lupo JM, Nelson SJ. Visualization and Analysis of Dynamic MRSI and Perfusion MRI Using the Open-Source SIVIC Software Framework. 97th Annual meeting of RSNA 2011;Chicago, IL(Exhibit LL-INE1174).

34. Crane JC OM. SIVIC. https://sourceforgenet/projects/sivic/; 2011.

CHAPTER 4 : Comparison of Leakage-Mitigating DSC-Acquisition Strategies on estimates of Cerebral Blood Volume in Patients with Glioma: Preload and Flip Angle

In this chapter, two DSC acquisition strategies for addressing leakage are compared in order to make a recommendation for a DSC protocol that yields the more repeatable estimates of blood volume. The addition of a "preload" prior to DSC acquisition is assessed in conjunction with either a low flip angle (FA) or high FA. When a preload is applied prior to high FA DSC, the blood volume measures are greatly altered, regardless of further post-processing correction. In contrast, when a preload is applied prior to low FA DSC, the resultant blood volume measures remain relatively unchanged compared to results obtained without a preload. This work provides support for acquiring DSC with a low FA to obtain blood volume estimates [Chapter 3] as this can be achieved without requiring an additional preload and limits the total gadolinium exposure to the patient.

4.1 Introduction:

Dynamic susceptibility contrast MR-imaging is a method that has been shown to be useful for noninvasively assessing tumor vascularity and perfusion for patients with glioma. Relative estimates of regional cerebral blood volume (rCBV) can be derived from acquiring dynamic T2 or T2* weighted images during and following a bolus injection of gadolinium contrast. The intravascular compartmentalization of the contrast bolus causes a susceptibility gradient which results in signal loss from T2* dephasing. This change in MR signal can be converted to change in relaxivity, which has been shown to be proportional to concentration of the contrast agent [1]. However, breakdown of the blood-brain barrier, common in high-grade gliomas, can allow contrast agent extravasation. This complicates DSC quantification, as the leaked contrast agent causes T1-shortening and a reduction in intravascular compartmentalization, which challenges the assumption of linearity between DeltaR2* and concentration. The complex interplay of T1- and T2-effects caused by contrast extravasation, has lead to the development of a number of methods for correcting this effect. These methods include using a low flip angle (FA) for data acquisition [2-6], a dual-echo acquisition [7-9], alternate contrast agents such as ferumoxytol [10], and post-processing methods for leakage corrections [7, 11-12].

Another method that is increasingly being employed in research and clinical setting is to give a partial or single dose of gadolinium prior to DSC acquisition, called a "preload," in order to counter the effects of signal increase due to contrast extravasation

by saturating the leakage space and reducing the initial T1 of the tissue [7, 10, 12]. In conjunction with a high flip angle (60˚or 90˚, respectively), this preload method has been shown to yield estimates of rCBV that have increased accuracy in discriminating between tumor recurrence and post-treatment effects [12] and have greater repeatability between post-processing methods [7]. However, the addition of a preload to the imaging protocol increases the total gadolinium dose a patient receives. Exposing patients to increased gadolinium heightens the associated risk of nephrogenic systemic fibrosis (NSF), which is a serious condition causing fibrosis of connective tissues in patients with impaired renal function, and needs to be taken into account when designing standardized MRI protocols [13]. While the addition of a preload has been shown to improve estimates of MR parameters from high flip angle DSC, it is unknown whether a preload significantly alters the perfusion estimates derived from low-flip angle DSC for patients with glioma. In this study we hypothesized that acquiring DSC data with a low-FA may sufficiently limit the competing T1-effects, so that the additional risks due to gadolinium exposure from preload correction may not be necessary.

DSC has the potential to facilitate patient management, but in order for it to transition more widely to the clinic, there is a clear need for standardization of acquisition protocols. Identifying protocols that yield blood volume measures that are both repeatable and biologically relevant is paramount to successful clinical translation. The goal of this study was to determine whether the addition of a preload of Gadolinium differentially influenced the DSC data acquired from patients with glioma using either low or high FA data acquisition strategies.

4.2 Materials and Methods:

MRI Acquisition:

Fourteen patients diagnosed with glioma were included in this study. Each patient

received a 3T MRI exam that included both standard anatomic imaging and DSC

imaging. Anatomic imaging comprised sagittal T2-weighted FLAIR (TE= 134 ms,

TR=6000 ms, TI = 1800 ms, slice thickness = 1.5 mm, matrix = 512x512, FOV = 28

x28cm) and pre- and post-contrast T1-weighted 3D IRSPGR (TE = 2.5 ms, TR = 7.8 ms,

TI = 400 ms, slice thickness = 1.5 mm, matrix= 256x256, FOV = 24 x 24cm, with

SENSE R=2).

During the exam, DSC data were acquired twice from each patient (**Figure 4.1**).

Each dataset was acquired following a bolus of 0.05 mmol/kg gadolinium contrast

(Magnevist®, Bayer Healthcare) for a total gadolinium dose of 0.1 mmol/kg per patient.

Both contrast injections were administered at the same speed (2 – 3 ml/s depending on

patient weight) using a power injector [Spectris Solaris EP®, Medrad]. Administering

the DSC injections in this manner allowed the contrast injected during the first DSC

dataset to act as a "preload" for the second DSC acquisition. Perfusion parameters

derived from a patient's first DSC acquisition are therefore without preload (Pre-) and the

parameters derived from the patient's second DSC acquisition are with preload (Pre+).

There was a 6-10 minute delay between DSC injections to achieve recommended

"incubation" time for preload to be most effective [12].

Patients were randomly assigned to either the Low-FA group or High-FA group.

For patients in the Low-FA group, both sets of DSC data were acquired with a 35° FA.

For patients in the High-FA group, both sets of DSC data were acquired with a 90° FA.

All other DSC parameters remained consistent between Group A and Group B (TE = 54

ms, TR = 1500 ms, 4mm slice thickness, matrix = 128x128, FOV = 24cm x 24cm).

Figure 4.1: Study Design
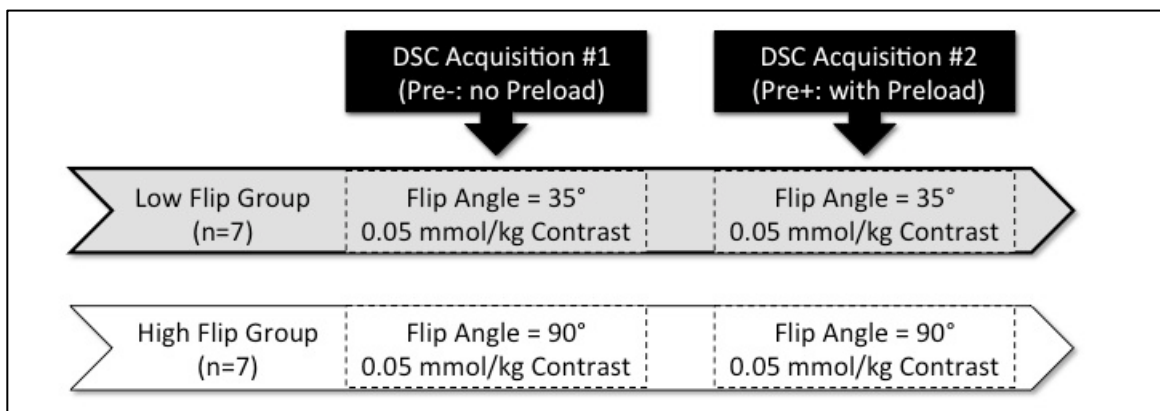
Post-Processing:

MRI data was transferred to a UNIX workstation (SUN Microsystems) for post-

processing. The same processing was applied to both the first DSC dataset (Pre-) and the

second DSC dataset (Pre+). DSC datasets were each non-rigidly aligned to the pre-

contrast T1-weighted anatomic images. The normal appearing white matter (NAWM)

was defined on the pre-contrast T1-weighted image by applying auto-segmentation

methods as previously described [14]. The NAWM mask was then resampled to the

perfusion data resolution and a morphologic erosion was applied to create a conservative

NAWM mask to use for comparing the Pre- and Pre+ perfusion datasets. Regions of

interest (ROIs) of the non-enhancing lesion and the contrast-enhancing lesion (if it

existed) were semi-automatically contoured on the FLAIR and T1-weighted post-contrast

images, respectfully. The putative tumor ROI was defined as including both the non-

enhancing lesion, corresponding to FLAIR hyperintensity, and any contrast-enhancing

lesion. ROIS were resampled to the perfusion data resolution. Care was taken to exclude

any regions of necrosis, surgical cavity, or cerebral spinal fluid.

Parametric maps of perfusion data were generated using two post-processing

methods: nonlinear fit with leakage correction (nl) [15] and non-parametric analysis (np)

[16]. These methods have been previously described [Chapter 3]. Briefly, the nonlinear

method was used to calculate leakage-corrected estimates of relative cerebral blood

volume (rCBV.nl) and peak height (PH.nl). The non-parametric method was used to

calculate model-free estimates directly from the ΔR_2^* hemodynamic-curve of PH.np. The

3 blood volume measures were normalized to the average within the NAWM. This

normalization was applied separately to the Pre- and Pre+ data. These two post-

processing methods were investigated as they both have been shown to yield biologically

relevant estimates of blood volume and are commonly used in the literature [Chapter 3,

[3, 16-17]] for data both with and without preload

Statistical Analysis:

The intra-patient variability between preload conditions was assessed in two ways. First, a region-level comparison was drawn between the histogram distributions of the DSC data from both the Pre- and Pre+ acquisitions. This analysis was applied separately to data within the NAWM and to data within the tumor region. For the region-level comparison, maps were generated at the in-plane resolution of the perfusion data (3mm). Within-patient change between the Pre- and Pre+ perfusion estimates was assessed using a Wilcoxon sign-rank test of the median parameter value within the ROI (NAWM or putative tumor). This analysis was repeated for both the Low-FA and High-FA patients.

The second analysis comprised a voxel-wise comparison in which the percent change of the Pre- and Pre+ perfusion estimates was determined on a voxel-by-voxel basis. In this case the perfusion maps were generated at the lower in-plane resolution of 5mm, to further mitigate any intra-exam alignment errors. This analysis was applied separately to voxels within the two distinct ROIs (NAWM and tumor). The median within the ROI of the voxel-wise percent change between Pre- and Pre+ acquisitions was calculated for each patient. A Wilcoxon rank-sum test was used to compare the median percent change between patients in the Low-FA and High-FA groups. Due to the exploratory nature of this study no formal adjustment of Type I error was undertaken. In all cases, $p \leq .05$ was considered statistically significant.

Table 4.1: Study population.

Study Population: Clinical Background			
	Grade	Age	CE-Lesion
Low-FA Group: (35°)	Grade I	39	No
	Grade II	26	No
	Grade III	51	No
	Grade III	48	No
	Grade III	43	Yes
	Grade III/IV	33	Yes
	Grade IV	28	Yes
High-FA Group: (90°)	Grade II	45	No
	Grade II	28	No
	Grade II	45	No
	Grade II	65	No
	Grade II	52	No
	Grade II	56	Yes
	Grade IV	40	Yes

4.3 Results:

Table 4.1 describes the histological grade for patients randomly assigned to the Low-FA and High-FA groups. The median [range] age was similar in both groups (Low-FA = 39 [28, 51]; High-FA: = 45 [28, 65]). The tumor-regions of these patients were predominantly non-enhancing lesions, with additional contrast-enhancement observed in 3 patients in the Low-FA and 2 patients in the High-FA group.

Region-Level Comparison:

NAWM:

Patients in the High-FA group showed significantly increased median blood volume within the NAWM at the Pre+ acquisition compared to the estimates from the Pre- acquisition. Further, the Pre+ blood volume estimates of the High-FA patients were significantly elevated regardless of post-processing method (Wilcoxon sign-rank, nPH.np: $p<.02$, nPH.nl: $p<.02$, nCBV.nl: $p<.02$**; Table 4.2**). Whereas, for the patients in the Low-FA group, the median blood volume in the NAWM remained stable and did not significantly change between Pre- and Pre+ conditions (nPH.np: $p=.94$, nPH.nl: $p=.58$, nCBV.nl: $p=.11$; **Table 4.2**). **Figure 4.2** shows $\Delta R2^*$ traces from the Pre- and Pre+ acquisitions of tissue within the NAWM for an example patient from the High-FA (top) and Low-FA (bottom) groups. Note that the Pre+ hemodynamic curve (pink) is noticeably elevated compared to the Pre- curve (white) for the High-FA patient, while they are very similar for the Low-FA patient.

Figure 4.2: Overlaid Pre- and Pre+ ΔR2* traces from a Low-FA and a High-FA patient.
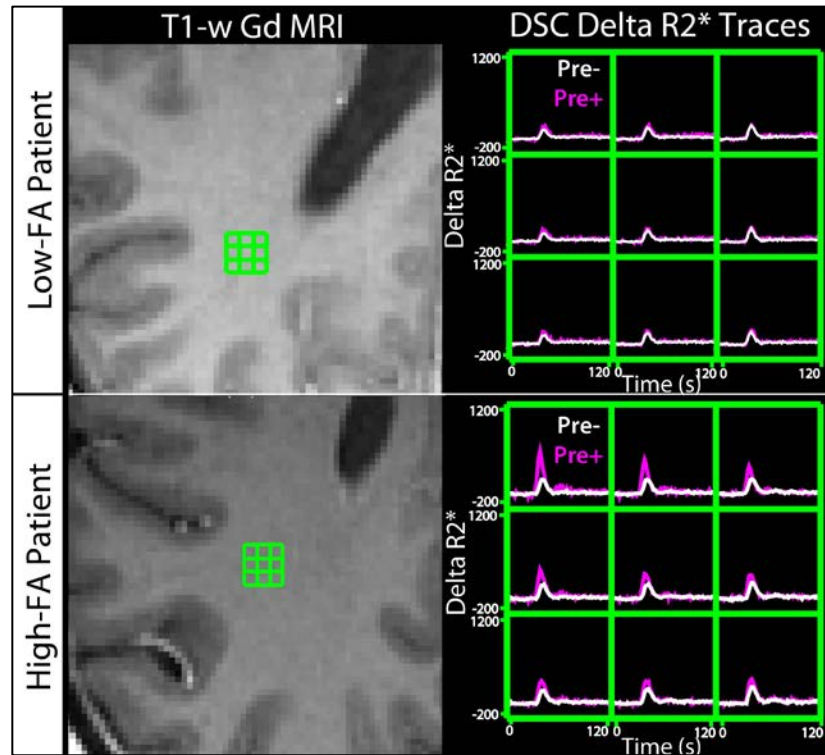
Figure 4.2 illustrates the Pre- (white) and Pre+ (pink) ΔR2* hemodynamic traces from two example patients: a Low-FA patient (top) and High-FA patient (bottom). Left: The selected voxels (green boxes) are shown overlaid on T1-weighted post-contrast MRI (left) and are within the NAWM. Right: The corresponding Pre- and Pre+ ΔR2* traces are very similar for the Low-FA patient, while the Pre+ trace is elevated for the High-FA patient.

Tumor-Region:

Patients in the High-FA group generally had elevated Pre+ blood volume in the tumor-region compared to Pre- blood volume, but this change did not reach statistical significance (**Table 4.2** - bottom). In contrast, the majority of patients in the Low-FA

91

group had relatively stable median blood volume in the tumor-region between Pre+ and Pre- acquisition (**Table 4.2** - top).

This difference was clearly noticeable within the contrast-enhancing lesion. **Figure 4.3** illustrates Pre- and Pre+ hemodynamic traces from within the contrast-enhancing lesion of a Low-FA patient and a High-FA patient. Note that the traces are relatively similar from the Low-FA patient, while they are quite different for the High-FA patient. The Pre- trace from the contrast-enhancing lesion of the High-FA patient illustrates large leakage contamination with the post-bolus data passing beyond baseline (dashed green line). The Pre+ trace from this same patient has elevated PH and does not pass beyond baseline, illustrating the leakage-correcting effect of the preload at this flip angle. The resultant blood volume estimates within the contrast enhancing lesion from the High-FA patient are greatly altered by the presence of a preload, while the blood volume estimates from the Low-FA patient remained stable.

Table 4.2: Region-Level Comparison - Median blood volume estimate within ROI from Pre- (no preload) and Pre+ (with preload) DSC data by flip angle group.

		nPH.np		nPH.nl		nCBV.nl	
		Pre-	Pre+	Pre-	Pre+	Pre-	Pre+
Low-FA	NAWM	0.96 [0.96,0.98]	0.97 [0.951, 0.98]	0.91 [0.90, 0.92]	0.92 [0.91, 0.94]	0.92 [0.91, 0.92]	0.93 [0.90, 0.95]
	Tumor	0.80 [0.68, 1.04]	0.80 [0.67, 1.08]	0.83 [0.63, 1.01]	0.83 [0.62, 1.14]	0.79 [0.66, 0.98]	0.97 [0.65, 1.10]
High-FA	NAWM	0.94 [0.94, 0.96]	1.03* [1.01,1.04]	0.94 [0.90,0.96]	1.07* [1.02,1.19]	0.94 [0.90, 0.95]	1.07* [1.02,1.19]
	Tumor	0.56 [0.40,0.61]	0.51 [0.48, 0.64]	0.67 [0.57, 0.75]	0.80 [0.58, 1.09]	0.78 [0.67, 0.93]	0.88 [0.67, 1.03]

Data is presented as group median [inner quartile range (IQR)].

* Significant within-patient change between Pre- and Pre+; Wilcoxon sign-rank, p≤.05

Figure 4.3: Overlaid Pre- and Pre+ ΔR2* traces from a Low-FA and a High-FA patient within contrast-enhancing lesion.
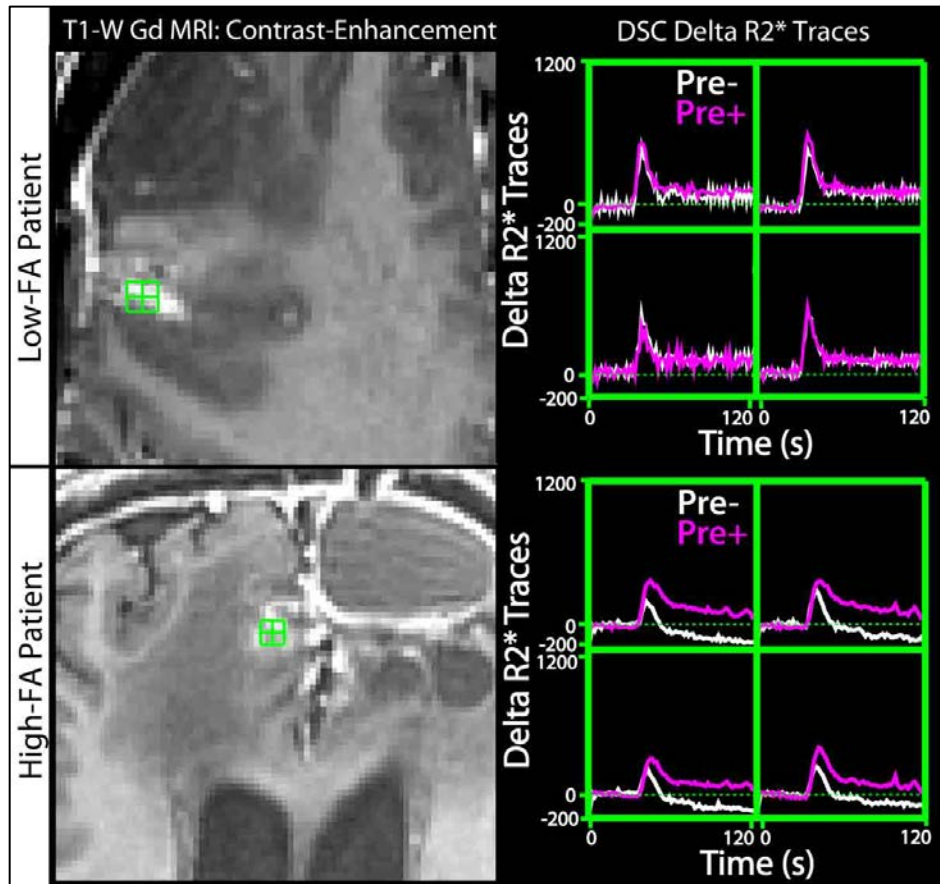
Figure 4.3 illustrates the Pre- (white) and Pre+ (pink) ΔR2* hemodynamic traces from two example patients: a Low-FA patient (top) and High-FA patient (bottom). Left: The selected voxels (green boxes) are shown overlaid on T1-weighted post-contrast MRI (left) and are within the contrast-enhancing lesion. Right: The corresponding Pre- and Pre+ ΔR2* traces are very similar for the Low-FA patient, while the Pre- and Pre+ traces for the High-FA patient differ greatly. The Pre- data from the High-FA patient shows clear leakage contamination (post-bolus data recovers beyond baseline), while the Pre+ data appears corrected (reduced post-bolus signal recovery, reduced PH). Within the contrast-enhancing lesion, the addition of a preload greatly alters High-FA data (bottom), but not Low-FA data (top).

Voxel-wise Comparison:

NAWM:

The paired voxel-wise percent change between Pre- and Pre+ blood volume estimates differed greatly between the Low-FA and High-FA groups. Median voxel-wise percent change of the blood volume estimates was significantly greater in the High-FA patients than in the Low-FA patients (Wilcoxon rank-sum, nPH.np: p=.002, nPH.nl: p=.001, nCBV.nl: p=.001, **Table 4.3**). **Figure 4.4** illustrates boxplots of the percent change for both of the FA groups. As shown in **Figure 4.4**, High-FA patients showed significantly greater voxel-wise percent change regardless of post-processing method.

Figure 4.4: Voxel-wise percentage change of blood volume between Pre- and Pre+ by flip-angle groups.
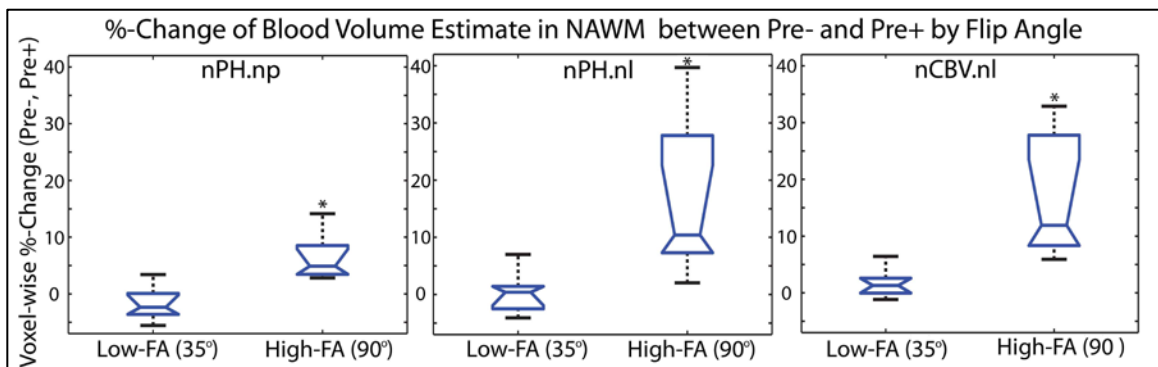
Figure 4.4 illustrates box-plots of voxel-wise percentage change between Pre- and Pre+ blood volume measures for the FA groups. Patients in the High-FA group had a significantly greater percentage change between Pre- and Pre+ acquisitions, regardless of post-processing method (*p<.002, Wilcoxon Rank-sum). High-FA had a large, variable increase in Pre+ blood volume measures, whereas Low-FA patients remained stable with

little change in Pre+ blood volume. NAWM is displayed, as this region is most directly

comparable between FA groups.

Tumor-Region:

The median of the voxel-wise percentage change was greater for High-FA for

each blood volume measure, but only the nPH.nl estimate reached statistical significance

(**Table 4.3**: median change: Low-FA = 0.79%, High-FA = 19.96%, Wilcoxon rank-sum;

p=.05). This difference was exaggerated in the patients with contrast-enhancing lesions

(**Figure 4.3**), but the small number of patients with contrast-enhancement limited further

analysis.

Table 4.3: Voxel-wise Comparison - Median percent change of blood volume in ROI between Pre- (no preload) and Pre+ (with preload) DSC data by flip-angle group.

		nPH.np %Δ(Pre-,Pre+)	nPH.nl %Δ(Pre-,Pre+)	nCBV.nl %Δ(Pre-,Pre+)
NAWM	Low-FA	-2.36% [-3.36%,-0.21%]	0.40% [-1.90%, 1.27%]	1.30% [0.06%, 2.37%]
	High-FA	4.90%* [3.74%, 8.04%]	10.38%* [7.97%, 23.3%]	11.91%* [8.72%, 22.78%]
	P-value	0.002	0.001	0.001
Tumor	Low-FA	0.01% [-5.83%, 1.99%]	0.79% [-4.50%, 3.39%]	5.96% [0.88%, 10.65%]
	High-FA	8.10% [1.54%, 10.88%]	8.05%* [6.23%, 37.77%]	7.22% [-3.74%, 31.86%]
	P-value	0.097	0.053	0.710

Data is presented as group median [IQR].

* Significant difference between FA groups, Wilcoxon rank-sum, p≤.05

To further investigate the interplay between post-processing leakage-correction and preload under the two FA paradigms, we compared the nPH.nl and nPH.np from Pre- and Pre+ data. Among High-FA patients, the leakage-corrected nPH.nl was significantly greater than the uncorrected nPH.np for both the Pre- and Pre+ data (**Table 4.3**, Wilcoxon sign-rank, p=.02; p=.02). In contrast, among Low-FA patients, there was no significant change when leakage-correction was applied to either the Pre- or Pre+ data (**Table 4.3**, Wilcoxon sign-rank, p=.30; p=.30).

Table 4.4: Post-processing Comparison - Median blood volume estimate within tumor region without post-processing leakage correction (nPH.np) and with post-processing leakage correction (nPH.nl).

	Pre-		Pre+	
	nPH.np	nPH.nl	nPH.np	nPH.nl
Low-FA	0.80 [0.68, 1.04]	0.83 [0.63, 1.01]	0.80 [0.67, 1.08]	0.83 [0.62, 1.14]
High-FA	0.56 [0.40,0.61]	0.67* [0.57, 0.75]	0.51 [0.48, 0.64]	0.80* [0.58, 1.09]

Data is presented as group median [IQR].

Data is grouped by preload condition (Pre- or Pre+) and separated by Flip Angle Group.

* Significant within-patient difference between nPH.np and nPH.nl, Wilcoxon sign-rank, p≤.05

4.4 Discussion:

In order for DSC imaging to be successfully translated into wide clinical use, practical factors of post-processing expense and ease of integration into clinical protocols need to be considered in addition to the challenges in quantifying DSC data. The addition of a gadolinium preload and the use of a low flip angle for DSC acquisition are two strategies that have been implemented to address challenges of contrast agent extravasation near BBB breakdown. These methods have been shown to yield blood volume estimates predictive of vascular features that can aid in the assessment of response and diagnosis for patients with glioma [Chapter 3, [18]]. These acquisition strategies also have associated tradeoffs, as the addition of a preload increases patient risk of NSF and the use of a low FA (35) may decrease SNR requiring higher field imaging. In this study, we aimed to determine whether an additional preload of gadolinium substantially altered the estimates of blood volume and leakiness in glioma patients when acquired at low FA compared to high FA, in order to form a recommendation for clinical DSC acquisition.

For High-FA (90) DSC acquisition, blood volume estimates were increased when a preload had been applied compared to without a preload. While not statistically significant, an increase in blood volume was seen within the putative tumor region (predominantly non-enhancing lesion) for the majority of High-FA patients. The elevated blood volume we observed from Pre+ data is in agreement with previous research suggesting that DSC without preload correction systematically underestimates true rCBV [11].

This within-patient increase in blood volume from Pre+ data was observed for estimates calculated with leakage-correction and non-parametric, model-free post-processing analysis. This finding is also in agreement with recent research from Boxerman et al. [19], which investigated the interplay between preload and post-processing leakage correction of High-FA data and showed that the combination of both techniques may have complementary correction effects depending on the tumor subtype. Our data presented here also shows blood volume from High-FA DSC is sensitive to the addition of a preload, the addition of post-processing correction, and the combination of these correction strategies. Taken together, these results suggest that attention must be paid to the leakage-correction strategies employed for High-FA data, as blood volume estimates are significantly influenced by presence of a gadolinium preload.

However, blood volume estimates from DSC acquired with Low-FA were not significantly influenced by the addition of a preload. Unlike the High-FA patients, blood volume estimates from patients in the Low-FA group did not significantly change between Pre- and Pre+ data acquisitions. The blood volume estimates within the NAWM of these patients remained highly stable with all seven patients showing a magnitude of voxel-wise change of less than 7%. When this was investigated on a voxel-wise basis, we found that patients in the Low-FA had significantly less percentage change between preload conditions than the patients in the High-FA. The blood volume estimates of patients in the Low-FA group were much less sensitive to the presence of a preload than

patients in the High-FA group. For Low-FA patients, the average voxel-wise change between Pre- and Pre+ blood volume ranged from -1.5% to 6.6% in tumor and -1.7% to 1.6% in NAWM (depending on post-processing method), whereas for High-FA patients it ranged from 7.2% to 20.0% in tumor and 6.5% to 16.6% in NAWM. This further supports that the addition of a preload greatly alters high-FA data, while low-FA data remains stable.

In addition to the relatively small sample size, one potential limitation of this study is the heterogeneity in patient history and glioma grade of the patients we studied. We would expect that prior treatment with antiangiogenic therapy may alter the blood volume and vessel permeability, thus influencing the preload effect. To address this, we chose to draw a within-patient comparison so as to minimize the effect of prior treatment history. We would also expect that the degree to which the addition of a preload influences resultant blood-volume would be dependent on grade, as high-grade, enhancing tumors would have greater contrast agent extravasation. The heterogeneity in the T2-lesions within this patient set is a probable explanation as to why the increase in blood volume observed within the T2-lesion did not reach statistical significance, whereas the change within the NAWM, a more comparable region between patients, did.

Finally, in practice the dose of the contrast bolus, whether or not a preload is also administered, will likely be larger than the .05 mmol/kg used in this study. The .05 mmol/kg bolus for both injections in this study was chosen so as to not increase the total

dose to patients beyond that of a standard, single-injection protocol. Greater dose of contrast bolus will likely improve SNR beyond that of this study. Since the presence of a preload did not significantly alter the blood volume estimates from Low-FA data, it would follow to use the full 0.1 mmol/kg dose for the contrast bolus to achieve improved SNR.

In conclusion, this study provides support for Low-FA (35°) DSC as an acquisition method for assessing blood volume in glioma patients in the clinical setting as these estimates both (1) remain stable across preload conditions; and (2) have previously been shown to be predictive of clinically-relevant vascular features [Chapter 3, [18]. Blood volume estimates calculated from Low-FA DSC data were similar whether acquired with or without a preload, whereas blood volume estimates calculated from High-FA (90°) DSC data significantly increased when a preload had been applied. The results of this study are in agreement with previous work showing significant underestimation of blood volume calculated from DSC acquired without a preload and at high FA. Further, this study offers that Low-FA DSC may be a more stable, and thus more comparable, acquisition strategy as the influence of preload was minimal. Low-FA DSC acquired with a single, standard dose of gadolinium may be a well-suited perfusion acquisition strategy for the clinic as it does not require the addition of a preload, thus limiting risks associated with gadolinium exposure to patients.

4.5 References:

1.   Weisskoff, R.M., et al., *Microscopic susceptibility variation and transverse relaxation: theory and experiment.* Magn Reson Med, 1994. **31**(6): p. 601-10.

2.   Knopp, E.A., et al., *Glial neoplasms: dynamic contrast-enhanced T2*-weighted MR imaging.* Radiology, 1999. **211**(3): p. 791-8.

3.   Lupo, J.M., et al., *Dynamic susceptibility-weighted perfusion imaging of high-grade gliomas: characterization of spatial heterogeneity.* AJNR Am J Neuroradiol, 2005. **26**(6): p. 1446-54.

4.   Maeda, M., et al., *Tumor vascularity in the brain: evaluation with dynamic susceptibility-contrast MR imaging.* Radiology, 1993. **189**(1): p. 233-8.

5.   Cha, S., *Perfusion MR imaging of brain tumors.* Top Magn Reson Imaging, 2004. **15**(5): p. 279-89.

6.   Kong, D.S., et al., *Diagnostic dilemma of pseudoprogression in the treatment of newly diagnosed glioblastomas: the role of assessing relative cerebral blood flow volume and oxygen-6-methylguanine-DNA methyltransferase promoter methylation status.* AJNR Am J Neuroradiol, 2011. **32**(2): p. 382-7.

7.   Paulson, E.S. and K.M. Schmainda, *Comparison of dynamic susceptibility-weighted contrast-enhanced MR methods: recommendations for measuring relative cerebral blood volume in brain tumors.* Radiology, 2008. **249**(2): p. 601-13.

8.   Uematsu, H. and M. Maeda, *Double-echo perfusion-weighted MR imaging: basic concepts and application in brain tumors for the assessment of tumor blood volume and vascular permeability.* Eur Radiol, 2006. **16**(1): p. 180-6.

9.   Heiland, S., et al., *Simultaneous assessment of cerebral hemodynamics and contrast agent uptake in lesions with disrupted blood-brain-barrier.* Magn Reson Imaging, 1999. **17**(1): p. 21-7.

10.   Gahramanov, S., et al., *Improved perfusion MR imaging assessment of intracerebral tumor blood volume and antiangiogenic therapy efficacy in a rat model with ferumoxytol.* Radiology, 2011. **261**(3): p. 796-804.

11.   Boxerman, J.L., K.M. Schmainda, and R.M. Weisskoff, *Relative cerebral blood volume maps corrected for contrast agent extravasation significantly correlate*

with glioma tumor grade, whereas uncorrected maps do not. AJNR Am J Neuroradiol, 2006. **27**(4): p. 859-67.

12.   Hu, L.S., et al., *Optimized preload leakage-correction methods to improve the diagnostic accuracy of dynamic susceptibility-weighted contrast-enhanced perfusion MR imaging in posttreatment gliomas.* AJNR Am J Neuroradiol, 2010. **31**(1): p. 40-8.

13.   Juluru, K., et al., *MR imaging in patients at risk for developing nephrogenic systemic fibrosis: protocols, practices, and imaging techniques to maximize patient safety.* Radiographics, 2009. **29**(1): p. 9-22.

14.   Saraswathy, S., et al., *Evaluation of MR markers that predict survival in patients with newly diagnosed GBM prior to adjuvant therapy.* J Neurooncol, 2009. **91**(1): p. 69-81.

15.   Weisskoff, R.M., Boxerman J. L., Sorensen A. G., Kulke S. M., Campbell T. A., Rosen B. R., *Simultaneous blood volume and permeability mapping using a single Gd-based contrast injection.* In: Proceedings of the Second Meeting of the Society of Magnetic Resonance., 1994. **Berkeley, CA**(279).

16.   Cha, S., et al., *Differentiation of glioblastoma multiforme and single brain metastasis by peak height and percentage of signal intensity recovery derived from dynamic susceptibility-weighted contrast-enhanced perfusion MR imaging.* AJNR Am J Neuroradiol, 2007. **28**(6): p. 1078-84.

17.   Crawford, F.W., et al., *Relationship of pre-surgery metabolic and physiological MR imaging parameters to survival for patients with untreated GBM.* J Neurooncol, 2009. **91**(3): p. 337-51.

18.   Essock-Burns, E., et al., *Assessment of perfusion MRI-derived parameters in evaluating and predicting response to antiangiogenic therapy in patients with newly diagnosed glioblastoma.* Neuro Oncol, 2011. **13**(1): p. 119-31.

19.   Boxerman, J.L., et al., *The Role of Preload and Leakage Correction in Gadolinium-Based Cerebral Blood Volume Estimation Determined by Comparison with MION as a Criterion Standard.* AJNR Am J Neuroradiol, 2012.

CHAPTER 5 : Assessment of Perfusion MRI Derived Parameters in Evaluating and Predicting Response to Anti-Angiogenic Therapy in Patients with Newly-Diagnosed GBM

In this project, we investigated the use of parametric maps derived from DSC imaging to evaluate response to enzastaurin, an antiangiogenic therapeutic, in the upfront treatment setting for patients with GBM. We assessed DSC perfusion parameters as a predictors of response in the context of classic Macdonald-criteria progression-free survival as well as an assessment of durable radiographic response. This work provides evidence to support the use of DSC-MRI data as a tool to identify likely responders and as an early biomarker of response in the antiangiogenic setting.

5.1 Abstract:

The paradigm for treating patients with glioblastoma multiforme (GBM) is shifting from a purely cytotoxic approach to one that incorporates anti-angiogenic agents. These are thought to normalize the tumor vasculature and have shown improved disease management in patients with recurrent disease. How this vascular remodeling evolves during the full course of therapy for patients with newly-diagnosed GBM and how it relates to radiographic response and outcome remains unclear. In this study we examined 35 patients who are newly-diagnosed with GBM using Dynamic Susceptibility Contrast (DSC) MR Imaging in order to identify early predictors of radiographic response to anti-angiogenic therapy and to evaluate changes in perfusion parameters that may be predictive of progression. After surgical resection, patients received enzastaurin and temozolomide both concurrent and adjuvant to radiotherapy. Perfusion parameters, peak height and percent recovery, were calculated from the dynamic curves to assess vascular density and leakage. Six-month radiographic responders showed significant improvement in percent recovery between baseline and 2-months into therapy, while 6-month radiographic non-responders showed significantly increased peak height between baseline and 1-month. At 2-months into therapy, percent recovery was predictive of progression-free survival. Four months prior to progression there was a significant increase in the standard deviation of percent recovery within the tumor region. DSC perfusion imaging provides valuable information about vascular remodeling during anti-angiogenic therapy, which may aid clinicians in identifying patients who will respond at the pre-therapy scan and as an early indicator of response to anti-angiogenic therapy.

5.2 Introduction:

Glioblastoma multiforme (GBM) is the most malignant subtype of glioma and is characterized by extreme heterogeneity, extensive neovasculature, and active angiogenesis. The current standard of care for patients with newly-diagnosed GBM includes combined radio- and chemotherapy, which comprises a six-week cycle of external beam radiation therapy and oral temozolomide followed by an additional six months of temozolomide [1, 2]. Anti-angiogenic therapies have recently shown the potential for reducing tumor size and increasing 6-month progression-free survival [3, 4]. The recent phase II trial of the anti-angiogenic agent bevacizumab, a monoclonal antibody directed against vascular endothelial growth factor (VEGF), used alone and in combination with irinotecan reported dramatic improvement in 6-month progression-free survival and a high response rate in patients with recurrent GBM [5]. It has been proposed that the use of adjuvant anti-angiogenic therapy in combination with standard radio- and chemotherapy acts to normalize the tortuous tumor vasculature and improve delivery of chemotherapeutics and oxygen [6, 7]. Enzastaurin (LY317615) is one such anti-angiogenic agent that is currently under investigation for its potential as an adjuvant therapy for patients with newly-diagnosed GBM [8].

Enzastaurin selectively inhibits protein kinase Cb and has been reported to have both direct antitumor effects, through suppression of tumor cell proliferation and induced apoptosis, and indirect effects, through inhibition of tumor induced angiogenesis [9]. Unlike bevacizumab, enzastaurin is a non-VEGF anti-angiogenic agent whose mechanism of action is not yet fully understood [10]. Preclinical reports have shown that

the combination of enzastaurin and radiation are synergistic in terms of the induction of apoptosis in glioma models [11]. One of the first multi-center phase II clinical studies of enzastaurin was reported by Robertson et al in 2007 who described a favorable toxicity profile and single-agent activity in a population of fifty-five patients with refractory diffuse large B-cell lymphoma [12]. The authors highlight the possibility of differential sensitivity to enzastaurin based upon a small subset of the study population who showed long-term response but showed similar steady-state drug levels as the rest of the population. In the recurrent GBM population, enzastaurin has not been shown to have superior efficacy compared with the cytotoxic chemotherapeutic agent lomustine [13], yet there are several ongoing phase I/II trials that involve the use of adjuvant enzastaurin for patients newly-diagnosed with GBM [8, 14].

The exciting potential of adjuvant anti-angiogenic therapy for improving disease management and increasing progression-free survival, has simultaneously highlighted unresolved questions in the field regarding the evaluation of response. As described in van den Bent et al [15], there are numerous challenges in evaluating response to anti-angiogenic therapies in neuro-oncology. Classic Macdonald criteria [16] have used reduction in contrast enhancing volume as a surrogate marker for antitumor effects. For anti-angiogenic therapies, the apparent reduction in enhancing volume could be due to the transient normalization of the blood-brain barrier rather than antitumor activity [17, 18]. This complicates the definition of progression and the use of six-month progression-free survival as a surrogate endpoint of overall survival. As the paradigm for GBM therapy shifts from a purely cytotoxic approach to now incorporating targeted therapies

with cytostatic effects, there is a need to explore the use of functional imaging techniques in order to better evaluate and define new criteria for evaluating response to therapy.

A number of non-invasive imaging techniques have been used to assess changes in microvasculature and response to therapy [19-21]. Dynamic susceptibility-weighted contrast (DSC) MR imaging has been shown to improve sensitivity compared to conventional MR imaging alone in determining glioma grade [22]. Within the context of anti-angiogenic therapy, Batchelor et al used both DSC and dynamic contrast-enhanced (DCE) MR imaging, with a variety of other advanced imaging techniques, to evaluate the normalization of vasculature in recurrent GBM patients receiving adjuvant AZD2171 during the first 112 days of therapy [3]. The authors observed rapid functional vascular normalization both in terms of a reduction in vessel size and overall permeability, which was found to be reversible upon drug "holiday." The changes in DSC and DCE imaging derived perfusion parameters combined with differences in circulating collagen IV levels between pre-therapy and one day post-therapy were combined to create a "vascular normalization index" which was predictive of overall survival and progression-free survival for patients with recurrent GBM who received this therapy [23]. How these parameters evolve during the full course of therapy for patients with newly-diagnosed GBM and how they relate to radiographic response and outcome remains unknown.

The previous work with DSC perfusion MRI has made it an alluring technique for evaluating response to anti-angiogenic therapy. There is the potential for addressing

challenges specific to assessing the efficacy of anti-angiogenic agents in clinical trials including; (1) the identification of subpopulations that would benefit most from this therapy and (2) the recognition of early markers of progressive disease in the case of tumor recurrence [17]. The present study was designed to investigate the use of DSC perfusion MR imaging to identify early predictors of overall response to anti-angiogenic therapy as well as to evaluate distinct changes in MR parameters during therapy that may be predictive of imminent progression.

5.2 Materials and Methods

Patient Population:

Thirty-five patients who were newly-diagnosed with grade IV glioblastoma multiforme based on the world health organization (WHO) criteria were recruited for this study. Patients received surgical resection and were treated with a standard six-week cycle of external beam radiation therapy (XRT). In addition to radiotherapy, patients were also administered a chemotherapy regimen that included temozolomide (75 mg/m^2 daily during radiotherapy and 200 mg/m^2 for five days every 28-day cycle after radiotherapy) and enzastaurin (250 mg daily) concurrent and adjuvant to radiation therapy. Patient age ranged from 25 to 70 with a median age of 57. Patients were required to have a Karnofsky Performance Score (KPS) of ≥60 in order to be enrolled in the study. Patients who went off therapy due to side effects were excluded from the study population. All patients provided informed consent in accordance with guidelines established by the Committee on Human Research at our institution.

Imaging:

MR exams were performed on a 3T GE EXCITE scanner (GE Healthcare Technologies, Milwaukee, WI) with an 8-channel phased array receive coil. Patients were imaged prior to beginning therapy (post-surgical resection) and then serially at 1, 2, 4, 6, 8, 10, and 12 months after beginning therapy. If a patient progressed, their subsequent scans were no longer included in this study.

Conventional MR and MRSI:

The MRI examination included pre- and post-gadolinium T1-weighted three-dimensional spoiled gradient echo (SPGR) with inversion recovery (TR = 8.86 msec, TE = 2.50 msec, matrix = 256 x 256, slice thickness = 1.5 mm, FOV = 24 x 24 cm, TI = 400ms, flip angle =15˚) and T2-weighted FLAIR (TR = 150 msec, TE= 2.1 msec, TI= 2.38 sec, matrix = 256 x 192, slice thickness = 3 mm, FOV = 24 x 24 cm) imaging. Patients also received lactate-edited 3-D MR spectroscopy with PRESS localization and VSS pulses around an excited volume of approximately 80x80x40 mm^3 (TR = 1104 msec, TE = 144 msec, FOV = 16 x 16 x16 cm, nominal voxel size=1x1x1 cm, 712 dwell points, 988 Hz sweepwidth) [24]. After each examination the images were transferred to a SUN Ultra 10 workstation (Sun Microsystems, Mountain View, CA) for post-

processing. The pre-gadolinium SPGR, FLAIR, and MRSI images were aligned to the post-gadolinium SPGR images for each scan date [25].

Perfusion-weighted Imaging:

In addition to anatomic and metabolic imaging, patients received DSC imaging, as summarized in **Table 3.1**. Perfusion imaging was performed during the injection of gadolinium chelate contrast (Magnevist®, Bayer Healthcare). A bolus injection of 0.1 mmol/kg contrast agent was administered at 3 ml/sec using a power injector. A gradient-echo echo-planar sequence (TR= 1500 msec, TE = 54 msec, matrix = 128 x 128, FOV = 24 x 24 cm^2, slice thickness = 4 mm, flip angle = 35˚) was acquired for 2:00 min for a total of 80 time points.

Image Processing:

The T2* signal-intensity time curves acquired during the first pass of the gadolinium bolus were converted to change in relaxation rate (ΔR2*) and resampled to match the spatial resolution of the anatomic image series. Two parameters were derived from these curves: *peak height*, the maximum increase in relaxivity reflective of greatest gadolinium influx and a physiological estimate of vascular density; and *percent recovery*, the relative return to baseline of the curve reflective of bolus passed through the voxel

and a physiological estimate of leakage. A schematic representation of these parameters on the susceptibility curve is illustrated in **Figure 5.1**. These summary parameters were chosen in lieu of relative cerebral blood volume and leakage factor, which can also be derived from the susceptibility curve, as they have been shown to be proportional to each other for the data acquisition parameters used in this study but do not require extensive curve fitting [26]. DSC images were nonrigidly aligned to the pre-contrast SPGR image using a B-spline warping by maximization of normalized mutual information [27]. The peak height value was normalized to the mean value within the normal appearing white matter, which was segmented from the pre-contrast SPGR images by applying a hidden Markov random field model with an expectation–maximization algorithm [28].

Figure 5.1: Summary parameters of susceptibility curve.
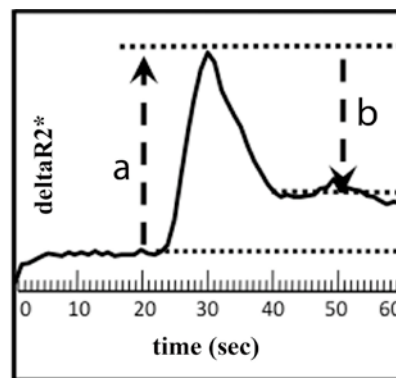
Figure 5.1: Peak Height, equal to the distance (a), is the maximum increase in relaxivity and is a physiologic estimate of vascular density. Percent Recovery, equal to [the distance (b) ÷ the distance (a)] × 100, is the relative return to baseline of the susceptibility curve and is a physiologic estimate of leakage.

Definition of Putative Tumor Region:

The region of risk was identified using both the anatomic and metabolic imaging (5.2). The contrast enhancing lesion (CEL) was defined on the post-gadolinium T1-weighted image and the T2 hyperintense region (T2All) was defined on the T2 FLAIR image using a semi-automatic segmentation algorithm [29] (**Figure 5.2.a**; left, middle). A board certified radiologist approved all regions of interest. The region of abnormally elevated Choline-to-NAA index (CNI>2) [30] was defined on the MRSI image (CNI-mask) (**Figure 5.2.a**; right). The putative tumor region was defined as including these three abnormality masks (CEL, T2all, and CNI-mask) and excluding the resection cavity, cerebral-spinal fluid, and necrotic regions (**Figure 5.2.b**).

Figure 5.2: Definition of putative tumor region.
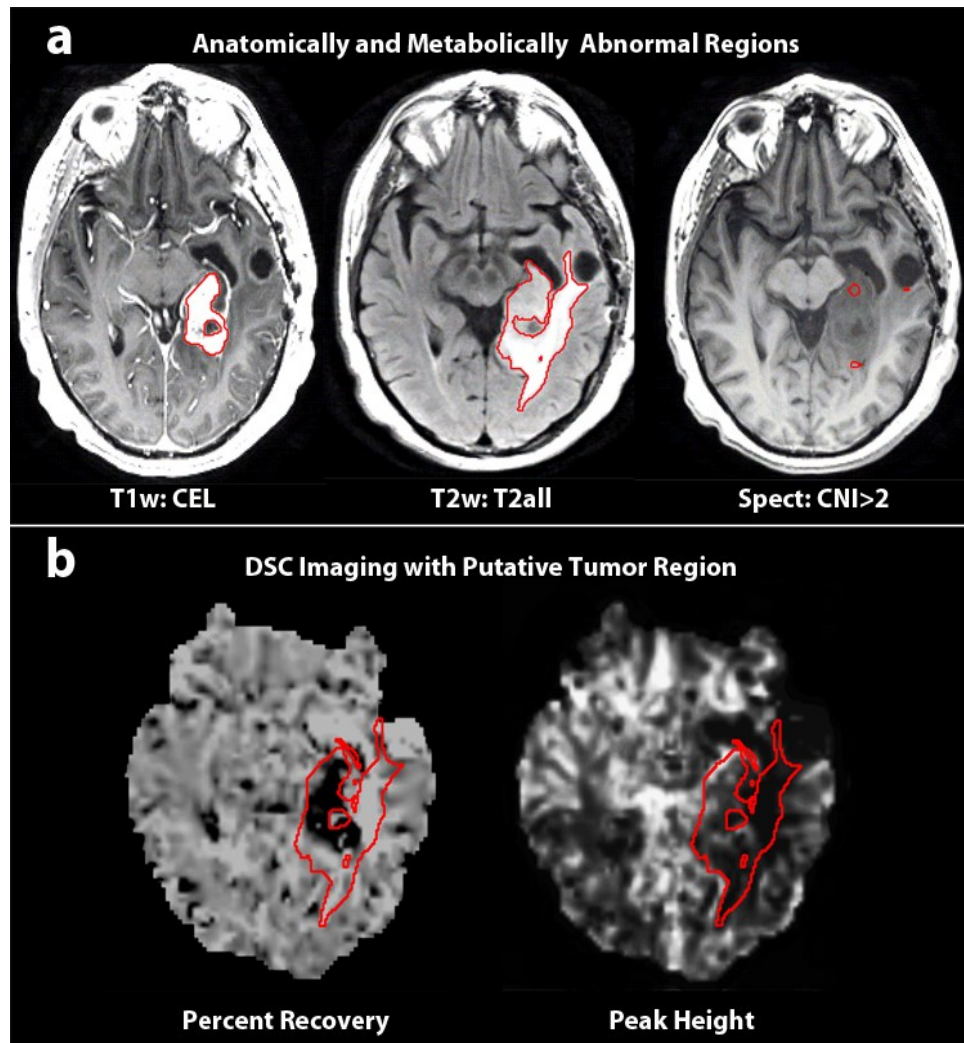
Figure 5.2: (a) Anatomically and metabolically abnormal regions were combined to define the putative tumor region, which was overlaid on both the percent recovery and peak height parametric maps (b).

Data Analysis/Statistical Considerations:

The putative tumor region mask was overlaid on the parametric maps derived from the DSC perfusion weighted imaging techniques (**Figure 5.2.b**). Two measures of abnormality were extracted from each of the parametric maps within the putative tumor region: the *intensity* and the *heterogeneity* of the perfusion parameter value. The intensity of the most extreme portion of the abnormality for the vascular density parametric maps was defined as the 90th percentile value of the DSC-derived peak height corresponding to elevated vascularization. For the permeability parametric maps, intensity was defined as the 25th percentile DSC-derived percent recovery corresponding to elevated permeability. The perfusion heterogeneity was defined as the standard deviation of the perfusion parameter value within the putative tumor region reflective of the variation in extent of vascularization or permeability on the respective parametric map. The Logrank test was used to compare progression-free survival (PFS) and overall survival (OS) among response groups. PFS was defined as the time from the patient's baseline scan to the scan date of clinical progression or, in the case of no progression, patient's were censored at the date of last contact. To address the potential for pseudo-progression, the clinical history of all patients that progressed within 12 weeks of the completion of radiotherapy, as well as all patients with a suspect scan followed by stable disease, were centrally re-reviewed by a neuro-oncologist. Notation was made regarding re-operation and location of recurrence to confirm true progression in accordance with the recommendations set forth by Wen et al. [31]. The Wilcoxon rank-sum test was used to test for differences in imaging parameters between response groups at early time points and the Wilcoxon sign-rank test was used to test for within group change between early time points. Univariate

and multivariate nonparametric Cox regression analysis was used to evaluate which parameters were predictive of PFS or OS (landmarked from scan date of perfusion covariate). Clinical control factors of baseline KPS, age, gender, and extent of resection (the few cases of biopsy were collapsed with subtotal resection) were included in this analysis. Due to the exploratory nature of the study, no formal adjustment of type I error was undertaken; in all cases, $p < 0.05$ was considered statistically significant.

Definition of Radiographic Response:

Patients were divided into four radiographic response categories based on the assessment made by an experienced board certified radiologist at two different time points (6 months and 12 months). A flow-chart illustrating this decision-tree process is displayed in **Figure 5.3**. The assessments were done blinded to the patients' perfusion data.

Figure 5.3: Radiographic response categories schema.
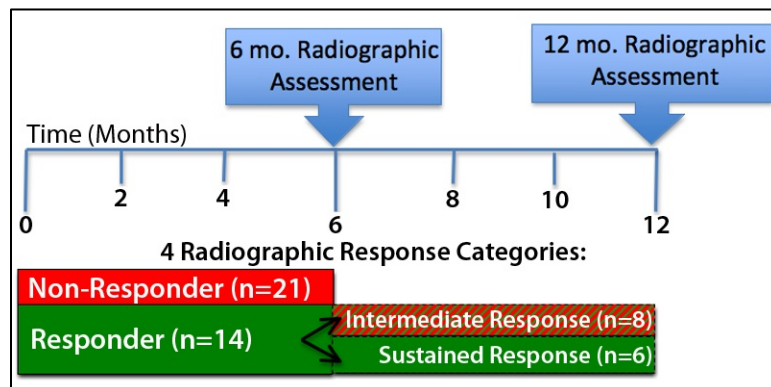
6 Month Radiographic Assessment: The radiologist reviewed the series of anatomic images from each patient up to this time-point to determine the changes in contrast enhancement from the baseline scan. Patients with decreased enhancement were classified as *6-Month Radiographic Responders* (n=14). Patients with increased (n=18) or no change (n=3) in enhancement were classified as *6-Month Radiographic Non-Responders* (n=21). **Figure 5.4.a** shows a characteristic example of a 6-Month Radiographic Non-Responder (top) and 6-Month Radiographic Responder (middle, bottom). Note the obvious increase in the CEL of the Non-Responder and decrease in the CEL of the Responders.

12 Month Radiographic Assessment: In order to capture the durability of the response for the 14 patients who were classified as *6-Month Radiographic Responders,* a second assessment was performed 12 months after the beginning of radiation. Patients who showed an obvious resurgence of contrast enhancement were classified as having a *12-month Intermediate-Response* (n=8) and patients who continued to show a decrease or no change in the enhancement were classified as having a *12-month Sustained-Response* (n=6). **Figure 5.4.b** shows examples of two of these patients, one where the observed response is transient (middle) and the other where the observed response was sustained (bottom).

This classification allowed the data to be analyzed in terms of patients who showed no short term radiographic response; those who showed an intermediate radiographic response; and those that showed a sustained radiographic response during the one-year of follow-up imaging. The rationale for doing both 6-month and 12-month assessment is two-fold. Firstly it reduces the risk of mistakenly capturing a pseudo-progression event because the radiographic pattern is assessed at two discrete standard clinical time-points. Secondly, by delineating between intermediate and sustained response, it allows the identification of imaging characteristics associated with patients who benefit the most from therapy.

Figure 5.4: Radiographic response assessment.
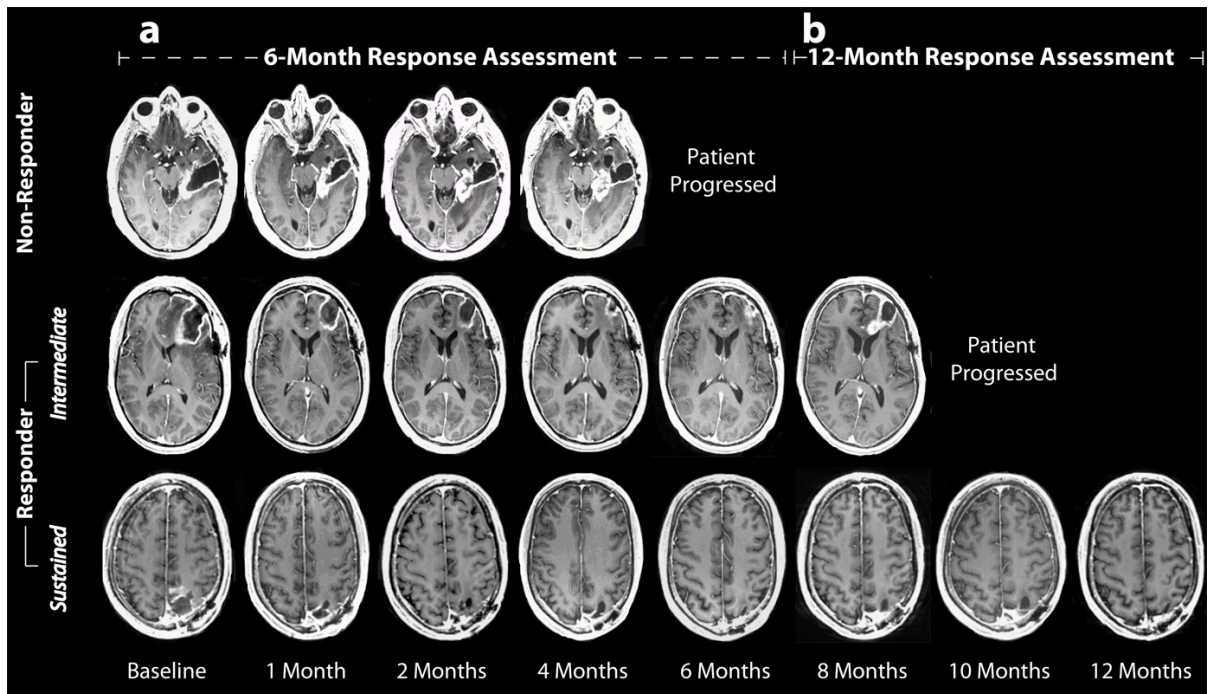
Figure 5.4: T1w post-gadolinium serial images of three exemplar patients of each of the response categories. 6-month Non-responders (top) had a significant increase in contrast enhancement (CE) within the 6-month assessment (a), while 6-month Responders (middle, bottom) did not. Those patients that responded during the 6-month assessment showed two distinct patterns of CE upon the further 12-month assessment (b). Patients with a 12-month Intermediate-Response had a dramatic resurgence of CE (middle) while patients with a 12-month Sustained-Response did not (bottom).

5.3 Results:

A total of 145 patient scans were collected with an average of 18 patient scans per time point (**Table 5.1**). Kaplan-Meier curves describing progression-free survival and preliminary overall survival of the thirty-five patients are displayed in **Figure 5.5**. Thirty-two of the thirty-five patients were determined by their neuro-oncologist to have evidence of progression during the length of the study. All patients that progressed within 12 weeks of the completion of radiotherapy (n=13) were confirmed to have had true progression; 11 patients had histological confirmation at resurgery, 1 patient had new CEL outside of the high-dose radiation field, and 1 patient changed therapies and quickly progressed again. Median progression-free survival (PFS) for the entire population was 30.9 weeks (95% CI: 18.4 to 41.6 weeks) and median overall survival (OS), based on 26 events, was 75.9 weeks (95% CI: 57.6 to 78.0 weeks). Median follow-up time for the censored patients at study completion was 98.9 weeks.

Table 5.1: Pattern of therapy and number of DSC patient scans acquired at each time point.

	Time (Months)								
	Baseline	1	2	4	6	8	10	12	Total
Therapy	RT+Drug	RT+Drug	RT+Drug	Drug	Drug	Drug	Drug	Drug	
DSC Scans	29	19	28	22	17	14	11	5	145

* "RT" is External Beam Radiation Therapy (60 Gy, 5 days per week for 6 weeks)

* "Drug" includes Enzastaurin (250 mg daily) and Temozolomide (75mg/m^2 daily during RT; 200mg/m^2 for 5 days every 28 days after RT)

Figure 5.5: Kaplan-Meier progression-free survival and overall survival curves for the thirty-five patients with GBM.
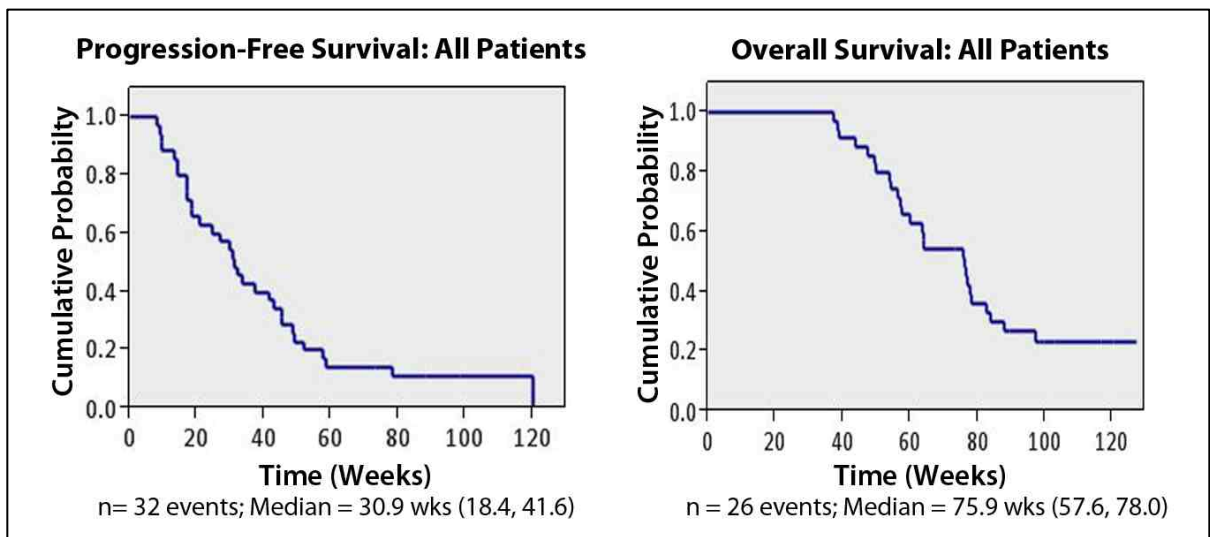
Early Differences in Perfusion Parameters among Radiographic Response Groups:

Data was analyzed from baseline pre-therapy scan through progression or furthest follow-up with a particular emphasis on identifying early predictors of response.

Peak Height – Measure of Vascularization:

Normalization of Entire Population:

The greatest change in the 90th percentile peak height (PH) across the patients occurred within the first two months of therapy (**Figure 5.6.b** top). There was a significant within-patient reduction of the 90th percentile PH and the standard deviation of PH in the putative tumor region between baseline and two months post initial therapy scans (Wilcoxon sign-rank, p=.002; p=.008). After 4 months of therapy, there were no longer any significant within-patient changes for either 90th percentile PH or standard deviation of PH between sequential bimonthly scans across the population.
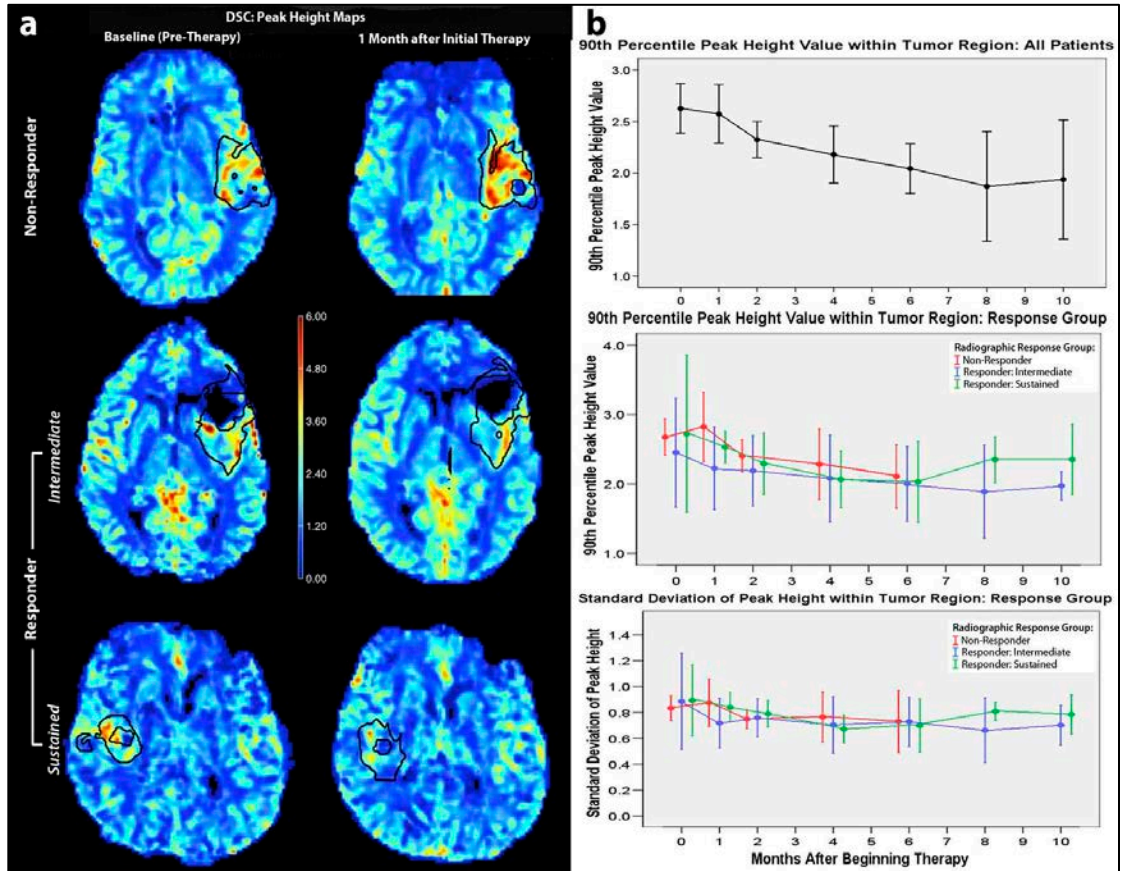
Figure 5.6: (a) Peak Height parametric maps of patient examples of each response category at baseline and 1-month into therapy. Note the increase in peak height of the 6-month Non-Responder patient (top) and the decrease in peak height of the patient with a 12-month Intermediate-Response (middle) and the patient with a 12-month Sustained-Response (bottom) within the putative tumor region (black line).

(b) Peak Height over time for entire population (top) and by response group (middle, bottom). Greatest amount of change in 90th percentile peak height occurred within the first 2 months of therapy.

Table 5.2: Summary of peak height and percent recovery data during the first two months of therapy and at progression for each response group.

	Peak Height: Mean Intensity (90th Percentile)*				
	Baseline	1-month	Δ(Baseline, 1-month)	2-months	Progression[+]
Non-Responders (n=21)	2.67± .51	2.82±.64	.20±.53	2.40±.41	2.29±.64
Responders: Intermediate (n=8)	2.45±.93	2.23±.57	-.27±.58	2.19±.60	2.30±.56
Responders: Sustained (n=6)	2.67±.62	2.53±.14	-.19±.62	2.29±.36	
All Patients (n=35)	2.63±.62	2.57±.59	-.02±.58	2.32±.46	2.29±.60

	Peak Height: Heterogeneity (Standard Deviation)*				
	Baseline	1-month	Δ(Baseline, 1-month)	2-months	Progression[+]
Non-Responders (n=21)	.83±.19	.88±.24	.06±.22	.75±.13	.76±.24
Responders: Intermediate (n=8)	.91±.43	.72±.18	-.22±.33	.76±.18	.81±.21
Responders: Sustained (n=6)	.86±.16	.84±.07	-.05±.14	.79±.08	
All Patients (n=35)	.86±.25	.82±.20	-.04±.26	.76±.13	.78±.23

	Percent Recovery: Mean Intensity (25th Percentile) *				
	Baseline	1-month	2-months	Δ(Baseline, 2-months)	Progression[+]
Non-Responders (n=21)	75.0%± 9.3	76.4%±12.4	71.8%±18.5	-2.7%±12.0	75.9%±17.9
Responders: Intermediate (n=8)	78.8%±4.5	81.3%±2.2	82.1%±4.0	3.9%±3.8	77.1%±8.3
Responders: Sustained (n=6)	76.5%±5.0	80.6%±4.2	83.7%±3.5	7.2%±7.0	
All Patients (n=35)	76.1%±7.8	78.8%±8.8	76.8%±14.7	1.0%±10.3	76.2±15.6

	Percent Recovery: Mean Heterogeneity (Standard Deviation)*				
	Baseline	1-month	2-months	Δ(Baseline, 2-months)	Progression[+]
Non-Responders (n=21)	9.4%±2.6	9.2%±3.7	12.7%±5.8	3.1%±5.1	11.1%±5.7
Responders: Intermediate (n=8)	10.8%±3.1	8.7%±1.8	10.3%±3.3	-.9%±4.1	12.0%±4.8
Responders: Sustained (n=6)	10.8%±4.0	9.30%±2.8	10.3%±3.5	-.6%±6.6	
All Patients (n=35)	10.0%±3.0	9.2%±2.9	11.6±4.88	1.3%±5.3	11.3%±5.4

*Mean computed across all patients in group

[+] Includes only patients that had progressed so was analyzed by 6-month Radiographic Response Group

Radiographic Response Assessment:

Within the first two months of anti-angiogenic drug administration, there was a significant reduction in the 90th percentile PH between the 1-month (during RT) and 2-month scans (Wilcoxon sign-rank, p=.008), but not between the baseline and 1-month scans. However, this lack of significance is explained by distinct differences within the radiographic response groups as summarized in **Table 5.2.**

Figure 5.6.a shows the PH parametric map from a 6-month Non-Responder patient, as well as examples of responder patients with either a 12-month Intermediate-Response or Sustained-Response, at baseline and 1-month into therapy. Both the patients with a 12-month Intermediate-Response and patients with a 12-month Sustained-Response showed a similar mean decrease between the baseline and 1 month scans, -.19±.63 and -.27±.58 respectively, while 6-month Non-Responders showed a mean increase of .21±.57 (**Table 5.2.a**). While the amount of change was not significantly different between response groups, it did have implications for PFS, which is discussed within the context of progression predictors.

The initial vascularization varied for the various response groups. 6-month Non-Responders and patients with a 12-month Sustained-Response had similar baseline vascularization (90th percentile PH of 2.68±.51 and 2.67±.62), while patients with a 12-

month Intermediate-Response were initially lower (2.45±.93; **Table 5.2.a**) and after the first month of therapy were significantly reduced compared with the rest of the population (2.23±.57; **Table 5.2.a**, Wilcoxon rank-sum, p<.03). The reduced 90th percentile PH value can also be seen in the patient example with 12-month Intermediate-Response in **Figure 6.a** (middle) compared to the 6-month Non-Responder (top) and 12-month Sustained-Response patient (bottom) examples.

Percent Recovery – Measure of Vascular Permeability:

Normalization of Entire Population:

Unlike PH, the percent recovery parameter was not found to have a specific time period during which there were significant within-patient changes for the entire population. Rather, by as early as 2 months after the initial therapy significant differences had begun to emerge in both the value and heterogeneity of the recovery within the putative tumor region between response groups.

Radiographic Response Assessment:

Figure 5.7.a displays the parametric maps of percent recovery at 2-months post initial therapy for one 6-month Non-Responder patient and two 6-month Responder

patients with either a 12-month Intermediate- or Sustained-Response. Significant differences were found at 2-months post initial therapy among the 6-month response groups, as described below. Note the reduced recovery and increased heterogeneity throughout the putative tumor for the 6-month Non-Responder (top) compared to both of the 6-month Responders (middle, bottom).

6-month Non-Responders displayed significantly lower 25th percentile recovery (71.8% ± 18.5%) than 6-month Responders (82.7% ± 3.7%) at 2-months into therapy (Wilcoxon rank-sum, $p = .01$). The 6-month Responder group showed significant improvement in 25th percentile recovery value between the baseline and two month scan (Wilcoxon sign-rank, $p = .008$), while the 6-month Non-Responders did not show significant within-patient change (Wilcoxon sign-rank, $p = .64$). 6-month Non-Responders had instead undergone a highly variable decrease in 25th percentile Recovery value (-2.7% ± 12.5%) and a marginally significant increase in overall heterogeneity (3.1 ± 5.3; Wilcoxon sign-rank, $p = .05$) by this time point. **Table 5.2.b** shows the 25th percentile recovery and standard deviation for each of the radiographic response groups.

Figure 5.7: Percent Recovery
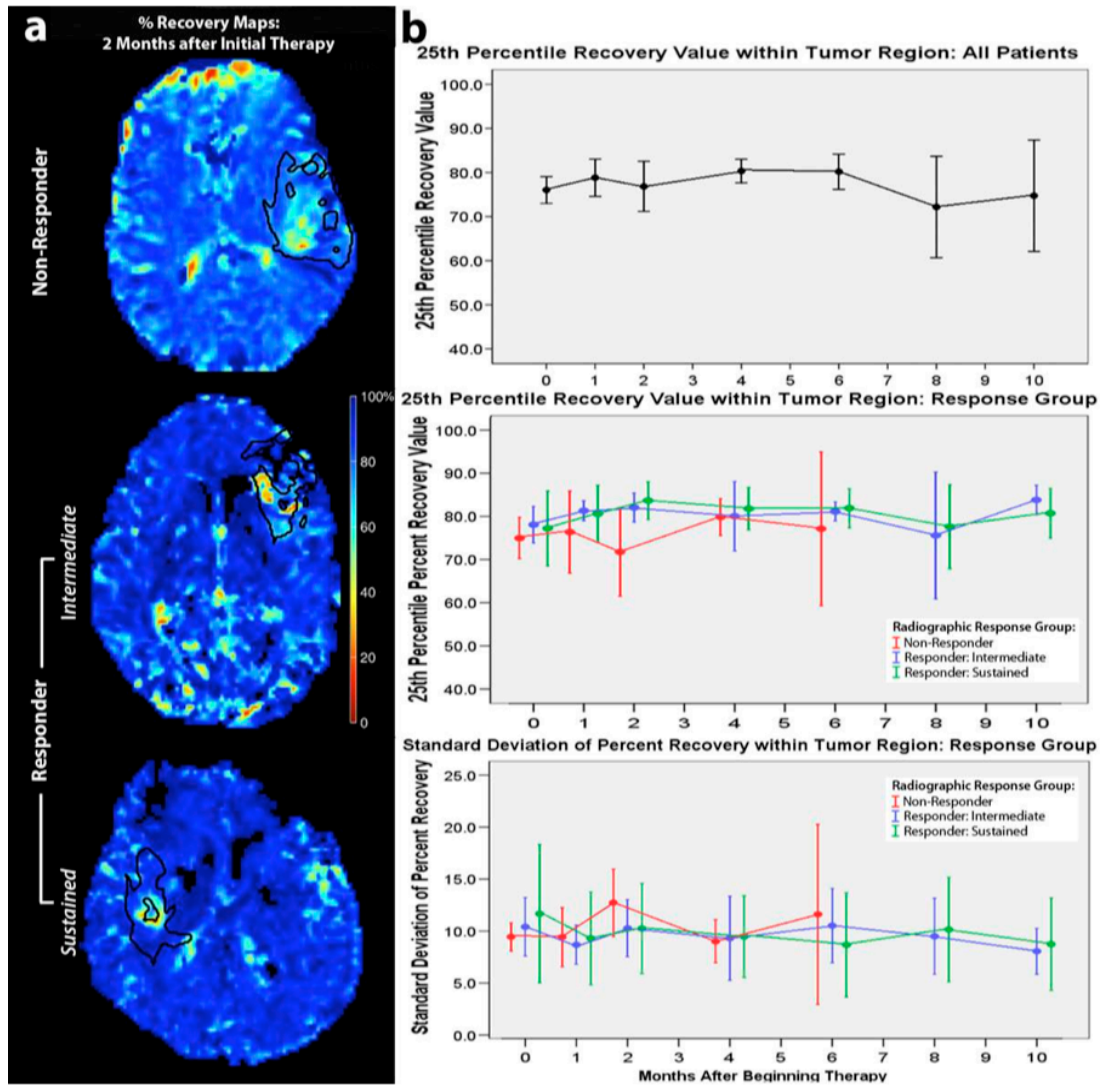
Figure 5.7: (a) Percent Recovery parametric maps of patient examples of each radiographic response category at 2-months into therapy. Note the reduced percent recovery of the 6-month Non-Responder patient (top) compared to the patient with a 12-month Intermediate-Response (middle) and patient with a 12-month Sustained-Response (bottom) within the putative tumor region (black line). The 25th percentile value within the putative tumor region was further predictive of PFS at this time point.

(b) Percent Recovery over time for entire population (top) and by response group (middle, bottom).

Early Imaging Predictors of Progression and Survival:

The data were analyzed to identify any patterns of perfusion parameters that were predictive of imminent progression and of overall survival. Of the 35 patients enrolled, 32 patients had clinically progressed and 26 patients were deceased at the time of study completion.

Progression-free Survival (PFS):

Peak Height:

An increase in 90th percentile PH value between baseline and 1-month was a risk factor for PFS adjusted for the baseline heterogeneity (standard deviation) of PH and the clinical control factors of baseline KPS, age, extent of resection, and gender (multivariate Cox regression, p = 0.02, hazard ratio = 5.408, 95% CI = [1.259, 24.420]). For every one unit increase in the change of 90th Percentile PH between baseline and 1-month (mean change = -0.02±.58), patients were at approximately a 5-fold greater risk of progression.

Percent Recovery:

Greater 25th percentile percent recovery at two months was a protective factor for

PFS, adjusting for baseline KPS, age, extent of resection, and gender (multivariate Cox

regression, p = .009, hazard ratio = .955, 95% CI = [0.926, 0.987]). For every 1%

increase in percent recovery at two-months (mean = 76.8% ± 14.7), there was

approximately a 5% reduction in risk of progression. Whereas prior to this 2-month scan,

the 25th percentile value of percent recovery at baseline and at one month was not found

to be predictive of PFS (multivariate Cox regression adjusted for clinical control factors,

p = 0.46 and 0.11, respectively). This supports the claim that by as early as two months

into therapy not only had differences in permeability emerged between response groups,

but also the extent of permeability within the tumor region was further predictive of PFS.

Changes in Parameters Prior to Progression:

The data were also examined to identify changes in the perfusion parameters on

the scans prior to patients' progression date that might be indicative of the imminent

progression. Immediately prior to progression, there were no significant changes in the

level of vascularization, both in terms of 90th percentile value and standard deviation (not

shown). However, there were interesting changes in the percent recovery parameter prior

to progression, which are displayed in **Figure 5.8.** At 4-months prior to progression the

heterogeneity of recovery values within the putative tumor region began to increase

(**Figure 5.8.a**, patient example **Figure 5.8.e**). There was a significant increase in the

standard deviation of the recovery at 4-months prior to progression over the previous (6-

months pre-progression) scan (**Figure 5.8.a**, Wilcoxon sign-rank, p < 0.04). Patients with

12-month Intermediate-Response were similar to the 6-month Non-Responders at 4-months prior to progression both in terms of the 25th percentile recovery value and overall standard deviation of recovery within the putative tumor region (**Figure 5.8.b-c**, Wilcoxon rank-sum p > 0.05). **Figure 5.8.e** shows the percent recovery parametric maps of a patient with a 12-month Intermediate-Response leading up to progression. Note the increase in the heterogeneity of percent recovery within the putative tumor region at 4-months pre-progression. This functional change can be seen on the percent recovery parametric map prior to the increase in enhancement on the T1-contrast enhanced images (**Figure 5.8.d**). The observed changes in the percent recovery map are not limited to within the contrast-enhancing lesion (**Figure 5.8.d**), but rather are throughout the broader putative tumor region (**Figure 5.8.e**). Patients had very similar percent recovery levels at progression date (**Figure 5.8.b-c**, Wilcoxon rank-sum, p > .2). At progression, the mean percent recovery value was 76.2% ± 15.6 and the mean standard deviation within the putative tumor region was 11.3% ± 5.4 for the entire population.

Figure 5.8: Percent Recovery Prior to Progression.
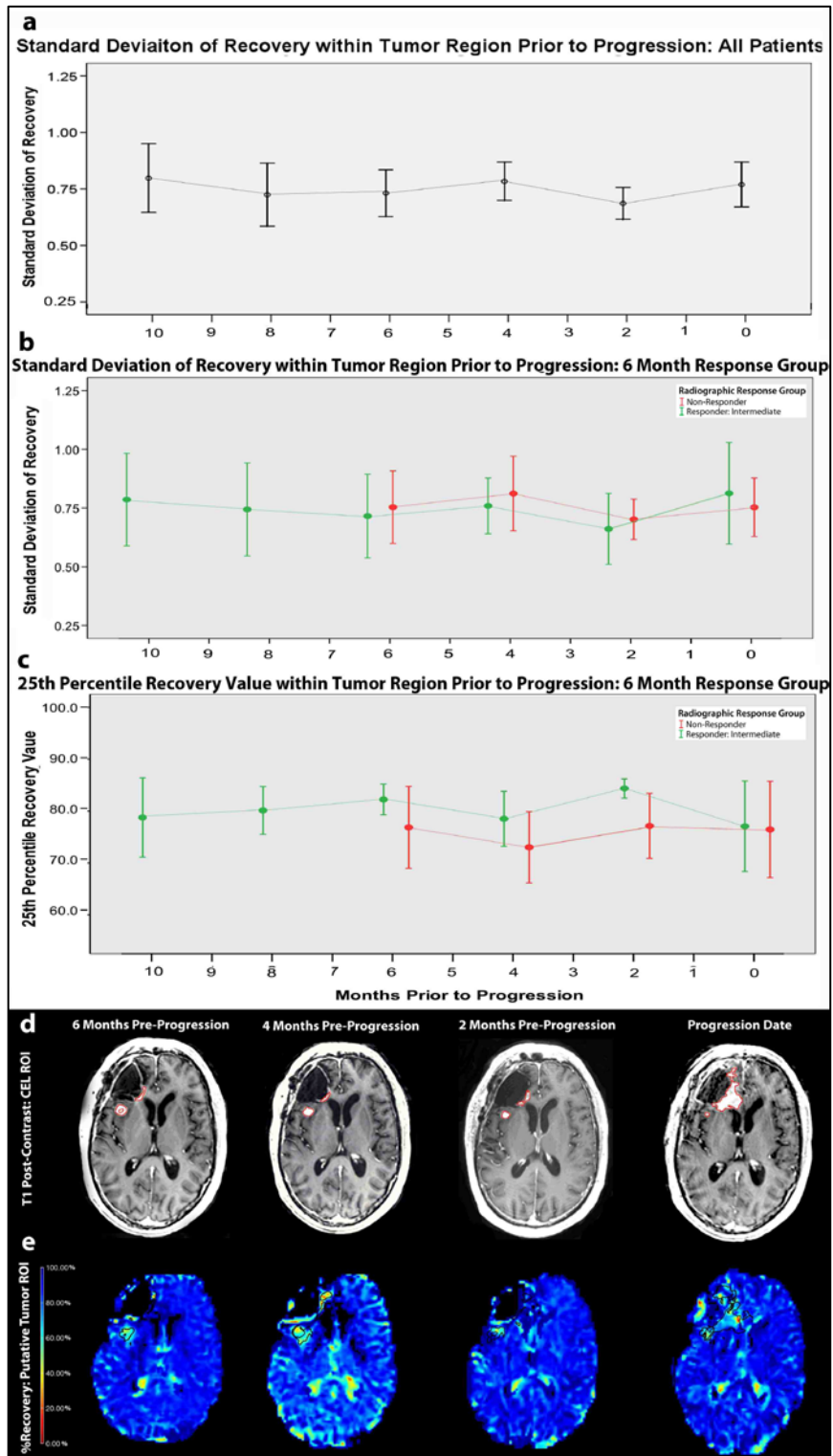
Figure 5.8: (a) Standard deviation of percent recovery within the putative tumor region increased 4 months prior to progression. (b,c) Both 6-month Non-Responders and patients with a 12-month Intermediate-Response converged as they neared progression in percent recovery intensity and heterogeneity. Note patient example showing an increase in heterogeneity of percent recovery (e) prior to the increase in CE (d).

Overall Survival:

Greater 25th percentile percent recovery at 2-months into therapy was a protective factor for overall survival, adjusted for baseline KPS, age, extent of resection, and gender (multivariate Cox regression, $p = 0.02$, HR = .957, CI = [.926, .991]). For each 1% increase in percent recovery at two-months, there was an associated 4% reduction in risk of death. Prior to the 2-month scan, percent recovery was not predictive of overall survival (multivariate Cox regression adjusted for clinical control factors, baseline $p = 0.08$ and at 1-month $p = 0.16$).

5.4 Discussion:

DSC imaging was used to identify periods of vascular remodeling during the course of anti-angiogenic therapy. Changes in the neovasculature that occurred within the first 2-months of therapy were related to both response and PFS. The marked decrease in

peak height that was observed during the first two months of therapy is consistent with the vascular normalization window that was reported by Batchelor et al [3] in 2007. They reported that the relative vessel size, as determined using a dual gradient- and spin-echo DSC sequence, reversed toward abnormal values at day 56 after initial therapy with AZD2171 and interpreted this as the end of the vascular normalization window.

When perfusion has normalized and the vasculature becomes more patent, it may be expected that intravascular gadolinium no longer leaks as readily into the extracellular extravascular space and that as a result the contrast enhancement on T1-weighted anatomical images decreases. This underlines the challenge in terms of using standard response criteria to evaluate response to anti-angiogenic therapy. The advantage of using 6- and 12-month assessments to analyze radiographic response to anti-angiogenic therapy is that they incorporate the full pattern of response rather than just the date of progression. Some patients present with a marked decrease in contrast enhancement early in therapy that is suggestive of positive response but possess a drastic return and/or growth of contrast enhancement by the 12-month assessment. Identifying which patients will have this pattern of response prior to the resurgence of enhancement would allow alternative therapies to be considered at a time point when they may be more effective. Interestingly, not all patients present in this way. Patients who show sustained response through both 6- and 12-month assessments may be interpreted as showing substantial benefit from anti-angiogenic therapy. The ability to make an early distinction between these two patterns of radiographic response may therefore be of critical clinical importance for choosing the most effective therapy.

The disadvantage of using the 6- and 12-month response assessment is that it does not provide a continuous scale on which to measure response and to test predictive hypotheses. While the use of MacDonald criteria to evaluate progression-free survival is limited in the evaluation of response to anti-angiogenic therapy [15], it does provide a scale for evaluating early biomarkers. Overall survival may be a more appropriate end-point in evaluating response to anti-angiogenic therapy, but is limited by the influence of salvage treatments [15]. The advantage in integrating the discrete 6- and 12-month radiographic assessment with the continuous PFS and OS scales is that two main challenges could be addressed (1) elucidating perfusion differences in order to identify radiographic response groups and (2) evaluating perfusion parameters during therapy that may predict outcome.

The subpopulation of patients who have a large decrease in vascular density after one month of therapy and an improvement in permeability after two months of therapy appeared to show the best response to therapy. Patients who show an increase in vascular density after one month of therapy and no improvement in permeability after two months did not respond within the first six months and thus had reduced PFS. In future prospective studies, this combination of early change in vascular density and permeability may be tracked as a biomarker of response and may ultimately aid in tailoring anti-angiogenic therapy to individual patient characteristics.

The most challenging question lies in identifying patients who display an intermediate positive response to therapy but then suddenly progress. Patients with Intermediate-Response showed a similar response pattern (decrease in vascular density after the first month and improvement in recovery after second month) as patients with Sustained-Response but had lower initial levels of vascularization. This suggests that an initially well-vascularized tumor, which improves in patency during initial therapy, is associated with better patient response. It seems that the combination of vascularization and permeability best describes the pattern of response.

Since most patients with GBM recur, it is critical to identify changes in perfusion that may be predictive of imminent progression [17]. When adjusted for the initial heterogeneity of tumor vascularization, the decrease in vascular density was predictive of PFS. This highlights interesting questions regarding the relationship between the extent and spatial distribution of tumor vascularization and the PFS of patients on anti-angiogenic therapy. The level of abnormal recovery that occurred after two-months of therapy was predictive of both PFS and OS. Four months prior to progression the heterogeneity of recovery within the putative tumor region began to increase, suggesting the end of the normalization period of the therapy for the individual patient and the beginning of reduced perfusion function. As **Figure 8.d-e** demonstrates, this change may occur prior to changes in appearance of the contrast-enhancing lesion and it will be crucial to investigate the potential of this parameter in future studies.

The observation that the entire population, regardless of radiographic response group, had similar perfusion parameters at progression is suggestive of a "progression profile". In the radiographically challenging case of patients with 12-month Intermediate-Response, perfusion parameters were similar to the 6-month Non-Responders at four months prior to progression. However, these patients remained on therapy due to the stable appearance of their contrast-enhancing lesion. Early changes in the heterogeneity of percent recovery that may precede the increase in appearance of contrast enhancement have great potential for improving the management of patients on anti-angiogenic therapy. Future prospective studies will validate these findings in a larger patient population and with other anti-angiogenic therapies.

5.5 Conclusion:

This study demonstrated changes in tumor vasculature on DSC MRI during the first two months of therapy for patients with GBM who were being treated with radiation therapy, temozolomide, and enzastaurin. Patients who had a large decrease in peak height after one month of therapy and improvement in percent recovery after two months of therapy seemed to respond best, which may aid in identifying patients who would benefit most from anti-angiogenic therapy in the future. The level of recovery present at the end of this two-month normalization window was found to be predictive of progression-free survival and overall survival. These results support the hypothesis that DSC perfusion imaging provides valuable information about changes in vascular function during therapy, which may ultimately aid clinicians in identifying patients who are likely to

respond prior to therapy and as an early indicator of patient response to anti-angiogenic

therapy.

5.6 References:

1.   Stupp R, Mason WP, van den Bent MJ, Weller M, Fisher B, Taphoorn MJ, Belanger K, Brandes AA, Marosi C, Bogdahn U, Curschmann J, Janzer RC, Ludwin SK, Gorlia T, Allgeier A, Lacombe D, Cairncross JG, Eisenhauer E, Mirimanoff RO: Radiotherapy plus concomitant and adjuvant temozolomide for glioblastoma. N Engl J Med 352: 987-996, 2005

2.   Stupp R, Hegi ME, Gilbert MR, Chakravarti A: Chemoradiotherapy in malignant glioma: standard of care and future directions. J Clin Oncol 25: 4127-4136, 2007

3.   Batchelor TT, Sorensen AG, di Tomaso E, Zhang WT, Duda DG, Cohen KS, Kozak KR, Cahill DP, Chen PJ, Zhu M, Ancukiewicz M, Mrugala MM, Plotkin S, Drappatz J, Louis DN, Ivy P, Scadden DT, Benner T, Loeffler JS, Wen PY, Jain RK: AZD2171, a pan-VEGF receptor tyrosine kinase inhibitor, normalizes tumor vasculature and alleviates edema in glioblastoma patients. Cancer Cell 11: 83-95, 2007

4.   Vredenburgh JJ, Desjardins A, Herndon JE, 2nd, Dowell JM, Reardon DA, Quinn JA, Rich JN, Sathornsumetee S, Gururangan S, Wagner M, Bigner DD, Friedman AH, Friedman HS: Phase II trial of bevacizumab and irinotecan in recurrent malignant glioma. Clin Cancer Res 13: 1253-1259, 2007

5.   Friedman HS, Prados MD, Wen PY, Mikkelsen T, Schiff D, Abrey LE, Yung WK, Paleologos N, Nicholas MK, Jensen R, Vredenburgh J, Huang J, Zheng M, Cloughesy T: Bevacizumab alone and in combination with irinotecan in recurrent glioblastoma. J Clin Oncol 27: 4733-4740, 2009

6.   Jain RK: Normalizing tumor vasculature with anti-angiogenic therapy: a new paradigm for combination therapy. Nat Med 7: 987-989, 2001

7.   Jain RK, Tong RT, Munn LL: Effect of vascular normalization by antiangiogenic therapy on interstitial hypertension, peritumor edema, and lymphatic metastasis: insights from a mathematical model. Cancer Res 67: 2729-2735, 2007

8.   Butowski N, Chang SM, Lamborn KR, Polley MY, Parvataneni R, Hristova-Kazmierski M, Musib L, Nicol SJ, Thornton DE, Prados MD: Enzastaurin plus temozolomide with radiation therapy in glioblastoma multiforme: A phase I study. [published online ahead of print Feb 17, 2010]. Neuro Oncol. doi: 10.1093/neuonc/nop070

9.   Teicher BA, Alvarez E, Menon K, Esterman MA, Considine E, Shih C, Faul MM: Antiangiogenic effects of a protein kinase Cbeta-selective small molecule. Cancer Chemother Pharmacol 49: 69-77, 2002

10.   Chen YB, LaCasce AS: Enzastaurin. Expert Opin Investig Drugs 17: 939-944, 2008

11.   Tabatabai G, Frank B, Wick A, Lemke D, von Kurthy G, Obermuller U, Heckl S, Christ G, Weller M, Wick W: Synergistic antiglioma activity of radiotherapy and enzastaurin. Ann Neurol 61: 153-161, 2007

12.   Robertson MJ, Kahl BS, Vose JM, de Vos S, Laughlin M, Flynn PJ, Rowland K, Cruz JC, Goldberg SL, Musib L, Darstein C, Enas N, Kutok JL, Aster JC, Neuberg D, Savage KJ, LaCasce A, Thornton D, Slapak CA, Shipp MA: Phase II study of enzastaurin, a protein kinase C beta inhibitor, in patients with relapsed or refractory diffuse large B-cell lymphoma. J Clin Oncol 25: 1741-1746, 2007

13.   Wick W, Puduvalli VK, Chamberlain MC, van den Bent MJ, Carpentier AF, Cher LM, Mason W, Weller M, Hong S, Musib L, Liepa AM, Thornton DE, Fine HA: Phase III study of enzastaurin compared with lomustine in the treatment of recurrent intracranial glioblastoma. [published online ahead of print Feb 4, 2010]. J Clin Oncol 28: 1168-1174. doi: 10.1200/JCO.2009.23.2595.

14.   Butowski N. A. LK, Chang S. , Hsieh E., Fedoroff A., Parvataneni R., Nicol S., Liepa A., Thornton D., Prados M.; University of California, San Francisco, San Francisco, CA; Eli Lilly, Indianapolis, IN: Phase II and pharmacogenomics study of enzastaurin plus temozolomide and radiation therapy in patients with glioblastoma multiforme or gliosarcoma. In proceedings of 2009 American Society of Clinical Oncology annual meeting Abstract No. 2020, 2009

15.   van den Bent MJ, Vogelbaum MA, Wen PY, Macdonald DR, Chang SM: End point assessment in gliomas: novel treatments limit usefulness of classical Macdonald's Criteria. J Clin Oncol 27: 2905-2908, 2009

16.   Macdonald DR, Cascino TL, Schold SC, Jr., Cairncross JG: Response criteria for phase II studies of supratentorial malignant glioma. J Clin Oncol 8: 1277-1280, 1990

17.   Chang SM, Lamborn KR, Kuhn JG, Yung WK, Gilbert MR, Wen PY, Fine HA, Mehta MP, DeAngelis LM, Lieberman FS, Cloughesy TF, Robins HI, Abrey LE, Prados MD: Neurooncology clinical trial design for targeted therapies: lessons learned from the North American Brain Tumor Consortium. Neuro Oncol 10: 631-642, 2008

18.   Wong ET, Brem S: Taming glioblastoma: targeting angiogenesis. J Clin Oncol 25: 4705-4706, 2007

19.   Fukumura D, Jain RK: Imaging angiogenesis and the microenvironment. APMIS 116: 695-715, 2008

20.   Harrer JU, Hornen S, Oertel MF, Stracke CP, Klotzsch C: Comparison of perfusion harmonic imaging and perfusion mr imaging for the assessment of microvascular characteristics in brain tumors. Ultraschall Med 29: 45-52, 2008

21.   Saraswathy S, Crawford FW, Lamborn KR, Pirzkall A, Chang S, Cha S, Nelson SJ: Evaluation of MR markers that predict survival in patients with newly diagnosed GBM prior to adjuvant therapy. J Neurooncol 91: 69-81, 2009

22.	Law M, Yang S, Wang H, Babb JS, Johnson G, Cha S, Knopp EA, Zagzag D: Glioma grading: sensitivity, specificity, and predictive values of perfusion MR imaging and proton MR spectroscopic imaging compared with conventional MR imaging. AJNR Am J Neuroradiol 24: 1989-1998, 2003

23.	Sorensen AG, Batchelor TT, Zhang WT, Chen PJ, Yeo P, Wang M, Jennings D, Wen PY, Lahdenranta J, Ancukiewicz M, di Tomaso E, Duda DG, Jain RK: A "vascular normalization index" as potential mechanistic biomarker to predict survival after a single dose of cediranib in recurrent glioblastoma patients. Cancer Res 69: 5296-5300, 2009

24.	Park I, Chen AP, Zierhut ML, Ozturk-Isik E, Vigneron DB, Nelson SJ: Implementation of 3 T Lactate-Edited 3D (1)H MR Spectroscopic Imaging with Flyback Echo-Planar Readout for Gliomas Patients. Ann Biomed Eng. [published online ahead of print July 24, 2010]. DOI: 10.1007/s10439-010-0128-x.

25.	Nelson SJ, Nalbandian AB, Proctor E, Vigneron DB: Registration of images from sequential MR studies of the brain. J Magn Reson Imaging 4: 877-883, 1994

26.	Lupo JM, Cha S, Chang SM, Nelson SJ: Dynamic susceptibility-weighted perfusion imaging of high-grade gliomas: characterization of spatial heterogeneity. AJNR Am J Neuroradiol 26: 1446-1454, 2005

27.	Rueckert D, Sonoda LI, Hayes C, Hill DL, Leach MO, Hawkes DJ: Nonrigid registration using free-form deformations: application to breast MR images. IEEE Trans Med Imaging 18: 712-721, 1999

28.	Zhang Y, Brady M, Smith S: Segmentation of brain MR images through a hidden Markov random field model and the expectation-maximization algorithm. IEEE Trans Med Imaging 20: 45-57, 2001

29.	Saraswathy SCF, Nelson S. J. : Semi-Automated Segmentation of Brain Tumor Lesions in MR Images. . In proceedings of the 14th Annual Meeting of International Soceity of Magnetic Resonance in Medicine , Seatle WA Abstract No. 1609, 2006

30.	McKnight TR, von dem Bussche MH, Vigneron DB, Lu Y, Berger MS, McDermott MW, Dillon WP, Graves EE, Pirzkall A, Nelson SJ: Histopathological validation of a three-dimensional magnetic resonance spectroscopy index as a predictor of tumor presence. J Neurosurg 97: 794-802, 2002

31.	Wen PY, Macdonald DR, Reardon DA, Cloughesy TF, Sorensen AG, Galanis E, Degroot J, Wick W, Gilbert MR, Lassman AB, Tsien C, Mikkelsen T, Wong ET, Chamberlain MC, Stupp R, Lamborn KR, Vogelbaum MA, van den Bent MJ, Chang SM: Updated response assessment criteria for high-grade gliomas: response assessment in neuro-oncology working group. [published online ahead of print March 17, 2010]. J Clin Oncol 28: 1963-1972. doi: 10.1200/JCO.2009.26.3541.

CHAPTER 6 : Patterns of Changes in Diffusion and Anatomic Imaging Parameters Vary with Treatment Regimen for Patients with Newly Diagnosed Glioblastoma

In the project described in this chapter, we investigated the effect of treatment regimen on the early changes in anatomic and diffusion parameters in patients newly diagnosed with glioblastoma. This was a collaborative project with Dr. Laleh Jalilian. My contributions included data processing, analysis of results, and editorial review. In this project, three different treatment regimens are compared (standard temozolomide (TMZ), enzastaurin with TMZ, and bevacizumab with TMZ) in conjunction with radiotherapy. Anatomic and diffusion changes were found to be therapy specific, with bevacizumab preventing the increase in edema associated with radiotherapy more effectively than enzastaurin or TMZ alone. This work provides the context for future predictive biomarker development by illustrating the early imaging changes that can be expected with these therapy regimens.

Authors:

Jalilian L, Essock-Burns E, Li Y, Cha S, Chang SM, Prados MD, Butowski NA, Nelson SJ.

6.1 Abstract:

Purpose: To compare anatomic and DWI parameters at pre-, mid-, and post-RT scans in the contrast-enhancing lesion (CEL) and non-enhancing lesion (NEL) of 99 post-surgical patients with newly diagnosed GBM who were treated with RT concurrently with either temozolomide only (TMZ alone), temozolomide and enzastaurin (TMZ+ENZA), or temozolomide and bevacizumab (TMZ+BEV).

Materials and Methods: Histograms of nADC and nFA within the CEL and NEL were generated and summary statistics calculated. Wilcoxon sign-rank and kruskal-wallis tests were used to determine changes for these parameters within each treatment arm and to evaluate differences amongst the different treatment arms at pre-, mid- and post-RT.

Results: The CEL volume decreased significantly from pre- to post-RT for patients treated with TMZ+BEV and TMZ+ENZA. The NEL volume decreased significantly from pre- to post-RT for patients treated with TMZ+BEV. The median and 10% nADC in CEL and NEL increased significantly from pre- to post-RT for patients treated with TMZ alone and patients treated with TMZ+ENZA. There was no significant change in the median and 10% nADC in the CEL and NEL from pre- to post-RT for patients treated with TMZ+BEV..

Conclusion: These quantitative results indicate that anatomic and diffusion patterns differ by treatment regimen. The diffusion pattern observed in patients treated with

143

bevacizumab supports the observation that this agent prevents the increase in edema that is associated with RT more effectively than enzastaurin or temozolomide alone.

6.2 Introduction:

Glioblastoma (GBM) is the most malignant primary malignant brain tumors in adults. The standard of care for patients with newly diagnosed GBM consists of surgery, radiotherapy and temozolomide (TMZ). Despite this multimodality treatment, the median overall survival remains around15 months [1]. GBM are highly vascularized tumors that overexpress vascular endothelial growth factor (VEGF),. This is a critical regulator of angiogenesis and neovascularization and is therefore an attractive target for therapy.. Phase II trials evaluating bevacizumab, which is an anti-VEGF antibody, either alone or in combination with irinotecan, have demonstrated an increase in 6-month PFS rates in patients with recurrent GBM when compared to historic controls [2-7]. This has resulted in anti-angiogenic therapies becoming the subject of investigation in the up front setting.

Enzastaurin is a selective protein kinase C β-inhibitor that is believed to indirectly inhibit tumor-induced angiogenesis [8] and Bevacizumab is a humanized monoclonal antibody to VEGF. The assessment of the efficacy of these agents is problematic because they directly affect the size of the CEL by reducing the permeability of the vasculature to gadolinium-based agents [9-10]. An alternative strategy is to use the new RANO (Response Assessment in Neuro-Oncology) criteria, which integrate changes in the T2 lesion into the definition of response. Although this approach is more flexible, it is still not specific for detecting tumor and there is an increasing need for alternative imaging

biomarkers to define treatment effects. A critical step in moving in this direction is to understand the degree to which anti-angiogenic agents impact anatomic and physiologic parameters compared to the current standard of care.

Diffusion weighted imaging (DWI) has been shown to detect disruption of tumor tissue architecture and identify regions of elevated cellular density by assessing random motion of water molecule protons in the extracellular space. Parameters derived from DWI include the apparent diffusion coefficient (ADC), which is a measure of the magnitude of diffusion of water molecules within the extracellular space, and the fractional anisotropy (FA), which is a measure of tissue architecture. These parameters have been proposed to be relevant for the assessment of treatment efficacy by providing an estimate of cellularity and tissue disruption within and beyond the CEL [11-13]. Radiation has been reported to cause an increase in ADC within the CEL and NEL [13], which is consistent with disruption of tissue architecture and reduction in tumor cellularity [13].

The inclusion of anti-angiogenic therapy into the standard treatment regimen has been reported to influence ADC in both a positive and negative manner, depending on the agent given and on whether patients had received previous therapy [11,14]. Obtaining a detailed understanding of how to interpret such changes would have a significant impact on clinical treatment decision-making. The purpose of this study was to evaluate and compare changes in anatomic and diffusion imaging parameters at baseline, mid-RT and post-RT scans within the CEL and NEL of post-surgical patients with newly diagnosed

GBM who were receiving TMZ alone or TMZ in combination with two different anti-angiogenic agents.

6.3 Methods:

<u>Study Population</u>

A total of 99 patients with newly diagnosed GBM (WHO Grade IV) who had received surgery and were to be treated with standard of care RT concurrently with either a) TMZ only (31 patients), b) TMZ with enzastaurin (41 patients), or c) TMZ with bevacizumab and erlotinib (27 patients) were recruited to this study. Diagnosis was based on histological examination using criteria defined by the World Health Organization (WHO). Patients were enrolled in three distinct prospective phase II clinical trials between 2005-2011, and were required to have a Karnofsky performance score (KPS) of ≥ 60. All subjects provided informed consent as approved by the Committee on Human Research at our institution. **Table 6.1** describes the characteristics of the three patient populations.

Table 6.1: Characteristics of the patients in each treatment cohort.

Treatment Population	RT + TMZ only	RT + TMZ + Enzastaurin	RT + TMZ + Bevacizumab + Erlotinib
Number of Patients	31	41	27
Median Age (range)	52 (38-77)	56 (25-80)	52 (21-76)
Male: Female Ratio	18:13	32:9	13:14
Surgery			
GTR	16	11	10
STR	13	25	13
Biopsy	2	5	4

The treatment schema for the three separate clinical trials is seen in **Figure 6.1**. Patients began treatment within 5 weeks of diagnosis with fractionated RT (total dose of 60 Gy) and 75 mg/m^2 of TMZ given daily over a period of 6 weeks. Patients receiving enzastaurin were administered the agent (250 mg daily) concurrent with the other treatments. Patients receiving bevacizumab received bevacizumab at a dose of 10 mg/kg IV every 14 days starting in week 2 of radiotherapy and received erlotinib (patients not on anti-epileptic drugs received 150 mg/day continuously and patients on anti-epileptic drugs received 500 mg/day continuously) starting on day 1 of RT.

MRI exams were performed at three time-points: (1) following surgical resection or biopsy but prior to RT (pre-RT), (2) between 3 and 5 weeks into treatment (mid-RT), and (3) within 2 weeks after completion of RT (post-RT). Patients receiving TMZ alone did not have a mid-RT scan.

Figure 6.1: Treatment Schema
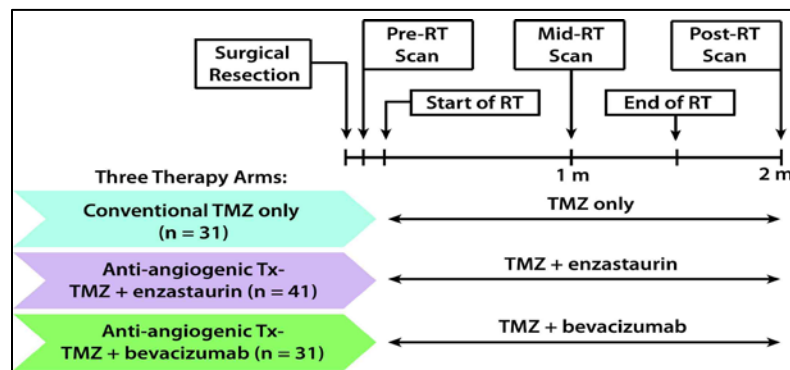
MRI Acquisition

All scans were obtained using a 3T GE MR scanner with the body coil for transmission and an 8-channel phased array coil for reception.

TMZ only Protocol: Exams included T1-weighted sagittal scout (TR/TE = 54/2 ms), axial T2-weighted fluid attenuated inversion recovery (FLAIR) (TR/TE/TI = 10002/127-157/2200 ms, matrix = 256x256x48, slice thickness = 3 mm), pre- and post-contrast T1-weighted spoiled gradient echo (SPGR) (TR/TE = 26/2-8 ms, matrix = 256x256x64, slice thickness = 3 mm), and six-directional axial diffusion echo-planar imaging (EPI) (TR/TE = 5000-10000/63-110 ms, matrix = 128x128 or 256x256, slice thickness = 3-5 mm, 21-40 slices, b = 1000 s/mm^2) sequences.

TMZ with enzastaurin and **TMZ with bevacizumab Protocol**: Exams included axial T1-weighted pre- and post-Gd 3D T1-weighted inversion recovery SPGR (IRSPGR) images (TR =8 ms, TE =3 ms, TI =400 ms, slice thickness =1.5 mm, matrix =256 × 256, FOV =241 × 241 mm^2, flip 158°), axial T2-weighted FLAIR (TR =9500 ms, TE =122 ms, TI =2375 ms, slice thickness =3 mm, matrix =256 × 256, FOV = 241 ×241 mm^2), six directional diffusion tensor EPI (TR = 7,000 ms, TE = 63 ms, matrix size = 256 x 256, slice thickness = 3 mm, b = 1000 s/mm^2, FOV = 220 x 220 mm^2, NEX=4) sequences.

Data Processing

The FLAIR and post-gadolinium T1-weighted images were aligned to the pre-gadolinium T1-weighted images using software developed in our laboratory [15]. Anatomical T2-weighted FLAIR images and post-Gd T1-weighted images were used to define the contrast-enhancing lesion (CEL), T2 hyperintense lesion. The non-enhancing lesion (NEL) was defined as the T2 hyperintense lesion without the CEL or any resection cavity (NEL = T2 hyperintense lesion - CEL). **Figure 6.2** shows an example of the CEL and NEL ROIs.

Figure 6.2 Creation of CEL and NEL ROIs.
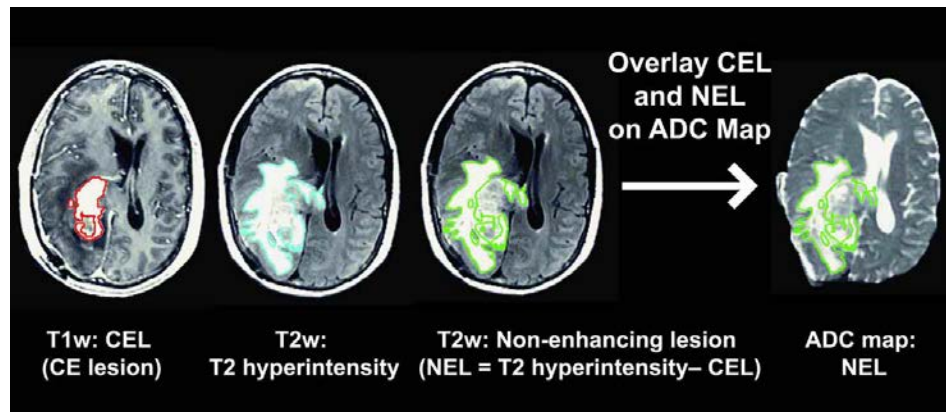
ADC and FA maps were calculated on a voxel-by-voxel basis using software developed in-house and were compared to anatomical imaging by rigidly aligning the T2-weighted (b=0) diffusion image to the T2-weighted FLAIR and applying the transformation to the ADC maps. To facilitate comparison of parameter values between patients and time points, normalized ADC maps (nADC) were generated by dividing the ADC maps by the mode ADC value from the histogram of values from the entire brain.

The latter was found to be a robust representation of the median ADC in normal appearing white matter. The same method was applied to the FA maps to generate normalized FA (nFA) maps.

Statistical Analysis

The volumes and histograms of normalized diffusion parameters (i.e. nADC, nFA) were calculated within the CEL and NEL regions. Parameters that summarized the shape of the histogram and that were considered in the analysis were the median, mode, mean, standard deviation, skewness, kurtosis, 10th, 25th, 75th and 90th percentile of the distribution. The volume of the region within the T2 lesion that had nADC less than 1.5 was determined as a measure of the diffusion tumor burden (DTB). The cut-off for estimating the diffusion tumor burden (DTB) within the NEL had been established as 1.5 times the median value of nADC in NAWM from previous studies that found patients with larger volumes demonstrated a significantly shorter overall survival [16-17]. The percent change for each volume and normalized diffusion parameter was calculated for three time point changes: from pre- to mid-RT (pre-mid), as 100 x [mid-pre]/pre; from mid-post RT (mid-post), as 100 x [post-mid]/mid; and from pre- to post-RT (pre-post), as 100 x [post-pre]/pre within the CEL and NEL regions.

Changes in lesion volumes, median and 10th percentile diffusion values were assessed using a 2-sided Wilcoxon signed-rank tests. Differences between treatments in lesion volumes, median and 10th percentile values, and percent changes at pre-, mid- and post-RT were assessed using kruskal-wallis tests. In cases where significance was found

using kruskal-wallis, a pair-wise test was also performed. Because of the exploratory nature of these analyses, no adjustments were made to account for type I error, and a P-value of <0.05 was considered to be statistically significant.

6.4 Results:

Differences in Anatomic Lesion Volumes:

Comparisons between Therapies: The median volumes (cc) of the CEL and NEL at pre-, mid-, and post-RT for patients receiving TMZ only, TMZ with enzastaurin, and TMZ with bevacizumab are presented in **Table 6.2**. Patients receiving TMZ and enzastaurin demonstrated significantly higher CEL volumes at pre-RT compared to patients receiving TMZ only and patients receiving TMZ and bevacizumab. No differences in the NEL volume was noted at baseline between the three treatment regimens.

Table 6.2: Volume and percent change in volume of anatomic lesions.

		Volume			Percent Change in Volume		
		Pre-RT	**Mid-RT**	**Post-RT**	**Pre-Mid**	**Mid-Post**	**Pre-Post**
CEL	**TMZ only**	2.83 (0.14-18.47)	n/a	2.13 (0.00-41.27)	n/a	n/a	-25% (-100-11879)
	TMZ + enzastaurin	6.25 (0.08-44.74)	4.06 (0.10-19.46)	2.59 (0.04-29.45)	-34% (-92-2650)	-7% (-89-1678)	-42% (-99-2750)
	TMZ + bevacizumab	2.75 (0.19-21.94)	1.11 (0.00-17.65)	0.80 (0.00-8.72)	-66% (-100-128)	-43% (-100-686)	-79% (-100-92)
NEL	**TMZ only**	13.67 (2.35-93.88)	n/a	21.27 (1.04-134.49)	n/a	n/a	20% (-89-1572)
	TMZ + enzastaurin	13.48 (0.83-97.82)	12.41 (0.88-77.45)	14.75 (2.66-68.52)	-5% (-87-645)	36% (-64-1021)	49% (-80-888)
	TMZ + bevacizumab	23.58 (1.71-139.34)	19.90 (1.45-136.57)	6.65 (1.33-39.14)	-4% (-95-591)	-28% (-87-153)	-55% (-93-121)

Comparisons within Therapy: Patients receiving TMZ only did not demonstrate a significant change in CEL or NEL volume from pre- to post-RT scans. Patients receiving TMZ with enzastaurin showed a significant decrease in CEL volume from pre- to mid-RT ($p < 0.0013$), but not from mid- to post-RT, with no change in the volume of the NEL. Patients receiving TMZ with bevacizumab showed a significant decrease in the CEL volume from pre- to mid-RT ($p < 0.0074$), but not from mid- to post-RT. However in this case the volume of the NEL showed a significant decrease from mid-to post-RT (Wilcoxon sign-rank, $p < 0.0006$).

Comparisons in Percentage Change: Patients receiving TMZ with bevacizumab had a significant and more extreme percentage decrease in CEL volume from pre- to mid-RT (median decrease = -66%) than patients receiving TMZ with enzastaurin (median decrease = -34%) (Wilcoxon rank-sum, $p < 0.02$). These patients also showed a significant difference in the percentage change in volume of the NEL lesion between mid- to post-RT (median change of -28%, compared with a median change of +36%, Wilcoxon rank-sum, $p < 0.0001$). **Figure 6.3 (top)** shows the percent change in NEL volume from mid- to post-RT in patients receiving TMZ with enzastaurin and patients receiving TMZ with bevacizumab.

Figure 6.3: Mid to Post %-change in NEL volume and median nADC
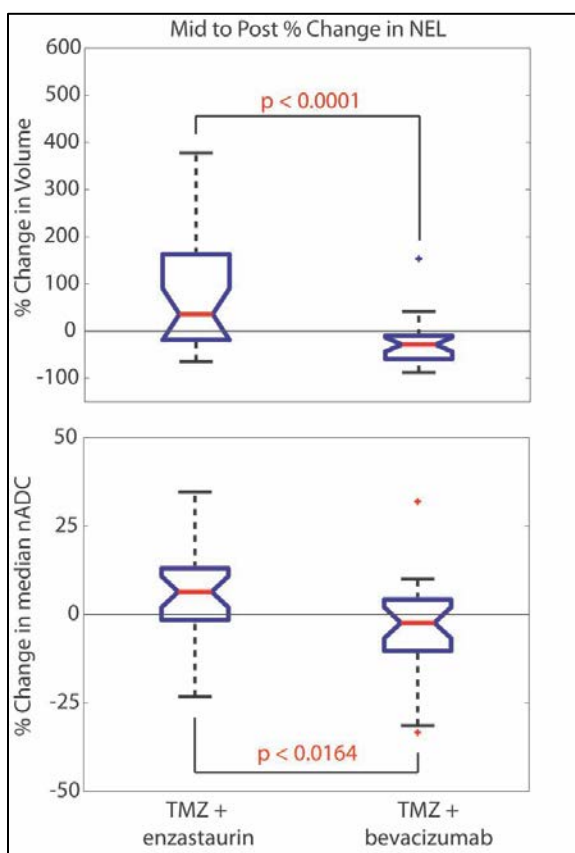
Figure 6.3: Mid to Post % Change in volume of NEL (top) and in median nADC (bottom) for patients receiving TMZ with enzastaurin and patients receiving TMZ with bevacizumab.

Patients receiving TMZ with bevacizumab demonstrated a significant difference in the percentage change from pre- to post-RT in CEL and NEL volume ($p < 0.0075$ and $p < 0.0004$) as compared to patients receiving TMZ only and TMZ with enzastaurin. Specifically, patients receiving TMZ with bevacizumab had a larger percent decrease in anatomic lesion volume for both CEL and NEL, between pre- and post-RT than patients in the other two cohorts (Wilcoxon rank sum, $p < .0075$; $p < 0.0004$ respectively).

Figure 6.4: Pre to post %-change in CEL and NEL by treatment arm
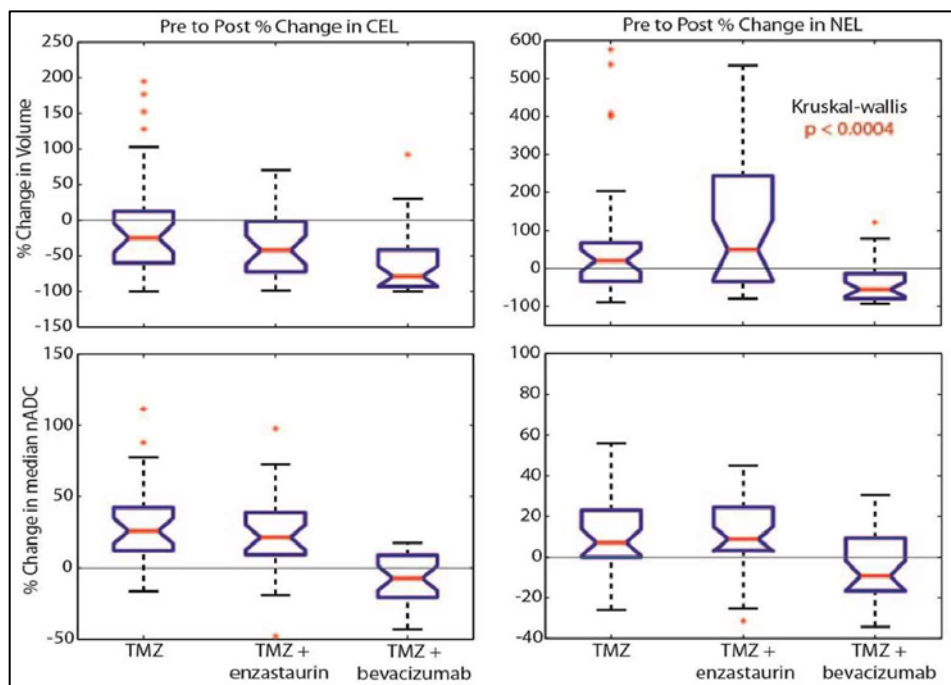
Figure 6.4: Boxplots illustrating pre- to post-RT percent changes in CEL and NEL volumes (top) and median nADC (bottom) by treatment arm.

Differences in Normalized Apparent Diffusion Coefficient (nADC):

Comparisons between Therapies: The median nADC within the CEL and NEL at pre-, mid-, and post-RT for patients receiving TMZ only, TMZ with enzastaurin, and TMZ with bevacizumab are presented in **Table 6.3.** The median nADC of the CEL and NEL at pre-RT was not significantly different for the three patient cohorts (kruskal-wallis, p= 0.2421).

Table 6.3: Median and percent change of nADC in anatomic lesions

		nADC			Percent Change in nADC		
		Pre-RT	Mid-RT	Post-RT	Pre-Mid	Mid-Post	Pre-Post
CEL	TMZ only	1.27 (0.96-1.87)	n/a	1.72 (1.04-2.99)	n/a	n/a	26% (-17-111)
	TMZ + enzastaurin	1.32 (0.82-1.84)	1.48 (0.81-2.06)	1.63 (0.53-2.49)	9% (-36-59)	12% (-10-207)	21% (-48-98)
	TMZ + bevacizumab	1.33 (0.70-1.95)	1.29 (1.02-2.16)	1.27 (0.85-2.00)	-5% (-27-35)	-2% (-49-58)	-7% (-43-186)
NEL	TMZ only	1.40 (1.13-1.95)	n/a	1.51 (1.08-2.08)	n/a	n/a	7% (-26-56)
	TMZ + enzastaurin	1.34 (0.91-2.14)	1.46 (1.05-2.33)	1.47 (1.09-1.93)	2% (-29-37)	6% (-23-35)	9% (-31-45)
	TMZ + bevacizumab	1.47 (1.16-2.06)	1.40 (1.19-1.95)	1.40 (1.18-1.92)	-1% (-35-30)	-2% (-33-32)	-9% (-34-30)

Comparisons within Therapy Cohorts: Patients receiving TMZ only showed a significant increase in median nADC in the CEL and NEL from pre- to post-RT scans (p < 0.0001 and p < 0.0053). Patients receiving TMZ with enzastaurin, showed a significant increase in median nADC in the CEL from pre- to mid-RT (p < 0.0443) and from mid- to post-RT (p < 0.0002). The median nADC in the NEL did not change significantly from pre- to mid-RT, but increased from mid- to post-RT (p < 0.0315). Patients receiving TMZ with bevacizumab showed no significant change in median nADC in the CEL and NEL from pre- to mid-RT or from mid- to post-RT. The 10th percentile data were consistent with these results (values not shown).

Comparisons of Percentage Changes: From pre- to mid-RT, patients receiving the anti-angiogenic treatments showed a significant difference in the percentage change in median nADC within the CEL (TMZ with enzastaurin 9%; TMZ with bevacizumab -5%; Wilcoxon rank sum, p<.02). The percentage changes in median nADC within the NEL

were smaller (TMZ with enzastaurin 6%; TMZ with bevacizumab -2%; Wilcoxon rank sum, p<.02). **Figure 6.3 (bottom)** shows the percentage change in median nADC in the NEL from mid- to post-RT in patients receiving TMZ with enzastaurin and in patients receiving TMZ with bevacizumab.

The percentage change in median nADC in the CEL from pre- to post-RT was significantly different between the three treatment regimens (kruskal-wallis, p < 0.00001). Patients who received TMZ with bevacizumab demonstrated a -7% median change in median nADC in the CEL, as compared to patients who received TMZ only (26%) and patients who received TMZ with enzastaurin (21%). The percentage change in median nADC in the NEL from pre- to post-RT was also significantly different between the three treatment regimens (kruskal-wallis, p< 0.0081). Patients who received TMZ and bevacizumab demonstrated a -9% median change in median nADC in the NEL, as compared to patients who received TMZ only (7%) and TMZ with enzastaurin (9%). **Figure 6.4 (bottom)** demonstrates the pre- to post-RT percentage change in median nADC within the CEL and NEL.

Diffusion Tumor Burden

The levels of ADC within the CEL and NEL for all three patient cohorts were significantly higher than the values in the normal appearing white matter (NAWM). The values for the DTB for all three patient populations are listed in **Table 6.4**. In patients receiving bevacizumab, this volume significantly decreased from mid- to post-RT (p < 0.0298), which is also the time point showed the greatest decrease in the NEL volume. For patients receiving conventional temozolomide only and temozolomide with

enzastaurin, there was no significant decrease in the DTB from pre- to mid-, mid- to post-

, or pre- to post-RT time points.

Table 6.4: Volume of nADC <1.5 within the NEL (Diffusion Tumor Burden)

		Volume			Percent Change in Volume		
		Pre-RT	Mid-RT	Post-RT	Pre-Mid	Mid-Post	Pre-Post
DTB	TMZ only	9.95 (1.41-62.60)	n/a	7.20 (0.89-45.34)	n/a	n/a	-30% (-87-780)
	TMZ + enzastaurin	9.98 (0.70-61.83)	8.02 (0.91-59.29)	6.71 (0.50-41.97)	-11% (-95-152)	-4% (-67-981)	-17% (-78-1037)
	TMZ + bevacizumab	7.77 (0.56-33.53)	13.18 (0.33-46.94)	4.54 (0.52-31.12)	-15% (-81-287)	-21% (-82-156)	-36% (-86-301)

DTB = Diffusion Tumor Burden

Differences in Normalized Fractional Anisotropy (nFA):

There were no significant differences in the median or other nFA parameters in the CEL and NEL at pre-RT, mid-RT, or post-RT among the three treatment regimens. There were no significant changes in median nFA from pre- to mid-, mid- to post-, or pre- to post-RT within each individual treatment regimen. There were no significant differences in the percentage change of median nFA in CEL or NEL from pre- to mid-, mid-to post-, or pre- to post- amongst the three cohorts.

6.5 Discussion:

Glioblastoma is a highly vascularized tumor that overexpresses VEGF. Pathologic angiogenesis driven by misregulation of VEGF is a hallmark of such lesions, and there are now therapeutic agents that target different parts of the pathway. Anti-

angiogenic agents have been shown to alter the presentation of contrast enhancement and therefore compromise the standard contrast-enhancement based metrics of response to therapy [18]. As the interest in integrating these agents into the standard of care in an upfront, newly diagnosed setting increases, there is a need to consider alternative metrics for assessing response to therapy. While DWI has been shown to detect changes in cellularity and tissue disruption following adjuvant chemotherapy in the recurrent setting, it is less well understood how these changes compare between therapies and in conjunction with changes in anatomic lesion volumes for patients with newly diagnosed disease. In the present study, the patterns of changes in anatomic and diffusion imaging parameters were compared among patients with newly diagnosed GBM at pre-, mid- and post-RT scans for three different treatment regimens.

Previous studies have indicated that anti-angiogenic agents can cause a marked decrease in the size of the contrast enhancing lesion on T1-weighted MR images [11, 19]. The results of the present study were consistent with these findings, with patients receiving TMZ with enzastaurin and TMZ with bevacizumab demonstrating a decrease in contrast-enhancement, while patients receiving conventional TMZ alone showing no significant change (see **Figure 6.5**). This is attributed to the combined effects of a reduction in blood volume, flow, and vessel permeability that have been reported to be associated with anti-angiogenic therapies [11, 20-21]. The patterns of changes that were observed in the non-enhancing lesion reflect the differential effects of the two anti-angiogenic therapies with only the bevacizumab being able to causes a reduction in edema.

Figure 6.5: Pattern of early changes in contrast-enhancement differ by treatment arm.
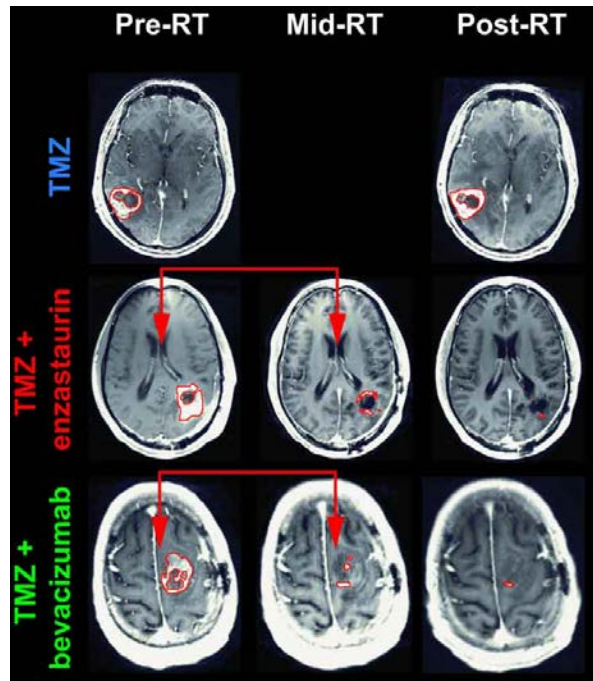
Figure 6.5: T1-weighted post-contrast images at of three patients receiving different treatment regimens. Patients on TMZ with enzastaurin (middle) and TMZ with bevacizumab (bottom) significantly decrease in contrast-enhancement, while TMZ alone (top) does not. Red arrows highlight the additional comparison from pre- to mid-RT for the TMZ with enzastaurin and TMZ with bevacizumab patients.

Previous studies of changes in nADC following radiation therapy and chemotherapy have reported an increase in the observed values shortly after treatment [18-20, 23]. These results are consistent with the findings for the patients receiving TMZ alone and TMZ with enzastaurin [11, 22]. For patients receiving bevacizumab, the observation of stable nADC and decreased volume of the diffusion tumor burden (volume

of nADC < 1.5 within the NEL) suggest that the vascular effects of this treatment modulate the expression of radiation damage. This is supported by in vitro data, which showed that the addition of bevacizumab to conventional treatment can potentiate the response of radiation [25-26] Since vasogenic edema is known to be associated with high VEGF levels and poor outcome, this may confer a therapeutic advantage [27]. Identifying differing patterns of changes in nADC within the NEL between treatment regimens as was seen in this study may help to provide a better understanding of how to utilize these new antiangiogenic therapies.

While corticosteroids are traditionally used to treat radiation-induced edema, their chronic use is also associated with significant morbidity. Since the majority of patients receiving temozolomide and bevacizumab did not receive steroids or were tapering off steroids during our study, the decrease in the volume of the NEL and the changes in nADC values appear to be a direct effect of VEGF inhibition. A similar effect was seen in a recent double-blinded, randomized trial, where Levin et al. showed that all 5 patients who were assigned to the bevacizumab treatment group showed a decrease in the volume of T2-weighted edema [20]. Even if there is no difference in overall survival for bevacizumab in the upfront setting, the observation of a more favorable side effect profile may make it an acceptable alternative to the use of steroids in reducing the amount of edema caused during RT.

6.6 Conclusions:

This study evaluated 99 patients with newly diagnosed GBM on three different therapy regimens and found distinct differences in the patterns of changes in volumes of anatomic lesions and diffusion parameters during the first two months of treatment. Patients treated with radiation, temozolomide and combined antiangiogenic therapy showed a decrease in the enhancing volume, but only patients treated with bevacizumab demonstrated a significant decrease in the non-enhancing volume from pre- to post-RT. Patients receiving temozolomide and enzastaurin or TMZ alone showed a significant increased in nADC during radiotherapy, whereas patients receiving bevacizumab had stable nADC and decreasing volumes of their diffusion tumor burden. These results indicate that imaging biomarkers of response must be tailored to take into account the specific treatment regimen being considered. Since nADC provides a quantitative measure that is reasonably accessible to clinical exams, it may provide a more reliable metric than volumetric T2-weighted hyperintensity when comparing between multiple time points or between different therapies. Future studies will determine whether early changes in anatomic and diffusion parameters are predictive of 1-year progression-free and overall survival, as well as looking at changes in anatomic and diffusion MRI parameters at the time of tumor recurrence

6.7 References:

1. Stupp, R., et al., *Radiotherapy plus concomitant and adjuvant temozolomide for glioblastoma.* N Engl J Med, 2005. **352**(10): p. 987-96.
2. Nghiemphu, P.L., et al., *Bevacizumab and chemotherapy for recurrent glioblastoma: a single-institution experience.* Neurology, 2009. **72**(14): p. 1217-22.
3. Vredenburgh, J.J., et al., *Bevacizumab plus irinotecan in recurrent glioblastoma multiforme.* J Clin Oncol, 2007. **25**(30): p. 4722-9.
4. Norden, A.D., et al., *Bevacizumab for recurrent malignant gliomas: efficacy, toxicity, and patterns of recurrence.* Neurology, 2008. **70**(10): p. 779-87.
5. Kreisl, T.N., et al., *Phase II trial of single-agent bevacizumab followed by bevacizumab plus irinotecan at tumor progression in recurrent glioblastoma.* J Clin Oncol, 2009. **27**(5): p. 740-5.
6. Friedman, H.S., et al., *Bevacizumab alone and in combination with irinotecan in recurrent glioblastoma.* J Clin Oncol, 2009. **27**(28): p. 4733-40.
7. Lai, A., et al., *Phase II study of bevacizumab plus temozolomide during and after radiation therapy for patients with newly diagnosed glioblastoma multiforme.* J Clin Oncol, 2011. **29**(2): p. 142-8.
8. Teicher, B.A., et al., *Antiangiogenic effects of a protein kinase Cbeta-selective small molecule.* Cancer Chemother Pharmacol, 2002. **49**(1): p. 69-77.
9. Goel, S., et al., *Normalization of the vasculature for treatment of cancer and other diseases.* Physiol Rev, 2011. **91**(3): p. 1071-121.
10. Sorensen, A.G., et al., *Increased Survival of Glioblastoma Patients Who Respond to Antiangiogenic Therapy with Elevated Blood Perfusion.* Cancer Res, 2012. **72**(2): p. 402-407.
11. Khayal, I.S., et al., *Evaluation of diffusion parameters as early biomarkers of disease progression in glioblastoma multiforme.* Neuro Oncol, 2010. **12**(9): p. 908-16.
12. Hamstra, D.A., A. Rehemtulla, and B.D. Ross, *Diffusion magnetic resonance imaging: a biomarker for treatment response in oncology.* J Clin Oncol, 2007. **25**(26): p. 4104-9.
13. Li, Y., et al., *Serial analysis of imaging parameters in patients with newly diagnosed glioblastoma multiforme.* Neuro Oncol, 2011. **13**(5): p. 546-57.
14. Rieger, J., et al., *Bevacizumab-induced diffusion-restricted lesions in malignant glioma patients.* J Neurooncol, 2010. **99**(1): p. 49-56.
15. Nelson, S.J., et al., *Registration of images from sequential MR studies of the brain.* J Magn Reson Imaging, 1994. **4**(6): p. 877-83.
16. Crawford, F.W., et al., *Relationship of pre-surgery metabolic and physiological MR imaging parameters to survival for patients with untreated GBM.* J Neurooncol, 2009. **91**(3): p. 337-51.
17. Nelson, S.J. and S. Cha, *Imaging glioblastoma multiforme.* Cancer J, 2003. **9**(2): p. 134-45.
18. Wen, P.Y., et al., *Updated response assessment criteria for high-grade gliomas: response assessment in neuro-oncology working group.* J Clin Oncol, 2010. **28**(11): p. 1963-72.

19.	Keunen, O., et al., *Anti-VEGF treatment reduces blood supply and increases tumor cell invasion in glioblastoma.* Proceedings of the National Academy of Sciences.

20.	Levin, V.A., et al., *Randomized double-blind placebo-controlled trial of bevacizumab therapy for radiation necrosis of the central nervous system.* Int J Radiat Oncol Biol Phys, 2011. **79**(5): p. 1487-95.

21.	Essock-Burns, E., et al., *Assessment of perfusion MRI-derived parameters in evaluating and predicting response to antiangiogenic therapy in patients with newly diagnosed glioblastoma.* Neuro Oncol, 2011. **13**(1): p. 119-31.

22.	Mardor, Y., et al., *Early detection of response to radiation therapy in patients with brain malignancies using conventional and high b-value diffusion-weighted magnetic resonance imaging.* J Clin Oncol, 2003. **21**(6): p. 1094-100.

23.	Zeng, Q.-S., et al., *Distinction Between Recurrent Glioma and Radiation Injury Using Magnetic Resonance Spectroscopy in Combination With Diffusion-Weighted Imaging.* International Journal of Radiation Oncology*Biology*Physics, 2007. **68**(1): p. 151-158.

24.	Chamberlain, M.C., *Pseudoprogression in glioblastoma.* J Clin Oncol, 2008. **26**(26): p. 4359; author reply 4359-60.

25.	Jain, R.K., et al., *Angiogenesis in brain tumours.* Nat Rev Neurosci, 2007. **8**(8): p. 610-22.

26.	Lee, C.G., et al., *Anti-Vascular endothelial growth factor treatment augments tumor radiation response under normoxic or hypoxic conditions.* Cancer Res, 2000. **60**(19): p. 5565-70.

27.	Carlson, M.R., et al., *Relationship between survival and edema in malignant gliomas: role of vascular endothelial growth factor and neuronal pentraxin 2.* Clin Cancer Res, 2007. **13**(9): p. 2592-8.

CHAPTER 7 : Regional Variation in Histopathologic Features of Tumor Specimens From Treatment-naïve Glioblastoma Correlates with Anatomic and Physiologic MR Imaging GBM

In this project, perfusion, diffusion, and anatomic MRI are compared to histologic features of tissue samples from treatment-naïve glioblastoma to identify non-invasive markers of malignant features in both the contrast-enhancing and non-enhancing lesion. This was a large, collaborative project with significant contribution from fields of MR research, clinical radiology, pathology, and statistics. My role in this project was to analyze the perfusion data, create the figures and assist in editing for publication, and facilitate interface of MRI data and pathology data. This project is highly complementarity to Chapter 3. In Chapter 3 we identified DSC post-processing methods predictive of vascular histopathology, and in Chapter 7 we find that these vascular pathologies are associated with malignant features. The work presented here suggests tissue sampling for diagnosis should be guided by physiologic imaging, specifically DSC within the CE-lesion and DWI within the NE-lesion.

7.1 Abstract

Background**:** Histopathologic evaluation of glioblastoma (GBM) at initial diagnosis is typically performed on tissue obtained from regions of contrast enhancement (CE) as depicted on gadolinium-enhanced T1 weighted images. The non-enhancing (NE) portion of the lesion, which contains both reactive edema and infiltrative tumor, is only partially removed due to concerns about damaging functioning brain. The purpose of this study was to evaluate histopathologic and physiologic MR imaging features from image guided tissue specimens from CE and NE regions to investigate correlations between imaging and histopathologic parameters.

Methods**:** 119 tissue specimens (93 CE and 26 NE regions) were acquired from 51 patients with newly diagnosed GBM utilizing stereotactic image-guided sampling. Anatomic, diffusion weighted (DW), and dynamic susceptibility weighted contrast enhanced (DSC) imaging variables from each tissue sample location were obtained and compared with histopathologic features such as tumor score, cell density, proliferation, architectural disruption, hypoxia, and microvascular hyperplasia.

Results**:** Tissue samples from CE regions had increased tumor score, cellular density, proliferation, and architectural disruption when compared to NE regions. DSC imaging variables such as relative cerebral blood volume, peak height, and recovery factor were significantly higher and the percentage of signal intensity recovery was significantly lower in the CE compared to NE regions. DW imaging variables were correlated with histopathologic features of GBM within NE regions.

Conclusion: Image-guided tissue acquisition and assessment of residual tumor from treatment naïve GBM should be guided by DSC perfusion imaging in CE regions and by DW imaging in NE regions.

7.2 Introduction:

Glioblastoma (GBM) is the most common and aggressive primary brain tumor in adults and demonstrates heterogeneous imaging characteristics, histological features, and clinical outcome. Despite significant advances in targeted surgical resection and conformal radiation therapy GBM remains a uniformly deadly disease with a dismal prognosis of less than 10% two-year overall survival (1-6). The presence of infiltrative tumor makes it is difficult to define tumor margins, as regions with malignant features are intermingled within functioning brain that cannot be removed without severe detriment to the patient. Although it may be possible to achieve a "gross total resection" of the contrast enhancing (CE) component of the lesion, there is often a substantial non-enhancing (NE) tumor component that is left behind and eventually becomes the site of focal recurrence.

The current standard for diagnosis and evaluation of prognosis for GBM remains histopathologic analysis of tumor specimens. The WHO II diagnostic criteria of GBM are based upon the presence of microvascular hyperplasia, cellular proliferation, nuclear atypia, architectural disruption, and necrosis (3-6). Tissue samples are typically obtained from the CE component of the tumor (5-8). There is rarely an examination of heterogeneity throughout the entirety of the lesion or an attempt to make direct correlations between imaging and histopathological features. The introduction of MR imaging sequences that provide tissue contrast based upon physiologic parameters, such as diffusion weighted imaging (DW) and T2* dynamic susceptibility weighted contrast enhanced (DSC) perfusion imaging, holds significant promise for identifying characteristics of GBM that are representative of biological behavior (7-26). However,

there remains the need to understand the relationship of these physiologic imaging measures with standard anatomical imaging parameters and histopathologic characteristics so they can collectively be utilized to assess tumor burden (7-11).

DW imaging derived apparent diffusion coefficient (ADC) and fractional anisotropy (FA) values are increasingly utilized in the evaluation of patients with brain tumors as these quantitative measures can be obtained in less than five minutes. ADC and FA values have been previously associated with increased cell density and disruption of normal tissue architecture (27-30). Recent studies investigating tissue samples from patients with primary cerebral nervous system lymphoma have suggested there is an inverse correlation between ADC values and cell density (29-30), but similar studies involving specimens from GBM have yielded varied results (30-33).

DSC perfusion imaging has been widely used to investigate variations in cerebral blood volume (CBV), peak height (PH), recovery factor (RF), and percentage of signal intensity recovery (PSR) (9-16). Prior investigations have shown that DSC imaging provides quantitative parameters that reflect hemodynamic characteristics of normal and tumor microvasculature within the brain and have demonstrated its clinical utility as a companion to anatomic MR imaging differentiating GBM from single brain metastasis (9-19), predicting glioma grade (19-22), and distinguishing recurrent brain tumors from radiation necrosis (34-37).

The purpose of the current study was to determine whether the differential distribution of histological features between tissue specimens that were obtained from CE and NE regions of tumor in patients with treatment naive GBM are associated with

specific anatomic and physiologic MR imaging parameters. This investigation utilized image guided tumor specimens from patients undergoing initial surgical resection in conjunction with a battery of histopathologic tests in order to make direct correlations between their biological features and the corresponding in vivo MR imaging parameters.

7.3 Methods:

Patient Population

A total of 51 adult patients (35 men, 16 women; mean age 64.5, range 33 to 85 years old) with newly diagnosed GBM were prospectively enrolled from July 2007- June 2010 into this Health Insurance Portability and Accountability Act compliant, Institutional Review Board and Committee on Human Research approved study that was in accordance with the ethical standards of the World Medical Association Declaration of Helsinki: Research involving human subjects. Written informed consent was obtained from all patients.

Preoperative Imaging Protocol

Forty six patients underwent preoperative anatomic and physiologic MR imaging using a 3T MR scanner (GE Medical Systems, Milwaukee, WI) and five patients were imaged on a 1.5T Signa Horizon scanner (GE Medical Systems, Milwaukee, WI). Similar MR imaging protocol was utilized: three plane localizer (8.5 ms/1.6 ms, TR/TE), sagittal T1-wighted spin echo (600 ms/17ms, TR/TE), axial three dimensional (3D) T2-weighted fast spin-echo (FSE) (3000 ms/102 ms, TR/TE), axial FLAIR (10,000 ms/148

ms/2200 ms, TR/TE/TI), axial DWI (echo-planar; 10,000 ms/99 ms, TR/TE; 3 mm/0 mm, slice thickness/interslice gap; 256 X 256, matrix size; 24 cm, field of view; 6 gradient directions, b= 0 and 1000 seconds/mm^2), contrast-enhanced 3D spoiled gradient-recalled acquisition in the steady state (SPGR) T1-weighted (34 ms/8 ms, TR/ TE; 1.5 mm/0 mm, slice thickness/interslice gap), and T1-weighted post-contrast spin echo images (600 ms/17 ms, TR/TE). In selected cases, 3D H-1 MR spectroscopy (MRSI) data were acquired for evaluation of tumor metabolism and contributed to the site selection for obtaining tissue samples that were likely to represent tumor, based upon the choline to N-acetyl aspartate (NAA) index (CNI) being greater than 2 standard deviations above normal (12, 38-39).

Axial DSC imaging was performed utilizing a series of T2* gradient-echo echo-planar images (flip angle= 35° or 60°; 54-56/1250-1500 ms, TE/TR; 128 X 128, matrix size; 26 X 26 cm field of view; 8-12 slices, 3-4 mm slice thickness) acquired immediately before, during, and after (total of 60-80 time points) intravenous administration of gadopentetate dimeglumine (0.1 mmol/kg, Gd-DTPA; Magnevist, Bayer HealthCare Pharmaceuticals Inc.) with an MR-compatible power injector (Medrad, Spectris Solaris, Indianola, Pa) at a rate of 4-5 ml/second through a 20 gauge angiocatheter, followed by 20 ml of continuous saline flush. The first 10 echo-planar imaging acquisitions were performed before the injection of Gd-DTPA to establish a pre-contrast baseline. The region selected for DSC imaging coverage included the entire tumor volume as determined by T2-weighted FLAIR and FSE images. A TE of 54 ms and flip angle of 35° were selected to maximize the effect of susceptibility changes while minimizing T1 effect during the first pass of contrast agent.

Physiologic MR Image Processing

Post-contrast T1 weighted 3D SPGR images, T2-FLAIR images, DSC perfusion images, and DW images, and, where available, H-1 MRSI data were transferred to a commercially available linux workstation where they were processed and co-registered as described previously (40). The accuracy of co-registration was manually verified by visual inspection.

DSC and DW image analysis was performed using software developed by our group (14, 40-41). The T2* dynamic signal intensity time curves acquired during the first pass of the gadolinium bolus were converted into dynamic $\Delta R2^*$ curves and re-sampled to match the spatial resolution of the anatomic imaging series. Peak height (PH) was defined as the maximum $\Delta R2^*$ value of the first-pass curve. Percentage of signal recovery (PSR) was calculated as the difference between the PH value and the average values of the final five time points in the dynamic $\Delta R2^*$ series divided by the PH value. CBV and recovery factor (RF) maps were calculated on a voxel-by-voxel basis utilizing a modified gamma-variate function that takes into account leakage of the contrast agent (14, 40-41). DW images were used for the production of ADC and FA maps on an automated voxel-by-voxel basis. Several of the physiologic MR imaging parameters were normalized by dividing the estimated values in normal appearing white matter (NAWM) from the contralateral hemisphere before comparing with the histological data (rCBV, rPH, rADC, rFA).

Preoperative Tumor Tissue Site Selection and MR Imaging Analysis

Anatomic and physiologic MR images were used to guide the prospective selection of tissue sampling sites within the T2 FLAIR and FSE hyperintense portion of the tumor. Tissue sampling sites were preoperatively planned and marked on the anatomical images that were used by the surgical navigation workstation (Brainlab, VectorVision Navigation System; Medtronic, Stealth Station). Criteria used to plan sites were based upon results from previous studies as having either rPH >3, ADC<1200, or, when MRSI data was available, CNI>2 (14, 19, 32-33, 38-39, 42-43). The tissue targets were marked on the anatomic images to be used by the surgeon for intraoperative sample localization. Requested tissue sampling sites were obtained more than 85% of the time with at least one requested tissue sampling site for all patients being sampled, however, it was not always possible to match all the requested tissue targets so the actual locations of the acquired tissue sample were saved on the surgical navigational system as both screenshots and as a list of image coordinate values. The tissue coordinates were subsequently used to define spherical regions of interest (ROIs) with a 5 mm diameter and used to record corresponding values of anatomic and physiologic MR imaging parameters. Accurate co-registration of intraoperatively generated screen shots that defined the tumor specimen site and the corresponding ROI were reviewed by a neuroradiologist, who was blinded to other patient data. The median intensity values for each of the relevant imaging parameter within the sample ROIs were determined for the subsequent imaging analysis using automated software developed in our research group.

Intraoperative Tissue Collection and Histopathologic Tumor Analysis

After removal from the brain, tissue specimens were divided in half with one-half snap frozen in liquid nitrogen, for potential future studies, and one-half immediately placed in Zinc-formalin for 4-6 hours, dehydrated in a series of graded alcohols, and infiltrated with low temperature paraffin for histological analysis. Sections from the tissue specimens were stained with hematoxylin and eosin (H&E) or immunostained using an automated immunohistochemical (IHC) tissue staining process (Ventana Medical Systems Benchmark XT). Digital images were captured with a microscope (Olympus, Model BX41TF) and digital microscope camera (Olympus, Model DP70).

For each tissue specimen, the presence of tumor cells was scored based upon review of H&E stained sections by a neuropathologist as follows: 0, no tumor present; 1, infiltrating tumor margin; 2, infiltrating cellular tumor; 3, highly cellular infiltrating tumor involving greater than 75% of the tissue. Tumor cells were identified based upon morphologic features including cytologic atypia, enlarged nuclear to cytoplasmic volume ratio, and hyperchromasia. The cumulative extent of necrosis was scored as follows: 0, no necrosis; 1, focal necrosis involving less than 50% of the tissue area; 2, extensive necrosis involving greater than or equal to 50% of the tissue area.

The degree of microvascular hyperplasia, hypoxia, and architectural disruption was qualitatively measured using IHC stained sections for Factor VIII, CA-9, and SMI-31, respectively, using an ordinal scale of immunoreactivity. For Factor VIII staining, the presence of specific microvascular elements were scored as follows: 0, delicate microvasculature only; 1, simple hyperplastic structures identified (hyperplastic capillaries with definitive lumen); and 2, complex microvascular hyperplasia

(circumferential multi-layered and glomeruloid type vessels). The contribution of each type of microvascular element to the overall vascularity was scored as follows: 0, not present; 1, present but not predominant; and 2, predominant.

The degree of hypoxia, as denoted by CA-9 (carbonic anhydrase-IX) positivity, was scored using a three tiered system: 0, no positive staining; 1, less than 10% of the tissue; 2, greater than or equal to 10% of the tissue but less than 25%; 3, greater than or equal to 25% of the tissue is CA-9 positive. The CA-9 gene has a hypoxia-responsive element in its promoter and its expression at the protein level is commonly used as a marker for hypoxia. To assess the degree of architectural disruption we performed immunohistochemistry with SMI-31, an antibody against a phosphorylated neurofilament epitope in thick and thin axons, and scored the samples based on the extent of SMI-31 staining as follows: 0, no disruption of the normal architecture; 1, minimal disruption; 2, mild disruption; and 3, severe disruption with no residual SMI-31 immunostaining.

The total number of cells and the total number of Ki-67 stained cells was quantified in 3-5 separate fields at 20x magnification to assess total cell number and standardized proliferation index. A minimum of 400 nuclei were counted per sample. An attending neuropathologist with greater than 10 years experience and who was blinded to the results of MR imaging, performed all quantitative and qualitative histopathologic assessments. All of the tissue specimens were of sufficient size and IHC staining quality to be included for analysis.

<u>Statistical Analysis</u>

There were three components to the analysis: 1) assessing intra-tumor variation for each histopathologic and MR imaging variable, 2) assessing whether MR imaging parameters (perfusion, diffusion, and anatomic) were predictive of GBM histopathology; and, 3) evaluating associations within histopathology features and in-vivo MR imaging parameters.

Association of Histopathology Characteristics and MR Imaging Variation Within Tumor Specimen Regions: Mixed-effects modeling was performed to estimate the coefficient of intra-tumor variation (as measured in CE versus NE regions) for each histopathologic and MR imaging variable in the subset of patients who had tumor specimens from both regions. For each continuous variable the initial model included a fixed effect for each tissue specimen site and a random effect for each patient. This model can be written as:

$$y_{ijk} = \beta_j + b_i + \varepsilon_{ijk}; i = 1,...,51; j = 1,2; k = 1,...,k_i$$

where y_{ijk} is the histopathologic or imaging value of the ith subject, in the jth tumor specimen region, for the kth biopsy; β_j is the tumor specimen specific intercept; and ε is the residual. This model assumes that $b_i \sim N(0,\sigma_b^2)$ and $\varepsilon_{ijk} \sim N(0,\sigma^2)$. The assumptions of normality for the random effects were verified with quantile-quantile plots. For some

histological and MR imaging variables, plots of residuals against fitted values demonstrated heteroscedasticity within tumor specimen regions. In those cases, the model was adjusted to account for unequal variances within tumor specimen regions. Interactions between the fixed and random effects were also investigated. Models were pair-wise compared and the coefficient/p-value for the best model is reported. The R Language and Environment for Statistical Computing and NLME package were used for the continuous-valued outcome mixed effect models.

To compare the ordinal histopathology variables between CE and NE tumor specimen regions we employed a proportional odds logistic regression model with repeated measures to model the probability of observing a lower versus higher response. This model is written as:

$$\log it[P(Y_{ijk} \leq \kappa | X_i, Z_i)] = \alpha_k + x_{ij}'\beta + Z_{ij}'\beta + z_{ij}'b_i; i = 1, \ldots, 35; k = 1, \ldots, c - 1,$$

where c is the total number of levels of the ordinal variable, X_i is the design matrix for the fixed effects and Z_i for the random effects; x_{ij} and z_{ij} are rows corresponding to the jth biopsy region; and β & b_i are the vectors of fixed and random parameters. The intercepts are fixed and category dependent. The odds ratio and p-value for each variable is reported. The ordinal-valued outcome mixed effect models were analyzed with PROC GENMOD in SAS v.9.2.

Predictive Ability of MR Imaging Parameters Separately by Tumor Specimen Region:

The primary analysis focused on whether anatomical, diffusion, or perfusion parameters (rT1C, rFSE, rFLAIR, rFA, rADC, rCBV, rPH, PSR, or RF) were predictive of malignant glioma histopathology as assessed by tumor cellularity (H&E), proliferation (Ki-67), overall cell density (H&E), necrosis (H&E), microvascular hyperplasia (Factor VIII), hypoxia (CA-9), architectural disruption (SMI-31), or microvascular morphology (delicate, simple, complex; Factor VIII) in each region. Univariate mixed effects linear models were fit as described above were used with each histopathology feature as the outcome and the imaging parameter as a fixed predictor adjusting for the patient effect. For models involving continuous outcomes, the coefficients were reported if they were statistically significant at P≤ 0.05 and if the within-tumor residual variance decreased at least 5% when compared to the unconditional means model. Each association was also assessed by randomly selecting one sample per patient and calculating a Kendall's Tau correlation coefficient (τ). This sampling process was repeated 100 times. A strong correlation was identified if the corresponding p-value for τ was significant at P≤ 0.05 in 70% of the 100 samples. The median τ and p-value is reported when a correlation did not exist linearly. Imaging parameters statistically significant at P≤ 0.15 were modeled pair-wise with and without interaction. These models were compared to the univariate model to confirm if the additive effect strengthened the model.

Associations Among Histopathology Scores and MR Imaging Separated by Tumor Specimen Region: Exploratory associations were estimated within histopathology features and within in-vivo MR imaging parameters stratified by tissue sample regions.

Univariate mixed effects linear models were fit as described above. Only associations of the following MR imaging variables are summarized: rT1c, rFSE, rFLAIR, rCBV, rADC, and rFA. Hypoxia, necrosis, and complex vessel scores were excluded from analyses involving NE regions because there were a relatively small number of non-zero values.

7.4 Results:

A total of 119 image-guided tissue specimens were obtained from regions of suspected tumor during surgical resection of 51 patients who were assessed as having newly diagnosed GBM. Ninety three tissue specimens were obtained from CE regions and 26 from NE regions. The analysis of DSC perfusion data was limited to patients imaged with a flip angle of 35º to minimize T1 signal intensity effects during the first pass of the contrast agent (N= 35, Total number of tissue samples= 72).

Differential Distribution of Histopathologic Features Within CE and NE Regions

Summary statistics for regional histopathology features obtained from this cohort are presented in **Table 7.1** and **Figure 7.1**. Eighty one percent of NE tissue specimens and 90% of CE tissue specimens contained tumor. Considering that the surgeon was not always able to sample the requested location, the high tumor identification rate indicated that the imaging criteria used for tumor targeting were highly effective. Tissue

specimens obtained from CE regions had significantly increased tumor score (P= 0.04)

and architectural disruption as demonstrated by SMI-31 (P= 0.05) when compared to NE

regions. Proliferation and tumor cell density were also found to be elevated within CE

regions (proliferation mean of 15.8% versus 4.6%, P= 0.04; tumor cell density mean of

268 versus 146, P= 0.007). The relative contribution of delicate vascular morphology

was higher in NE tumor tissue regions (P = 0.01). As is shown in **Figure 7.1**, there were

relatively few samples from NE regions with complex microvascular hyperplasia,

hypoxia, and necrosis (19%, 4% and 0% respectively).

Figure 7.1: Frequency distribution of histopathologic features of GBM among contrast-enhancing and non-enhancing regions.
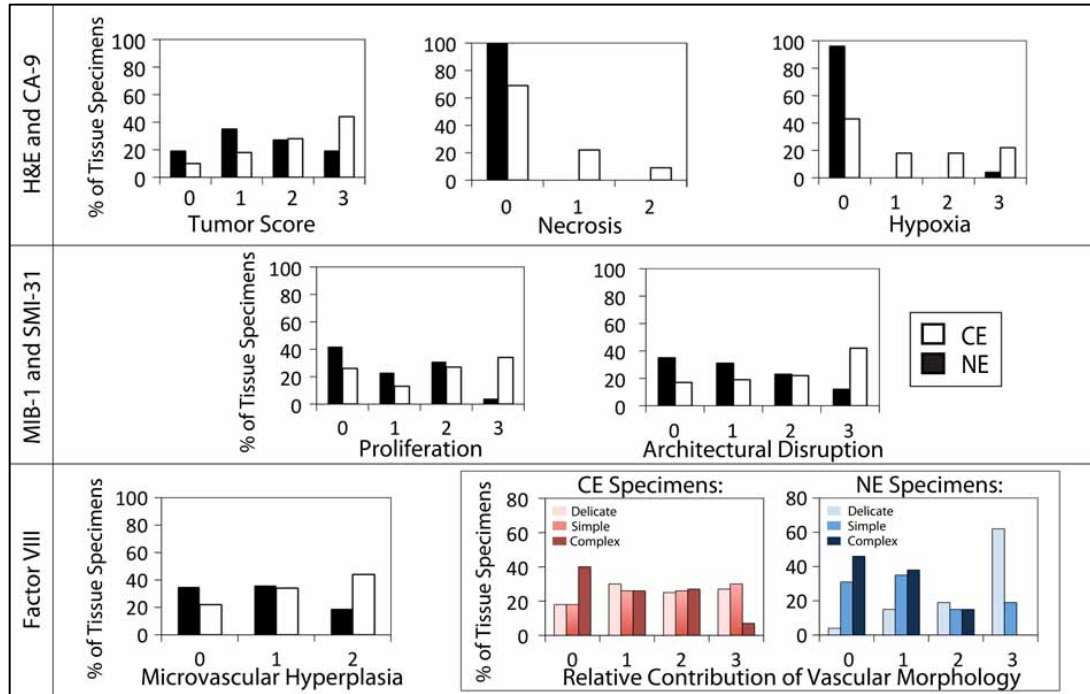
Figure 7.1:. Histopathologic features were noted to be heterogeneously distributed within both enhancing and non-enhancing regions. Bar graphs of the entire cohorts histopathological features demonstrates significantly increased distribution of tumor score, architectural disruption, and complex vascular hyperplasia morphology within contrast enhancing regions when compared to non-enhancing biopsy regions ($P < 0.05$). Delicate vascular morphology distribution was increased within non-enhancing biopsy regions when compared to contrast enhancing regions ($P = 0.01$). The distributions of overall vascular hyperplasia and simple microvascular hyperplasia morphology were not different between enhancing and non-enhancing regions. Hypoxia and pseudopalisading necrosis were not observed in non-enhancing regions.

Table 7.1: Regional histopathological summary statistics and differential regional expression

Regional Histopathological Summary Statistics and Differential Regional Expression											
Categorical Features											
Histologic Value	**Tissue Region**	**Pt #**	**TS #**	**Frequency Distribution (%)**				**Random Effect Model Analysis**			
				0	**1**	**2**	**3**	**# Pairs**	**Odds Ratio**	**95% Confidence Interval**	**P-Value**
Tumor Score	NE	20	26	19	35	27	19	16	2.6	1.1 6.6	0.04
	CE	47	90	10	18	28	44				
Necrosis	NE	20	26	100	0	0	NA	17	NA	NA NA	NA
	CE	48	92	69	22	9	NA				
Hypoxia	NE	20	26	96	0	0	4	16	NA	NA NA	NA
	CE	47	89	45	17	18	22				
AD	NE	20	26	35	31	23	12	16	2.8	1 7.7	0.05
	CE	46	88	17	19	22	42				
Total MVH	NE	20	26	35	46	19	NA	16	2.5	1 6.2	0.06
	CE	47	89	22	44	34	NA				
Delicate MVH	NE	20	26	4	15	19	62	16	0.3	0.1 0.8	0.01
	CE	47	89	18	3	25	27				
Simple	NE	20	26	31	35	15	19	16	2	0.8 5.2	0.15

Histologic Value	Tissue Region	Pt #	TS #					# Pairs	B			P-Value
MVH	CE	47	89	18	26	26	30					
Complex MVH	NE	20	26	81	11	8	0	16	NA	NA	NA	NA
	CE	47	89	60	16	10	14					

Continuous Features

Histologic Value	Tissue Region	Pt #	TS #	Min	Median	Max	SD	# Pairs	B	95% Confidence Interval		P-Value
Proliferation	NE	20	26	0.0	4.6	26.7	7.3	16	5.9	0.2	11.6	0.043
	CE	47	89	0.0	15.8	59.2	13.9					
Tumor Cell Number	NE	20	26	66.5	145.5	474	88.7	17	103	30.6	175.1	0.007
	CE	48	91	43.0	267.8	921	165.9					

Note: Regional summary statistics of histopathological values obtained from contrast enhancing (CE) and non-enhancing (NE) regions. The estimated difference in effect between the two regions (NE as baseline) are summarized by the odds ratio/p-value from a random effects model. Tumor score: 0, no tumor present; 1, infiltrating tumor margin; 2, infiltrating cellular tumor; 3, highly cellular infiltrating tumor involving greater than 75% of the tissue. Necrosis: 0, no necrosis; 1, focal necrosis involving less than 50% of the tissue area; 2, extensive necrosis involving greater than or equal to 50% of the tissue area. Hypoxia: 0, no positive staining; 1, less than 10% of the tissue; 2, greater than or equal to 10% of the tissue but less than 25%; 3, greater than or equal to 25% of the tissue is CA-9 positive. AD: 0, no disruption of the normal architecture; 1, minimal disruption; 2, mild disruption; and 3, severe disruption with no residual SMI-31 immunostaining. Total MVH: 0, delicate microvasculature only; 1, simple hyperplastic structures identified (hyperplastic capillaries with definitive lumen); and 2, complex microvascular hyperplasia (circumferential multi-layered and glomeruloid-type vessels). Relative contribution of each vascular morphology (Delicate, Simple, Complex) to total vascularity within the sample: 0, no contribution; 1, minimal; 2, prevalent; 3, predominant. Proliferation is based on total number of Ki-67-positive cells relative to total number of cells in 3-5 separate fields at 20x magnification. Tumor cell number: Total cells per field at 200x magnification. AD denotes architectural disruption. Pt # denotes number of patients. TS # denotes number of tissue samples. NA denotes not applicable.

Differential Distribution of MR Imaging Parameters Within CE and NE Regions

Summary statistics for regional anatomic and physiologic MR imaging values obtained from this cohort are summarized in **Table 7.2** and **Figure 7.2**. Compared to NE regions, tissue specimens obtained from CE regions demonstrated significantly higher levels of rT1C, rFSE, rCBV, rPH, and RF (P< 0.01). As expected, PSR was found to be significantly lower within CE regions when compared to NE regions (P= 0.007). The distributions of rADC, rFA, and rFLAIR were not found to be different between CE and NE regions.

Table 7.2: Regional anatomic and physiologic MR imaging values: summary statistics and differential regional expression

Table 7.2: Regional Anatomic and Physiologic MR Imaging Values: Summary Statistics and Differential Regional Expression												
		Summary Statistics						Mixed Effects Model				
MRI Value	Tissue Region	Pt #	TS #	Min	Median	Max	Std	Pair #	B	95 % Confidence Interval		P value
rT1C	NE	20	26	0.60	0.92	1.42	0.21	17	0.4	0.2	0.7	0.004

Section	Measure	Region	Pt #	TS #	Min	Median	Max	SD	Pt #	Coeff	CI low	CI high	p-value
		CE	48	93	0.55	1.29	2.61	0.46					
	rFSE	NE	20	26	0.94	1.57	4.36	0.92	17	0.7	0.2	1.3	0.007
		CE	48	93	0.38	1.94	6.34	0.92					
	rFLAIR	NE	20	26	0.71	1.42	2.35	0.37	17	0.1	-0.1	0.3	0.569
		CE	48	93	0.83	1.50	2.94	0.41					
DSC Perfusion	rCBV	NE	11	15	0.47	1.64	2.77	0.70	7	0.9	0.4	1.4	0.003
		CE	29	52	0.45	2.29	8.61	1.50					
	rPH	NE	12	17	0.49	1.48	4.06	0.86	8	0.6	0	1.1	0.046
		CE	30	53	0.27	1.67	6.74	1.08					
	PSR	NE	12	17	77.5	94.5	99.5	5.9	8	-19.6	-31.9	-7.4	0.007
		CE	30	53	34.5	78.5	96.5	16.9					
	RF	NE	11	15	0.89	2.65	3.75	0.85	7	2.6	1.2	4	0.002
		CE	29	52	0.37	3.60	13.15	3.01					
Diffusion	rADC	NE	19	24	0.86	1.09	2.34	0.37	16	0.2	-0.1	0.5	0.156
		CE	47	90	0.35	1.43	3.69	0.48					
	rFA	NE	19	24	0.37	1.03	2.37	0.50	16	-0.2	-0.4	0.1	0.224
		CE	47	90	0.21	0.68	2.50	0.36					

Note: Regional summary statistics of anatomic and physiologic MRI values based on contrast enhancement (CE) or non-enhancement (NE). The estimated difference in effect between the two regions (NE as baseline) are summarized by the coefficient/p-value from mixed effects models. Relative values are indicated by prefix r, which indicates tumor value divided by contralateral white matter value. rFLAIR= relative FLAIR T2 hyperintensity value, rT1C= relative T1 enhancing value, rFSE= relative fast spin echo T2 hyperintensity value, rCBV= relative cerebral blood volume, rPH= relative peak height, PSR= percentage of signal intensity recovery, RF= Recirculation factor, rADC= relative apparent diffusion coefficient, rFA= relative fractional anisotropy, Min= minimum value within region of interest, Pt # denotes number of patients, TS # denotes number of tissue samples, Max= maximum value within region of

interest, Std= standard deviation.

Figure 7.2: Distribution of DSC perfusion, diffusion, and anatomic T1 and T2 weighted MR imaging characteristics among contrast enhancing and non-enhancing regions.
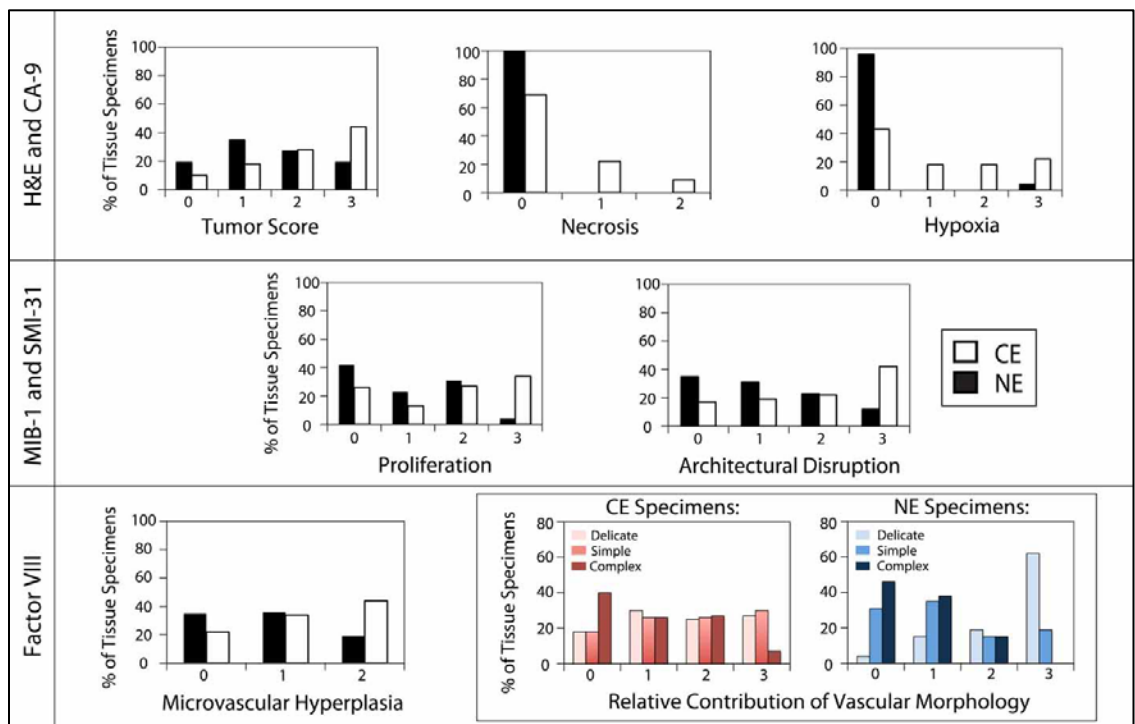
Figure 7.2: Histograms as a distribution of the entire cohort's MR imaging values demonstrates significantly elevated rT1C, rFSE, rCBV, rPH, RF values within contrast enhancing regions when compared to non-enhancing regions (P<0.01). Mean PSR values were significantly lower within contrast enhancing regions when compared to non-enhancing regions (P<0.01). rADC, rFA, and rFLAIR were not observed to be differentially distributed between contrast enhancing and non-enhancing regions.

Association of Histology and MR Imaging Parameters Within CE Tumor Regions

Table 7.3 summarizes the statistically significant associations between MR imaging and histopathology parameters in samples from CE tumor regions (detailed results are shown in **Supplemental Table 7.6**). Univariate mixed effects model analyses demonstrated that tumor score was associated with rFLAIR, rCBV, rPH, and RF (P= 0.01, 0.003, 0.011 and 0.015). Microvascular hyperplasia and proliferation were associated with rT1C, rCBV, and rPH (P= 0.027, 0.005 and 0.005; Fig**ure 7.3**). Tumor cell density was associated with rCBV and rPH (P= 0.01). Necrosis was associated with rCBV (P= 0.003) and delicate vasculature was inversely associated with rT1C (P= 0.033). There were no significant univariate relationships observed between histopathologic features and PSR, rFSE, rADC, or rFA parameters within CE regions.

Pairwise models of rFLAIR with perfusion parameters rCBV (Odds Ratio; OR= 2.38, P= 0.10), rPH (OR= 2.46, P= 0.002), or RF (OR= 0.85, P= 0.044) were predictive of tumor score. Additional pairwise predictive models of tumor score included RF with rCBV (OR= 2.26, P= 0.003) and RF with rPH (OR= 2.74, P= 0.03). Pairwise models of rT1C with rCBV (OR= 1.88, P= 0.007) and rT1C with rPH (OR= 2.43, P= 0.002) were predictive of microvascular hyperplasia.

	CE Region								NE Region							
Table 7.3: Associations Between Key Histopathologic and In Vivo MR Imaging Parameters																
	rT1C	rFSE	rFLAIR	rCBV	rPH	RF	rADC	rFA	rT1C	rFSE	rFLAIR	rCBV	rPH	RF	rADC	rFA
Tumor score			-	+	+	-				-			+		-	
Proliferation	+			+							-					-
Total MVH	+			+	+											
Delicate MVH	-								+							+
Simple MVH					+											
Necrosis				+												
TCN				+	+								+			
AD													+		-	+

Note: Statistically significant (P< 0.05) associations observed between histopathologic and MR imaging parameters. + denotes a positive correlation. – denotes inverse correlation. AD denotes architectural disruption. Total MVH denotes all microvascular hyperplasia including both simple and complex. Tumor cell density denotes mean tumor cell number per 200x-microscopic field. Tumor cell density denotes mean tumor cell number per 200x-microscopic field. TCN= tumor cell number per high power field. CE denotes contrast enhancing. NE denotes non-enhancing.

Figure 7.3: Regional correlation between histopathologic features of GBM and physiological MR imaging within contrast enhancing regions.
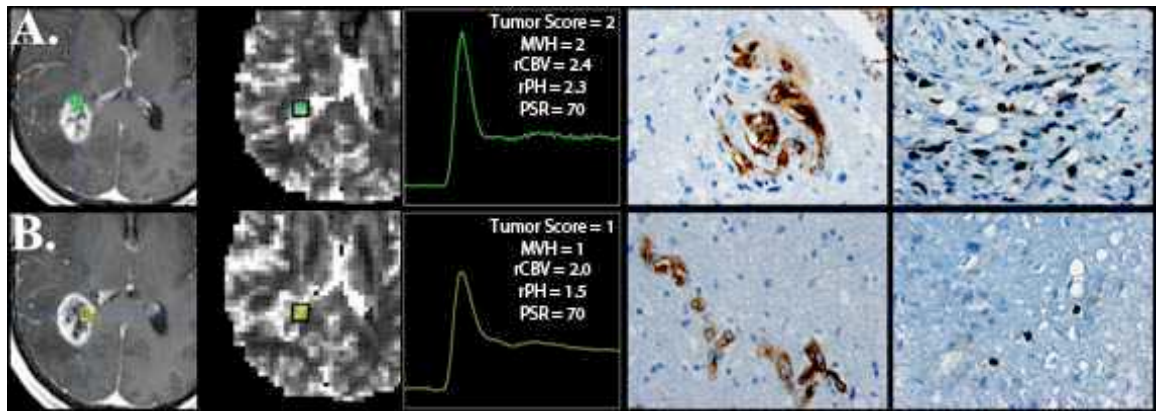
Figure 7.3: Site of 2 tumor samples (colored circles; A) Green, B) Yellow) planned on axial T1 weighted MR images (column 1), co-registered CBV maps and average dynamic $\Delta R2^*$-time curve within the tissue sample region (column 2 and 3), and histopathological features (column 4, microvascular hyperplasia; column 5, cellular proliferation) demonstrates significant correlation between perfusion MR imaging, microvascular hyperplasia, and cellular proliferation within contrast enhancing regions. Contrast enhancing regions with elevated microvascular hyperplasia and cellular proliferation (A) demonstrated elevated rCBV and rPH values (insert, column 3) when compared to similar appearing contrast enhancing regions which demonstrate less aggressive tumor features (B).

Association of Histology and MR Imaging Parameters Within NE Tumor Regions

The associations between MR imaging and histopathologic features in NE regions are summarized on the right hand side of **Table 7.3** (detailed results are shown in **Supplemental Table 7.7**). Inverse associations were observed for tumor score with rFSE and rADC (P= 0.03 and 0.02) as well as proliferation with rFLAIR and rADC (P= 0.01; **Figure 7.4**). Architectural disruption (SMI-31) was inversely related to rADC (P= 0.005; **Figure 7.4**) but positively correlated to rFA and rPH (P= 0.035 and 0.038). Tumor cell density was associated with increasing rPH (P= 0.05), while delicate microvasculature was found to be positively associated with rT1C (P= 0.03) and rFA (P= 0.009).

Figure 7.4: Regional correlation between histopathologic features of GBM and physiological MR imaging within non-enhancing regions.
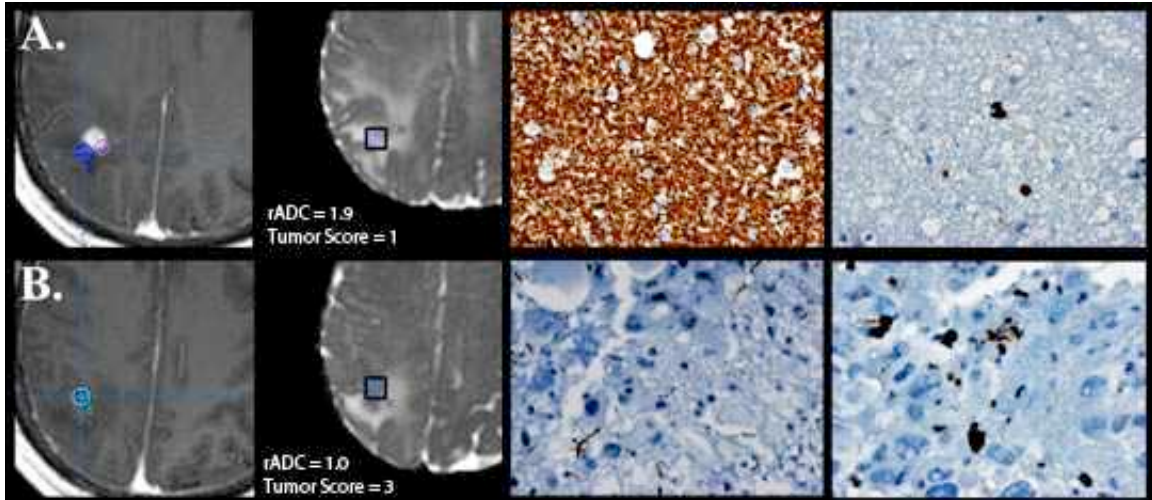
Figure 7.4: Site of 2 tumor samples (colored circles; A) Violet, and B) Blue) planned on axial T1 weighted MR images (column 1), co-registered DW maps (column 2), and histopathologic features (column 3, architectural disruption; column 4, cellular proliferation) demonstrates significant inverse correlation between diffusion weighted MR imaging, architectural disruption, and cellular proliferation within non-enhancing regions. Non-enhancing regions with increased architectural disruption and cellular

proliferation (B) demonstrated decreased rADC values (insert; column 2) when compared to similar appearing non-enhancing regions which demonstrate less aggressive tumor features (A).

Associations Between Histology Parameters

The potential interactions between histopathologic features within each tumor region are summarized in **Table 7.4** (Details shown in Supplemental **Table 7.8**). No assessment was made for complex microvascular morphology because the number of samples with positive scores was relatively small (41% for CE and 20% for NE regions). Within CE tissue specimens, all histopathologic features, except for delicate vasculature, were positively associated with tumor score, proliferation, and total microvascular hyperplasia. Delicate microvascular morphology was inversely associated with tumor score, proliferation, total microvascular hyperplasia, and necrosis within CE tissue specimens. Additionally, CE tissue specimens demonstrated a positive association between hypoxia, architectural disruption, simplex microvascular morphology, and necrosis.

Relationships between proliferation, microvascular hyperplasia, architectural disruption, and simplex vasculature scores were similar in NE tissue specimens, however, a low number of positive scores for necrosis and hypoxia (0% and 4%) precluded evaluation of these features. NE tissue specimens lacked a significant association of

delicate microvascular morphology with other histopathologic features and for tumor cell density with proliferation or microvascular hyperplasia.

Table 7.4: Correlations between key histopathologic features.

Table 7.4: Correlations Between Key Histopathologic Features								
	CE Tissue Specimen				NE Tissue Specimen			
	Tumor Score	Proliferation	Total MVH	Necrosis	Tumor Score	Proliferation	Total MVH	Necrosis
Tumor Score								
Proliferation	+				+			
Total MVH	+	+			+			
Necrosis	+	+	+		NA	NA	NA	
CA9	+	+	+	+	NA	NA	NA	NA
AD	+	+	+	+	+	+	+	NA
TCN	+	+	+					NA
Delicate MVH	-	-	-	-				NA
Simple MVH	+	+	+	+	+	+	+	NA

Note: Statistically significant (P< 0.05) associations observed between histopathologic features of GBM. + denotes a positive correlation. – denotes inverse correlation. AD denotes architectural disruption. Total MVH denotes all microvascular hyperplasia including both simple and complex. Tumor cell density denotes mean tumor cell number per 200x-microscopic field. TCN= tumor cell number per high power

Associations Between MR Imaging Parameters

Associations among MR imaging parameters are summarized in **Table 7.5** (Details are shown in **Supplemental Table 7.9**). rFSE and rFLAIR were associated within CE and NE regions. rT1C was inversely associated with rFSE and rFLAIR only within NE regions. rCBV was positively associated with rPH and inversely associated with rADC in CE and NE regions. rCBV was associated with rT1C only in CE regions. rADC was positively associated with rFSE and inversely associated rFA in CE and NE regions. Similar parameters from the same imaging modality such as rCBV and rPH were positively related, and PSR was inversely related with RF for CE and NE regions.

Table 7.5: Correlations between key in vivo MR imaging parameters.

Table 7.5: Correlations Between Key In Vivo MR Imaging Parameters								
	CE Region				NE Region			
	rT1C	rFSE	rCBV	rADC	rT1C	rFSE	rCBV	rADC
rT1C			+			-		
rFSE				+	-			+
rCBV	+			-				-
rADC		+	-			+	-	

7.5 Discussion:

In this study we prospectively collected tissue specimens from CE and NE regions in patients with untreated GBM utilizing MR image-guided neurosurgical techniques to evaluate their physiologic MR imaging and histopathological characteristics and to assess the correlation of in vivo MR parameters with histological features of GBM. We observed that a number of histopathologic features and quantitative MR imaging parameters differ between CE and NE regions. These variables also demonstrate significant correlations suggesting that DSC perfusion and DW MR imaging are capable of detecting heterogeneous histopathologic features within anatomically distinct portions of treatment naive GBM.

The results of our study suggests the tissue sampling site criteria of either rCBV>3, ADC<1200, or CNI>2 within CE and NE regions proved to be highly effective in identifying tumor containing regions for patients with treatment naïve GBM. This is of particular interest for defining tumor burden in NE regions, where being able to distinguish reactive edema from biologically active infiltrative tumor is clinically important. Previous studies in patients with newly diagnosed GBM have shown that increased volumes of ADC< 1200 or CNI> 2 within the T2 hyperintense lesion were

associated with poor overall survival prior to initial surgical resection (42). Additionally, Saraswathy et al have demonstrated that increased volumes of these three physiologic MR parameters within the T2 hyperintense lesion at the post surgery and pre-treatment examination are associated with decreased survival (43). Future studies will follow up on these findings by considering these measures as candidates for defining physiological as opposed to anatomical tumor burden in serial studies of response to therapy.

From the comparison of histological parameters within CE versus NE regions, it was clear that the hallmark histopathologic features of GBM, including necrosis and complex microvascular hyperplasia, were present in a significant number of CE regions but either absent or rare in NE regions. Despite this, the majority of NE regions (81%) did contain tumor cells as indicated by a positive tumor score. Additionally, a median Ki-67 score of 4.55% was observed among the NE regions. Interestingly, the hypoxia score was zero for all except one of the NE tumor specimens. Give that well oxygenated tissues are more sensitive to radiation damage, this finding raises the possibility that tumor in NE regions of GBM is more effectively treated by radiation or DNA damaging chemotherapies than tumor in CE regions. This has significant implications for planning boost volumes for radiation therapy. Of further interest in designing therapy protocols is the presence of simple microvascular hyperplasia in 65% of the samples from NE regions, which indicates that although there is increased vasculature in these areas, the vessel permeability is limited.

The relationship between increased intra-tumoural perfusion and malignant growth has been associated with hypoxic cellular conditions within GBM (44-50). The morphological feature of contrast enhancement on T1-weighted MR imaging, which

reflects the disruption of the blood–brain barrier, has previously been thought of as a marker of elevated complex microvasculature, but several studies have demonstrated a discrepancy between regions of contrast enhancement and microvascular density. In this study, a strong positive correlation was observed for rCBV and rPH in CE regions with the histopathologic features of proliferation, cell density, and microvascular hyperplasia. This suggests that DSC imaging is capable of capturing a clinically useful, noninvasive assessment of the CE lesion for newly diagnosed GBM that can be utilized on an individual basis to provide quantifiable biomarkers (7, 13, 19-22, 33, 51-53).

The pattern of microvascular proliferation can vary widely in GBM (54-61). Areas of infiltrative tumor often contain delicate vasculature that resembles normal cerebral vasculature. Regions with more malignant tumor features contain both simple and complex microvascular hyperplasia. Simple microvascular hyperplasia has been characterized by hyperplastic capillaries with increased endothelial cellularity and luminal patency (33, 54-61). Complex microvascular hyperplasia is identified by large collections of capillaries with partially to completely thrombosed slit-like lumen resulting in minimal perfusion to the surrounding tissue (33, 54-61). The correlation of rCBV and rPH with microvascular morphology suggests that DSC imaging is sensitive to all three types of vascular morphology and can used to guide the acquisition of tumor samples, irrespective of the patterns of contrast enhancement.

The results of our study challenge the widely held concept that T2 FSE and FLAIR hyperintense non-enhancing regions have limited malignant potential. By using physiologic MR imaging parameters to target tissue specimens from NE regions we were able to identify areas with histopathologic features corresponding to biologically active

tumor. Interestingly, rADC and rFSE were found to be associated with tumor score in the NE region but this was not the case in CE regions. This was thought to be due to partial volume averaging of tumor and necrosis within voxels that correspond to the CE region, which makes the image intensities higher than would have otherwise been observed. Previous investigations have also yielded mixed results. Sadeghi et al., in their investigation of untreated GBM, reported an inverse correlation of rADC with microvascular density but no inverse correlation between rADC and tumor cell density in their examination of 33 tumor tissue specimens (19). On the other hand, several other groups have reported finding an inverse correlation between rADC and cell density (30-33). These conflicting findings are likely due to the differences in sampling strategies for obtaining tissue samples, as well as the complex interactions of water diffusivity within the heterogeneous cellular environment of GBM.

Our study was specifically designed to look at regions within the enhancing and non-enhancing lesions with physiological imaging parameters that are suggestive of tumor. Given that it was not always possible to exactly target the areas requested, as well as the differences in scale of the image resolution versus the amount of tissue evaluated using histology, the fact that 90% of the enhancing samples and 81% of the non-enhancing samples had a positive tumor score is encouraging. To determine whether the imaging data can accurately define lesion boundaries would require a sampling strategy that also targeted regions of non-enhancing tumor with physiological parameters unlikely to correspond to tumor, however, this may not be practical from the patient perspective given the risk of taking tissue from regions of normal brain.

One limitation of this study is the potential for misregistration between biopsy sites and MR images uploaded to the neuro-navigational device theatrically exists when significant amounts of brain shift occur. Such a mismatch could lead to inaccuracy in DSC perfusion and diffusion weighted imaging measurements, however, several steps were utilized to negate any possible brain shift that may have occurred following dural opening. We sought to minimize significant amounts of brain shift by (a) performing accurate intraoperative neuronavigational system registration to the patient's facial anatomy, (b) avoiding substantial loss of cerebrospinal fluid, (c) watching for intraoperative brain swelling, (d) testing registration accuracy against visible cortical landmarks immediately prior to biopsy sampling, (e) using standardized regions of interest of sufficient size to compensate for any minimal shift in brain location. We believe that any minimal amount of brain shift that may have occurred prior to biopsy sampling did not result in significant sampling error or adversely affect the results of this study. Further prospective studies may consider implementing the use of closed brain biopsies to negate this potential limitation.

Our investigation suggests that the heterogeneous distribution of histopathologic features within GBM can be reliably identified by physiological MR imaging. The associations of imaging and histological parameters observed indicate that these physiological imaging variables are likely to be of interest for defining residual post-surgical tumor burden and may need to be considered in expanding the definition of the RANO criteria for assessing response to therapy (62).

7.5 Conclusions:

We have demonstrated that histopathologic features of GBM are differentially expressed between contrast enhancing and non-enhancing components of the tumor. In contrast enhancing regions DSC perfusion MR imaging variables can be used to identify tissue specimens with higher tumor proliferation, necrosis, and vascular hyperplasia. In the non-enhancing component of the lesion, diffusion weighted imaging variables are able to improve the detection of infiltrating tumor, which may lack some of the characteristic histopathologic features of GBM and may therefore respond differently to radiation or other types of therapy.

7.6 References:

1. Greenlee RT, Murray T, Bolden S. Cancer statistics 2000. CA Cancer J Clin. 2000;50:7-33.

2. Eby NL, Grufferman S. Increasing incidence of primary brain lymphoma in the US. Cancer. 1998;62:2461-2465.

3. Fulling KH, Garcia DM. Anaplastic astrocytoma of the adult cerebrum. Prognostic value of histologic features. Cancer. 1985;55:928-931.

4. Gilles FH, Brown WD, Leviton A. Limitations of the World Health Organization classification of childhood supratentorial astrocytic tumors. Cancer. 2000;88:1477–1483.

5. Prayson RA, Agamanolis DP, Cohen ML et al. Interobserver reproducibility among neuropathologists and surgical pathologists in fibrillary astrocytoma grading. J Neurol Sci. 2000;175(1):33-39.

6. Coons SW, Johnson PC, Scheithauer BW, Yates AJ, Pearl DK. Improving diagnostic accuracy and interobserver concordance in the classification and grading of primary gliomas. Cancer. 1997;79:1381–1393.

7. Law M, Oh S, Johnson G, et. al. Perfusion magnetic resonance imaging predict patient outcome as an adjunct to histopathology. Neurosurgery. 2006;58:1099-1107.

8. Coons SW, Johnson PC, Scheithauer BW, Yates AJ, Pearl DK. Improving diagnostic accuracy and interobserver concordance in the classification and grading of primary gliomas. Cancer. 1997;79:1381–1393.

9. Jackson A, Kassner A, Annesley-Williams D. Abnormalities in the Recirculation Phase of Contrast Agent Bolus Passage in Cerebral Gliomas: comparison with Relative Blood Volume and Tumor Grade. Am J Neuroradiol. 2002;23:7–14.

10. Cha S: Update on Brain Tumor Imaging: From Anatomy to Physiology. Am J Neuroradiol. 2006;27:475– 487.

11. Lev MH, Rosen BR. Clinical applications of intracranial perfusion mr imaging. Neuroimaging Clin N Am. 1999;9:309-331.

12. Henry RG, Vigneron DB, Fischbein NJ, et al. Comparison of relative cerebral blood volume and proton spectroscopy in patients with treated gliomas. Am J Neuroradiol. 2000;21:357-366.

13. Sugahara T, Korogi Y, Kochi M, et al. Correlation of MR imaging-determined cerebral blood volume maps with histologic and angiographic determination of vascularity of gliomas. Am J Roentgenol. 1998;171:1479-1486.

14. Lupo JM, Cha S, Chang SM, Nelson SJ. Dynamic susceptibility-weighted perfusion

imaging of high-grade gliomas: characterization of spatial heterogeneity. Am J Neuroradiol. 2005;26:1446-1454.

15. Cha S, Lu S, Johnson G, Knopp EA. Dynamic susceptibility contrast MR imaging: correlation of signal intensity changes with cerebral blood volume measurements. J Magn Reson Imaging. 2000;11:114–119.

16. Cha S, Lupo JM, Chen MH, et al. Differentiation of Glioblastoma Multiforme and Single Brain Metastasis by Peak Height and Percentage of Signal Intensity Recovery Derived from Dynamic Susceptibility-Weighted Contrast- Enhanced Perfusion MR Imaging. Am J Neuroradiol. 2007;28:1078-1084.

17. Barajas R, Chang J, Sneed P, Segal M, McDermott M, Cha S. Distinguishing Recurrent Brain Metastasis From Radiation Necrosis Following Gamma Knife Radiosurgery Using Dynamic Susceptibility Weighted Contrast-Enhanced Perfusion MR Imaging. Am J Neuroradiol. 2009;30:367-372.

18. Barajas R, Chang J, Segal M, et al. Distinguishing Recurrent Glioblastoma Multiforme from Radiation Necrosis Following External Beam Radiotherapy Using Dynamic Susceptibility Weighted Contrast-Enhanced Perfusion MR imaging. Radiology. 2009;253:486-496.

19. Sadeghi N, D'Haene N, Decaestecker C, et al. Apparent Diffusion Coefficient and Cerebral Blood Volume in Brain Gliomas: Relation to Tumor Cell Density and Tumor Microvessel Density Based on Stereotactic Biopsies. Am J Neuroradiol. 2008;29:476-482.

20. Aronen HJ, Gazit IE, Louis DN, et al. Cerebral blood volume maps of gliomas: comparison with tumor grade and histologic findings. Radiology. 1994;191:41–51.

21. Cha S, Johnson G, Wadghiri YZ, et al. Dynamic, contrast-enhanced perfusion MRI in mouse gliomas: correlation with histopathology. Magn Reson Med. 2003;49:848–855.

22. Maia AC Jr, Malheiros SM, da Rocha AJ, et al. MR cerebral blood volume maps correlated with vascular endothelial growth factor expression and tumor grade in nonenhancing gliomas. Am J Neuroradiol. 2005;26:777–783.

23. Rowley HA, Grant PE, Roberts TP. Diffusion MR imaging: theory and applications. Neuroimaging Clin N Am. 1999;9:343–361.

24. Le Bihan D, Turner R, Douek P, Patronas N. Diffusion MR imaging: clinical applications. Am J Roentgenol. 1992;159:591–599.

25. Kotsenas AL, Roth TC, Manness WK, Faerber EN. Abnormal diffusion-weighted MRI in medulloblastoma: does it reflect small cell histology? Pediatr Radiol. 1999;29:524–526.

26. Kitis O, Altay H, Calli C, Yunten N, Akalin T, Yurtseven T. Minimum apparent diffusion coefficients in the evaluation of brain tumors. European Journal of Radiology. 2005;55:393–400.

27. Le Bihan D, Breton E, Lallemand D, Grenier P, Cabanis E, Laval-Jeantet M. MR imaging of intravoxel incoherent motions: application to diffusion and perfusion in neurologic disorders. Radiology. 1986;161:401–407.

28. Guo AC, Cummings TJ, Dash RC, Provenzale JM. Lymphomas and high-grade astrocytomas: comparison of water diffusibility and histologic characteristics. Radiology. 2002;224:177–1783.

29. Barajas RF Jr, Rubenstein JL, Chang JS, Hwang J, Cha S. Diffusion-weighted MR imaging derived apparent diffusion coefficient is predictive of clinical outcome in primary central nervous system lymphoma. AJNR. 2010;31:60-66.

30. Stadnik TW, Chaskis C, Michotte A, et al. Diffusion-weighted MR imaging of intracerebral masses: comparison with conventional MR imaging and histologic findings. Am J Neuroradiol.   2001;22:969–976.

31. Sugahara T, Korogi Y, Kochi M, et al. Usefulness of diffusion-weighted MRI with echo-planar technique in the evaluation of cellularity in gliomas. J Magn Reson Imaging. 1999;9:53–60.

32. Gupta RK, Cloughesy TF, Sinha U, et al. Relationships between choline magnetic resonance spectroscopy, apparent diffusion coefficient and quantitative histopathology in human glioma. J Neurooncol. 2000;50:215–226.

33. Barajas RF Jr, Hodgson JG, Chang JS, et al. Glioblastoma multiforme regional genetic and cellular expression patterns: influence on anatomic and physiologic MR imaging. Radiology. 2010;254(2):564-576.

34. Cha S, Johnson G, Yuz M, et al. The role of contrast-enhanced perfusion MR imaging in differentiating between recurrent tumor and radiation necrosis. Proceedings: Radiological Society of North America. 1999;213:188.

35. Cha S, Knopp EA, Johnson G, et al. Dynamic contrast-enhanced T2*-weighted MR imaging of recurrent malignant gliomas treated with thalidomide and carboplatin. Am J Neuroradiol. 2000;21:881-890.

36. Cha S, Pierce S, Knopp EA, et al. Dynamic contrast-enhanced T2*-weighted MR imaging of tumefactive demyelinating lesions. Am J Neuroradiol. 2001;22:1109-1116.

37. Sorensen AG, Buonanno FS, Gonzalez RG, et al. Hyperacute stroke: Evaluation with combined multisection diffusion- weighted and hemodynamically weighted echo-planar MR imaging. Radiology. 1996;199:391-401.

38. McKnight TR, Smith KJ, Chu PW, et al. Choline metabolism, proliferation, and angiogenesis in nonenhancing grades 2 and 3 astrocytoma. J Magn Reson Imaging. 2011 Apr;33(4):808-816.

39. Khayal IS, Vandenberg SR, Smith KJ, et al. MRI apparent diffusion coefficient reflects histopathologic subtype, axonal disruption, and tumor fraction in diffuse-type grade II gliomas. Neuro Oncol. 2011 Nov;13(11):1192-1201.

40. Lee MC, Cha S, Chang SM, Nelson SJ. Dynamic susceptibility contrast perfusion imaging of radiation effects in normal-appearing brain tissue: changes in the first-pass and recirculation phases. J Magn Reson Imaging. 2005 Jun;21(6):683-693.

41. Hartkens T, D. R, Schnabel JA, Hawkes DJ, Hill DLG. VTK CISG Registration Toolkit: An open source software package for affine and non-rigid registration of single- and multimodal 3D images [abstract] BVM; 2002; Leipzig, Germany: Springer-Verlag, 2002:185.

42. Crawford FW, Khayal IS, McGue C, et al. Relationship of pre-surgery metabolic and physiological MR imaging parameters to survival for patients with untreated GBM. J Neurooncol. 2009 Feb;91(3):337-351.

43. Saraswathy S, Crawford FW, Lamborn KR, et al. Evaluation of MR markers that predict survival in patients with newly diagnosed GBM prior to adjuvant therapy. J Neurooncol. 2009 Jan;91(1):69-81.

44. Kleihues P, Soylemezoglu F, Schäuble B, Scheithauer BW, Burger PC. Histopathology, classification, and grading of gliomas. Glia. 1995;15(3):211-221.

45. Preusser M, Haberler C, Hainfellner JA. Malignant glioma: neuropathology and neurobiology. Wien Med Wochenschr. 2006;156(11-12):332-337.

46. Tate M, Aghi M. Biology of angiogenesis and invasion in glioma. Neurotherapeutics. 2009; 6:447-457.

47. Wong M, Prawira A, Kaye A, Hovens C. Tumour angiogenesis: Its mechanism and therapeutic implications in malignant gliomas. Journal of Clinical Neurosceience. 2009;16: 1119-1130.

48. Louis DN, Ohgaki H, Wiestler OD, Cavenee WK. World Health Organization classification of tumors: pathology and genetics of tumors of the nervous system, fourth edition. IARC Press, Lyon, 2007.

49. Knopp EA, Cha S, Johnson G, et al. Glial neoplasms: dynamic contrast-enhanced T2-weighted MR imaging. Radiology. 1999;211:791–798.

50. Brem S, Cotran R, Folkman J. Tumor angiogenesis: a quantitative method for histologic grading. J Natl Cancer Inst. 1972;48:347–356.

51. Batra A, Tripathi RP, Singh AK. Perfusion magnetic resonance imaging and magnetic resonance spectroscopy of cerebral gliomas showing imperceptible contrast enhancement on conventional magnetic resonance imaging. Australasian Radiology. 2004;48:324–332.

52. Ginsberg LE, Fuller GN, Hashmi M, et al. The Significance of Lack of MR Contrast Enhancement of Supratentorial Brain Tumors in Adults: Histopathological Evaluation of a Series. Surg Neurol. 1998;49:436–440.

53.   Law M, Yang S, Wang H, et al. Glioma grading: sensitivity, specificity, and predictive values of perfusion MR imaging and proton MR spectroscopic imaging compared with conventional MR imaging. Am J Neuroradiol. 2003;24(10):1989– 1998.

54. Miyagami M, Katayama Y. Angiogenesis of glioma: evaluation of ultrastructural characteristics of microvessels and tubular bodies (Weibel–Palade) in endothelial cells and immunohistochemical findings with VEGF and p53 protein. Med Mol Morphol. 2005;38:36–42.

55. Deane BR, Lantos PL. The vasculature of experimental brain tumours. Part 1. A sequential light and electron microscope study of angiogenesis. J Neurol Sci. 1981;49:55-66.

56. Deane BR, Lantos PL. The vasculature of experimental brain tumours. Part 2. A quantitative assessment of morphological abnormalities. J Neurol Sci. 1981;49:67-77.

57. Rojiani AM, Dorovini-Zis K. Glomeruloid vascular structures in glioblastoma multiforme: an immunohistochemical and ultrastructural study. J Neurosurg. 1996;85(6):1078-1084.

58. Izycka-Swieszewska E. Immunomorphological analysis of the vascular stroma in glioblastoma. Neurol Neurochir Pol. 2003;37(1):59-71.

59. Wesseling P, Vandersteenhoven JJ, Downey BT, Ruiter DJ, Burger PC. Cellular components of microvascular proliferation in human glial and metastatic brain neoplasms. A light microscopic and immunohistochemical study of formalin-fixed, routinely processed material. Acta Neuropathol. 1993;85(5):508-514.

60. Jain, R., Gutierrez, J., Narang, J., Scarpace L., Schultz, L., Lemke, N., Patel, S.C., Mikkelsen, T., Rock, J. In vivo correlation of tumor blood volume and permeability with histological and molecular angiogenic markers in gliomas. Am J Neuroradiology 2011; 32: 388 - 394.

61. Jain, R., Narang, J., Gutierrez, J., Schultz, L., Scarpace L., Rosenblum, M., Mikkelsen, T., Rock, J. Correlation of Immuno-histological and Perfusion Vascular Parameters with Contrast Enhancement using Image-guided Biopsy Specimens in Gliomas. Academic Radiology 2011 Aug;18(8):955-962.

62. Wen PY, Macdonald DR, Reardon DA, et al. Updated response assessment criteria for high-grade gliomas: response assessment in neuro-oncology working group. J Clin Oncol. 2010 Apr 10;28(11):1963-1972.

7.7 Supplemental Tables:

Table 7.6 (Supplemental): Significant correlations between histopathologic features of GBM and MR imaging parameters within CE regions.

Significant Correlations Between Histopathologic Features of GBM and MR Imaging Parameters Within CE Regions							
Histopathologic Features	MR Imaging Parameter	Pt #	TS #	OR	95% CI		P value
Tumor Score	rFLAIR	47	90		Kt:-0.28		0.010
Tumor Score	rCBV	29	52	2.36	1.33	4.18	0.003
Tumor Score	rPH	30	53	2.16	1.19	3.92	0.011
Tumor Score	RF	29	52	0.84	0.73	0.97	0.015
Necrosis	rCBV	29	52	1.32	1.10	1.60	0.003
Total MVH	rT1C	47	89	2.30	1.10	4.82	0.027
Total MVH	rCBV	29	52	1.86	1.21	2.85	0.005
Total MVH	rPH	30	53	2.40	1.31	4.41	0.005
Delicate MVH	rT1C	47	89	0.42	0.19	0.93	0.033
Simple MVH	rPH	30	53	1.44	1.01	2.05	0.044

(Categorical — row group label spanning the left side of all data rows)

Continuous	**Proliferation**	**rT1C**	47	89	6.55	NA	NA	0.04
	Proliferation	**rCBV**	29	51	4.42	NA	NA	<0.001
	TCN	**rCBV**	29	52	43.06	NA	NA	0.01
	TCN	**rPH**	30	53	57.56	NA	NA	0.01

Note: Odds ratio (ordinal outcomes) or coefficient (continuous outcomes) for statistically significant parameters at P< 0.05 within contrast enhancing regions; the estimate for the corresponding tumor tissue region is also listed for comparison though it may not always be significant. In the cases where the association is non-linear, the median Kendall Tau (Kt) correlation coefficient and p-value is reported. Total MVH denotes all microvascular hyperplasia including both simple and complex. TCN= tumor cell number per high power field. Pt # denotes number of patients. TS # denotes number of tissue samples. rFLAIR denotes relative fluid attenuated inversion recovery. rPH denotes relative peak height. RF denotes recovery factor. rT1C denotes relative quantitative contrast enhancement. rFSE denotes relative quantitative T2 hyperintensity. rCBV denotes relative cerebral blood volume. rADC denotes relative apparent diffusion coefficient. NA denotes not applicable.

Table 7.7 (Supplemental): Significant correlations between histopathologic features of GBM and MR imaging parameters within NE regions.

Significant Correlations Between Histopathologic Features of GBM and MR Imaging Parameters Within NE Regions								
Histopathologic Feature		MR Imaging Parameter	Pt #	TS #	OR	95% CI		P value
Categorical	**Tumor Score**	**rFSE**	20	26	0.54	0.3	0.94	0.030
	Tumor Score	**rADC**	19	24	0.15	0.03	0.74	0.020
	Tumor Score	**rPH**	12	17	5.77	1.74	19.15	0.004
	AD	**rADC**	19	24	NA	Kt: -0.52		0.005
	AD	**rFA**	19	24	3.79	1.1	13.12	0.035
	AD	**rPH**	12	17	3.32	1.07	10.35	0.038
	Delicate MVH	**rT1C**	20	26	NA	Kt:0.42		0.027
	Delicate MVH	**rFA**	19	24	NA	Kt:0.51		0.009
Continuous	**Proliferation**	**rFLAIR**	19	24	NA	Kt:0.51		0.010
	Proliferation	**rADC**	19	24	NA	Kt:-0.49		0.010
	TCN	**rPH**	12	17	50.77	NA	NA	0.05

Note: Odds ratio (ordinal outcomes) or coefficient (continuous outcomes) for statistically significant parameters at p less than 0.05 within non-enhancing regions; the estimate for the corresponding tumor tissue region is also listed for comparison though it may not always be significant. In the cases where the association is non-linear, the median Kendall Tau (Kt) correlation coefficient and p-value is reported. TCN= tumor cell number per high power field. AD denotes architectural disruption. rFLAIR denotes relative fluid attenuated inversion

recovery. rPH denotes relative peak height. RF denotes recovery factor. rT1C denotes relative quantitative contrast enhancement. rFSE denotes relative quantitative T2 hyperintensity. rADC denotes relative apparent diffusion coefficient. rFA denotes relative fractional anisotropy. NA denotes not applicable.

Table 7.8 (Supplemental): Significant correlations between histopathologic features of GBM stratified by tumor specimen region.

Significant Correlations Between Histopathologic Features of GBM Stratified by Tumor Specimen Region							
CE Tissue Specimen							
Histopathological Features		**Pt #**	**TS #**	**OR**	**95 % CI**		**P Value**
Tumor score	Cell Per HPF	47	90	1.02	1.01	1.02	<.001
Tumor score	Proliferation	47	89	1.10	1.04	1.16	0.001
Tumor score	Hypoxia	47	89	2.75	1.75	4.33	<.001
Tumor score	Total MVH	47	89	3.73	1.99	7.02	<.001
Tumor score	Delicate MVH	47	89	0.39	0.26	0.57	<.001
Tumor score	Simple MVH	46	88	3.00	2.09	4.32	<.001
Tumor score	Complex MVH	47	89	1.78	1.14	2.77	0.011
AD	Tumor score	46	88	5.18	3.16	8.49	<.001
AD	TCN	46	88	1.01	1.00	1.01	0.02

AD	**Necrosis**	46	88	4.31	1.81	10.28	0.001
AD	**Hypoxia**	46	88	2.80	1.87	4.21	<.0001
AD	**Total MVH**	46	88	2.19	1.23	3.89	0.007
AD	**Delicate MVH**	46	88	0.47	0.30	0.74	0.001
AD	**Simple MVH**	46	88	1.98	1.28	3.08	0.002
Necrosis	**Tumor score**	47	90	2.62	1.27	5.42	0.009
Necrosis	**Hypoxia**	47	89	3.27	2.05	5.22	<0.001
Necrosis	**Delicate vessels**	47	89	0.37	0.23	0.59	<0.001
Total MVH	**Tumor score**	47	89	1.14	1.85	4.64	<0.001
Total MVH	**Proliferation**	47	88	1.10	1.04	1.17	0.001
Total MVH	**Hypoxia**	47	89	1.79	1.20	2.67	0.005
Total MVH	**Delicate MVH**	47	89	0.45	0.28	0.72	0.001
Total MVH	**Simple MVH**	47	89	4.72	2.92	7.64	<0.001
Total MVH	**Complex MVH**	47	89	7.13	1.36	37.32	0.02
Delicate MVH	**Tumor score**	47	89	0.37	0.26	0.54	<0.001
Delicate MVH	**TCN**	47	89	1.00	0.99	1.00	0.004
Delicate MVH	**Proliferation**	47	88	0.96	0.94	0.99	0.008
Delicate MVH	**Necrosis**	47	89	0.30	0.14	0.64	0.002

Delicate MVH	**Hypoxia**	47	89	0.39	0.24	0.63	<0.001
Delicate MVH	**Total MVH**	47	89	0.33	0.18	0.63	0.002
Delicate MVH	**Simple MVH**	47	89	0.49	0.34	0.72	<0.001
Delicate MVH	**Complex MVH**	47	89	0.30	0.19	0.47	<0.001
Simple MVH	**Tumor score**	47	89	3.42	2.24	5.21	<0.001
Simple MVH	**TCN**	47	89	1.00	1.00	1.01	0.011
Simple MVH	**Proliferation**	47	88	1.05	1.02	1.08	0.002
Simple MVH	**Hypoxia**	47	89	1.89	1.33	2.70	<0.001
Simple MVH	**Total MVH**	47	89	8.45	4.38	16.30	<0.001
Simple MVH	**Delicate MVH**	47	89	0.51	0.35	0.75	0.001

Continuous Variables

Proliferation	**Tumor score**	47	89	7.03	NA	<.001
Proliferation	**TCN**	47	89	0.04	NA	<.001
Proliferation	**AD**	46	87	2.26	NA	<.001
Proliferation	**Hypoxia**	47	88	5.25	NA	<.001
Proliferation	**Total MVH**	47	88	9.75	NA	<.001
Proliferation	**Simple MVH**	47	88	5.73	NA	<.001
Proliferation	**Complex MVH**	47	88	6.91	NA	<.001
TCN	**Tumor score**	47	90	112.33	NA	<.001

				OR	95 % CI		P Value
TCN	TCN	46	88	38.07	NA		<.001
TCN	Hypoxia	47	89	Kt= 0.242	NA		0.032
TCN	Total MVH	47	89	Kt= 0.284	NA		0.014
TCN	Simple MVH	47	89	Kt= 0.3	NA		0.008
TCN	Complex MVH	47	89	Kt= 0.263	NA		0.023

NE Region

Histopathological Features		Pt #	TS #	OR	95 % CI		P Value
Tumor score	TCN	20	26	1.02	1.01	1.03	0.0003
Tumor score	Proliferation	20	26	1.24	1.10	1.39	0.0004
Tumor score	Total MVH	20	26	4.81	1.42	16.33	0.0117
Tumor score	Simple MVH	20	26	2.26	1.02	5.00	0.0436
AD	Tumor score	20	26	10.92	3.41	35.03	<.0001
AD	TCN	20	26	1.01	1.00	1.02	0.0419
AD	Proliferation	20	26	1.21	1.09	1.34	0.0003
AD	Total MVH	20	26	9.34	2.77	31.48	0.0003
AD	Simple MVH	20	26	2.04	1.04	4.02	0.0394
Total MVH	Tumor score	20	26	3.21	1.32	7.81	0.01
Total MVH	Proliferation	20	26	1.13	1.03	1.24	0.013

Total MVH	Simple MVH	20	26	7.61	2.27	25.50	0.001
Simple MVH	Tumor score	20	26	2.66	1.14	6.21	0.0243
Simple MVH	Proliferation	20	26	1.16	1.04	1.28	0.007
Simple MVH	Total MVH	20	26	19.49	4.78	79.46	<.0001

Continuous Variables

Proliferation	Tumor score	20	26	4.60	NA	<.001
Proliferation	AD	20	26	4.31	NA	<.001
Proliferation	Simple MVH	20	26	3.52	NA	0.02
TCN	Tumor score	20	26	51.32	NA	0.02
TCN	AD	20	26	39.23	NA	0.04

Note: Statistically significant (P< 0.05) associations observed between histopathologic features of GBM. AD denotes architectural disruption. Total MVH= all microvascular hyperplasia including both simple and complex. Tumor cell density denotes mean tumor cell number per 200x-microscopic field. TCN= tumor cell number per high power field. NE denotes non-enhancing. In the cases where the association is non-linear, the median Kendall Tau (Kt) correlation coefficient and p-value is reported. NA denotes not applicable.

Table 7.9 (Supplemental): Significant correlations between anatomic and phsyiologic
MR imaging parameters stratified by contrast enhancing and non-enhancing regions.

Significant Correlations Between Anatomic and Physiologic MR Imaging Parameters Stratified by Contrast Enhancing and Non-Enhancing Regions					
CE Region					
MR Imaging Parameters		Pt #	TS #	B Value	P Value
rFSE	rFLAIR	48	93	0.54	0.05
rFSE	rCBV	29	52	-0.151	<0.001
rFSE	rPH	30	53	-0.245	<0.001
rCBV	rT1C	29	52	0.735	<0.001
rCBV	rPH	29	52	1.221	<0.001
rCBV	rADC	28	51	-1.32	<0.001
rADC	rFSE	47	90	0.33	<0.001
rADC	rFA	47	90	-0.33	0.01
rADC	RF	28	51	-0.078	<0.001

MR Imaging Parameters		Pt #	TS #	B Value	P Value
rFA	rFSE	47	90	-0.132	0.002

NE Region					
MR Imaging Parameters		Pt #	TS #	B Value	P Value
rT1C	rFLAIR	20	26	-0.23	0.01
rT1C	rFSE	20	26	-0.18	<0.001
rFSE	rFLAIR	20	26	1.29	0.01
rCBV	rPH	11	15	0.86	0.01
rCBV	rADC	10	14	-1.13	0.02
rADC	rFLAIR	19	24	0.65	0.01
rADC	rT1C	19	24	-1.18	0.03
rADC	rFSE	19	24	0.53	<0.001
rADC	rFA	19	24	-0.44	0.03
rFA	PSR	11	16	0.04	0.05

Note: Statistically significant (P< 0.05) associations observed between anatomic and physiologic MR imaging parameters. Pt # denotes number of patients. TS# denotes number of tissue specimens. rT1C denotes relative quantitative contrast enhancement. rFSE denotes relative quantitative T2 hyperintensity. rCBV denotes relative cerebral blood volume. rPH denotes relative peak height. PSR denotes percentage of signal intensity recovery. RF denotes recovery factor. rADC denotes relative apparent diffusion coefficient.

rFLAIR denotes relative fluid attenuated inversion recovery. rFA denotes relative fractional anisotropy. CE denotes contrast enhancing. NE denotes non-enhancing.

CHAPTER 8 : Summary

Advances in treatment management are critical for improving upon the poor prognosis of patients with glioblastoma (GBM). In recent years, the treatment paradigm for these patients has shifted to include antiangiogenic therapy and subsequently has generated new needs for noninvasive MRI in the field of neuro-oncology. The goal of this dissertation project was to develop and apply physiologic imaging techniques to guide the assessment of response to antiangiogenic therapy for patients with GBM. This dissertation puts forth three major themes toward the advancement of this goal.

First, this work supports that integrating dynamic susceptibility contrast (DSC) MRI into the exam workflow for patients with glioma is feasible in the clinical setting. DSC imaging can be acquired with a single dose of gadolinium when acquired with a low flip angle, rather than adding a preload dose prior to high flip angle acquisitions. This means that estimates of cerebral blood volume and permeability can be achieved without increasing the total gadolinium dose and associated risks to the patient. Further, these parameters can be generated using non-parametric, model-free analysis with limited computational expense. The integration of non-parametric post-processing into SIVIC (http://sourceforge.net/projects/sivic/), a freely available open-source software platform for visualizing 4-dimensional MRI data, is a major advance in making DSC post-processing more easily accessible in the clinic. This software package is a collaborative project led by Dr. Jason Crane and Beck Olson of the Surbeck Lab for Advanced Imaging

and is an exciting example of how these advances in MRI analysis can be brought to the clinic.

Second, physiologic imaging can aid in the preoperative characterization of heterogeneous GBM. DSC imaging was found to yield estimates of blood volume that were predictive of vascular morphology in tissue samples from treatment-naïve GBM. Complementary physiologic imaging methods, DSC and diffusion weighted imaging (DWI), provided insights into the tumor histology within both the non-enhancing and contrast-enhancing lesion. These imaging methods offer noninvasive correlates of biological features, which can aid in guiding tissue sampling for diagnosis. In the future, this could be used to describe initial physiologic tumor burden in order to tailor subsequent treatment plans to individual patients.

Finally, DSC and DWI can be used to describe the physiologic changes underlying tumor response to therapy. This is critical to patient management in the antiangiogenic setting, since the therapy-induced reduction in permeability of tumor vasculature obscures the historical assessment metrics based on anatomic MRI changes. Assessing early serial changes in blood volume and permeability following antiangiogenic therapy was found to predict patient outcome. Diffusion changes during this time frame were found to be treatment-specific and reflected the anti-edema effect of bevacizumab. Together, these projects form a foundation for future validation in

prospective large-scale clinical trials in order to develop of predictive biomarkers of response to antiangiogenic therapy.

       The opportunities created by antiangiogenic therapy to improve patient outcome have been accompanied by new research challenges in how to best evaluate the indication and benefit of these treatments. The inclusion of perfusion and diffusion MRI to clinical exams provides physiologic clues for individualizing treatments and identifying response, which will ultimately improve the clinical management of patients with GBM.

Publishing Agreement

It is the policy of the University to encourage the distribution of all theses, dissertations, and manuscripts. Copies of all UCSF theses, dissertations, and manuscripts will be routed to the library via the Graduate Division. The library will make all theses, dissertations, and manuscripts accessible to the public and will preserve these to the best of their abilities, in perpetuity.

Please sign the following statement:

I hereby grant permission to the Graduate Division of the University of California, San Francisco to release copies of my thesis, dissertation, or manuscript to the Campus Library to provide access and preservation, in whole or in part, in perpetuity.

Author Signature

6/8/2012
Date